1-1-2021

ACOUSTIC BESSEL AND VORTEX BEAMS: FORCES AND REFRACTION

Xudong Fan
University of Mississippi

ACOUSTIC BESSEL AND VORTEX BEAMS: FORCES AND REFRACTION

A Dissertation
presented for the degree of Doctor of Philosophy
in the Department of Physics and Astronomy
The University of Mississippi

by

XUDONG FAN

December 2021

ABSTRACT

Non-contact manipulation techniques or tweezers devices are invaluable for applications in physics, chemistry, biology, and engineering. Acoustic tweezers using either standing waves or focused beams have been investigated for more than a few decades with advantages of label-free operation, noninvasiveness, and biocompatibility when compared with the optical, magnetic, and electrical counterparts. Here, a new type of acoustic tweezers (i.e. acoustic tractors) is studied using acoustic Bessel and vortex beams that are able to pull objects against the beam's propagation over centimeter ranges. Stable acoustic tractors require transversely stable trapping in addition to axially negative pulling. Hence, the transverse forces acting on a spherical particle centered on the axis of axisymmetric and vortex Bessel beams were first investigated by using both the Gorkov potential and the partial wave expansion with the trapping behaviors more flexible than trapping by standing waves and focused beams used in conventional acoustic tweezers. Then, the physical parameters desired for simultaneous trapping and pulling of particles of different sizes were examined. The results reveal the possibility of achieving a simultaneous pulling and trapping of a small particle using Bessel beams. In addition, the Born approximation method was used to analyze the transverse trapping force for spherical particles and particles of different shapes and orientations. Compared with the full solution from the partial wave expansion, the Born approximation can simplify the computation and can also provide insight into the transverse radiation force. In addition, a mathematical framework based on phase shifts adapted from quantum scattering theory was used to analyze the axial radiation force. This phase shift approach can allow one to engineer object and beam parameters to design experimentally achievable axially pulling forces. Furthermore, the effects of realistic factors such as gravity, buoyancy, and the acoustic streaming were also evaluated. The work here is useful for the further study of acoustic radiation force and will lead to an experimental demonstration of stable acoustic tractor beams.

Furthermore, the refraction of acoustic Bessel and vortex beams in an inhomogeneous medium was studied because in the practical situations and applications, media are commonly inhomogeneous with spatially varying parameters, for example, in ocean environments or biomedical materials. Hence, it is of fundamental and practical interests to study the effects caused by the medium inhomogeneity on the propagation of acoustic beams. Here, an acoustic vortex Bessel beam with topological charge of $l = -1$ propagating in a linearly stratified medium was simulated. A series of unstable and dynamic behaviors of acoustic vortices as the beam propagates in the inhomogeneous media were observed. These behaviors include bending, stretching, distorting and untwisting of the vortex beam, migration of singular points, and reversal of energy flux and angular momentum. Then the acoustic orbital Hall effect caused by the interactions between acoustic vortex beams and medium inhomogeneity were studied. The transverse shifts caused by the acoustic Hall effect were numerically observed, analyzed, and compared with theoretical predictions. A special example of the acoustic Hall effect occurring on the sharp boundary between two media, i.e., acoustic Imbert-Fedorov effect, was also investigated. Possible experimental observations of the acoustic Hall effect were suggested in a water tank using salinity gradient, through an interface between two media, and in air with the aid of a gradient metasurface. This work provides a basis for the fundamental study of acoustic vortices in inhomogeneous media or complex media.

DEDICATION

This work is dedicated to my parents, family and friends, their support and encouragement are invaluable.

LIST OF ABBREVIATIONS AND SYMBOLS

Al	aluminum
OAM	orbital angular momentum
EOAM	extrinsic orbital angular momentum
IOAM	intrinsic orbital angular momentum
IF or I-F	Imbert-Fedorov
PMMA	Poly(methyl methacrylate)
$\mathbf{F}$	radiation force
J_l	l-order Bessel function
$\overleftrightarrow{T}$	momentum-flux tensor
$\mathbf{Y}$	dimensionless radiation force
a	radius of spherical objects
b	inner radius of spherical shells
c_n	scattering coefficient
c_L	longitudinal sound propagation speed
c_T	transverse sound propagation speed
f	sound frequency or force density
f_1	monopole factor
f_2	dipole factor
$\mathbf{g}$	momentum density
l or m	topological charge or beam order
n	refractive index
p	acoustic pressure

s_n	scattering function
t	phase shift ratio δ_0/δ_1
v	velocity field
K	bulk modulus
Y_{nm}	spherical harmonics
j_n	spherical Bessel function
h_n	spherical Hankel function
k	acoustic wave number magnitude
I	sound intensity
P_n	Legendre polynomials
R	transverse location of objects
$\mathbf{S}$	energy flux
U	Gorkov potential
Φ_l	acoustic contrast factors for the order l
κ	axial wave number magnitude or bulk modulus ratio
μ	transverse wave number magnitude or dynamic viscosity of fluid
α	medium inhomogeneity
α_n	real part of scattering coefficient c_n
β_n	imaginary part of scattering coefficient c_n
β	paraxiality parameter
θ	scattered angle or incident angle
λ	wavelength or mass density ratio
ρ	density
ω	angular frequency

δ	thickness of boundary layer
δ_r	transverse shift of orbital Hall effect
ν	kinematic viscosity of fluid
η	dynamic viscosity of fluid
η_n	complex phase shift
δ_n	real part of the complex phase shift η_n
γ_n	imaginary part of the complex phase shift η_n

ACKNOWLEDGEMENTS

I would like to first give my sincere gratitude to my advisor Dr. Likun Zhang of the National Center for Physical Acoustics at University of Mississippi. I would like to thank him for his invaluable trust, high expectations, extraordinary patience and consistent encouragement. He always gave me great help by providing me with necessary materials, advice of great value and inspiration of new ideas whenever I ran into a trouble spot or had a question about my research or writing. Without his strong support, this dissertation could not been the present form.

I am also deeply grateful to Dr. Richard Raspet, Dr. Rogar Waxler, Dr. Baharak Sajjadi and Dr. Wei-Yin Chen for serving on the dissertation committee, providing invaluable assistance and their helpful comments through my Ph.D study. I would like also to thank Dr. Kevin Beach for his generous help throughout my Ph.D years. I am thankful to all members of the National Center for Physical Acoustics (NCPA) and the Department of Physics and Astronomy.

Finally, I would like to express my heartfelt gratitude to my parents and to my friends Dr. Feiyan Cai, Dr. Zheguang Zou, Dr. Robert Lirette, Chen Cheng, Mukunda Acharya, Xinyue Gong, Guoqing Liu,and Madiligama Ralalage Madusanka Abeykoon for providing me with unfailing support, considerable comments, and continuous encouragement throughout my years of study and through the process of researching and writing this dissertation. This accomplishment would not have been possible without them.

The support of the start-up fund from the University of Mississippi is acknowledged.

TABLE OF CONTENTS

LIST OF FIGURES

CHAPTER 1

BACKGROUND

This dissertation studies the acoustic radiation force generated by acoustic Bessel and vortex beams, and also studies the propagation of these beams in inhomogeneous media. Before discussing the details, this chapter briefly introduces the related background.

1.1 Major milestones about acoustic radiation forces

The first portion of the dissertation focuses on the acoustic radiation force. Radiation force and radiation pressure are fundamental phenomena in both electromagnetic waves and acoustic waves. The radiation forces are caused by momentum transfer from the waves to matter due to the scattering or reflection from the objects or from spatial variations and the absorption from objects.[1] Compared with the optical and other counterparts, acoustic manipulation methods have the advantages of label-free operation, noninvasiveness, and biocompatibility. In this regard, acoustic-based particle manipulation methods can present an excellent alternative for a wide range of applications in many fields such as physics, chemistry, biology, and engineering.

Major milestones in the history of radiation forces are shown in Fig. 1.1. The first experiment related to acoustic radiation force was the acoustic streaming observation by Faraday in 1831[7] after the finding of pressure of light by Kepler in 1619.[8] In 1874, August Kundt demonstrated the acoustic radiation force on particles inside a cylindrical tube for acoustic standing waves,[9] where lycopodium powder was trapped at the pressure nodes of the acoustic field (Fig. 1.2). In 1902,

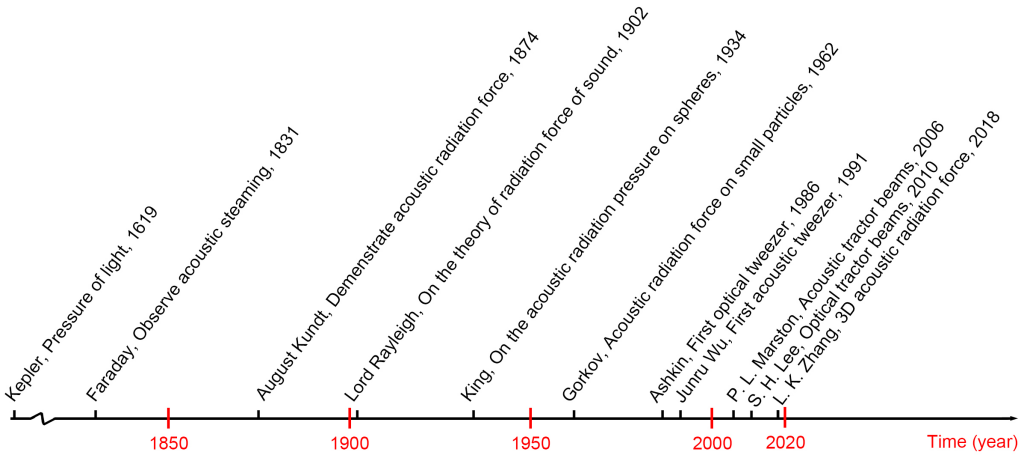

Figure 1.1: Major milestones in the history of radiation force.

the concept and theory of acoustic radiation force and pressure were scientifically defined by Lord Rayleigh (Fig. 1.3).[10] The acoustic radiation force effect on an interface between two media was investigated by Hertz and Mende[11] in 1939 where they found the direction of radiation force can be both outward and toward the sound source depending on the medium properties (Fig. 1.4). Then acoustic radiation forces were further explored by Gorkov in 1962[12] (Fig. 1.5) for one dimensional standing waves, where the acoustic trapping of a small particle in the Rayleigh regime (object size is much smaller than the wavelength) was considered using the concept of force potential. Based on the Gorkov potential, relatively light and soft particles (like droplets) are trapped to the pressure maximum (node) in the Rayleigh regime, yet relatively dense and stiff particles (like elastic objects) would be trapped to pressure minimum (anti-node). Later in 1991, Junru Wu first showed that latex particles and frog eggs could be manipulated by acoustic tweezers using two collimated focused ultrasonic transducers (Fig. 1.6).[2] In regards to the pulling force, Marston first predicted an acoustic negative pulling force using a non-diffracting Bessel beam in 2006.[13] The negative force was interpreted later in terms of the conservation of momentum and the asymmetry of scattering by Zhang and Marston in 2011 and 2012.[14,15] Later in 2012, Xu et al.[16] found that a particle in a liquid can be pulled backward with two crossed acoustic plane waves. In 2013, Courtney et al.[3] used a circular ultrasound array of 16 elements to generate standing Bessel waves to trap and manipulate particles (Fig 1.7), and in 2014, Démoré et al.[17] utilized a speaker array to generate sound fields in

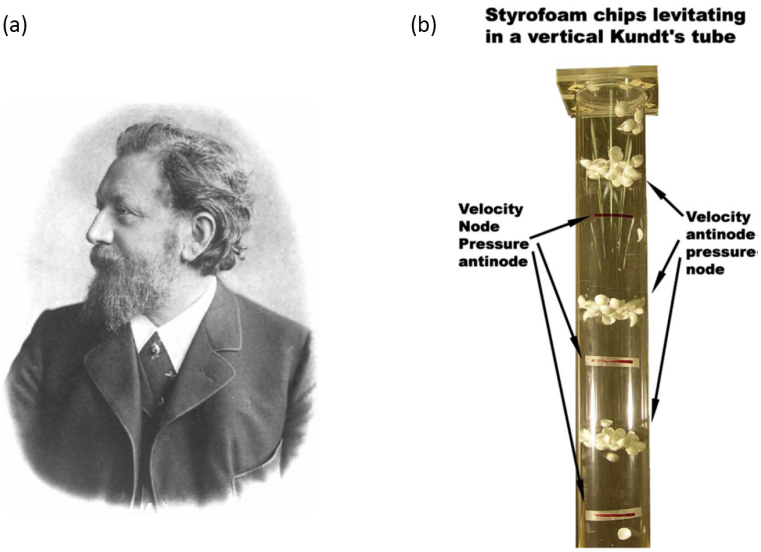

Figure 1.2: (a) August Kundt, German physicist, 1839-1894. (b) Styrofoam chips are trapped to the pressure nodes of acoustic standing waves in a cylindrical tube. Figure from Sarvazyan et al.[1]

a specific direction to pull a large triangle particle in an experiment. Later in 2015 and 2016, Marzo et al.[4] and Melde et al.[5] realized flexible particle manipulations using speaker arrays (Fig 1.8) and acoustic histograms (Fig 1.9). In 2018, Zhang derived the expressions of acoustic radiation force on an arbitrary-size and arbitrarily-located sphere, which provides the theoretical foundation for both trapping and pulling,[18] and later in 2019, Fan and Zhang systematically analyzed the trapping behavior of an object located at the beam axis and suggested the possibility of achieving acoustic tractor beams.[19]

1.2 Theory of acoustic radiation forces

When an object of volume V is placed in an acoustic field, there exists an acoustic radiation force acting on it. This force originates from the momentum transfer from the field to the object due to the scattering, reflection and absorption. The acoustic radiation force acts throughout the volume, but owing to the overall momentum conservation, the problem can be reduced to forces acting on the surface S of the object. Following the classical treatment, the time-averaged acoustic radiation force $\mathbf{F}$ can be expressed in terms of momentum-flux tensor $\overleftrightarrow{T}$ over the surface of the

Figure 1.3: John William Strutt, also known as Lord Rayleigh, British scientist, 1842-1919. Figure from Sarvazyan et al.[1]

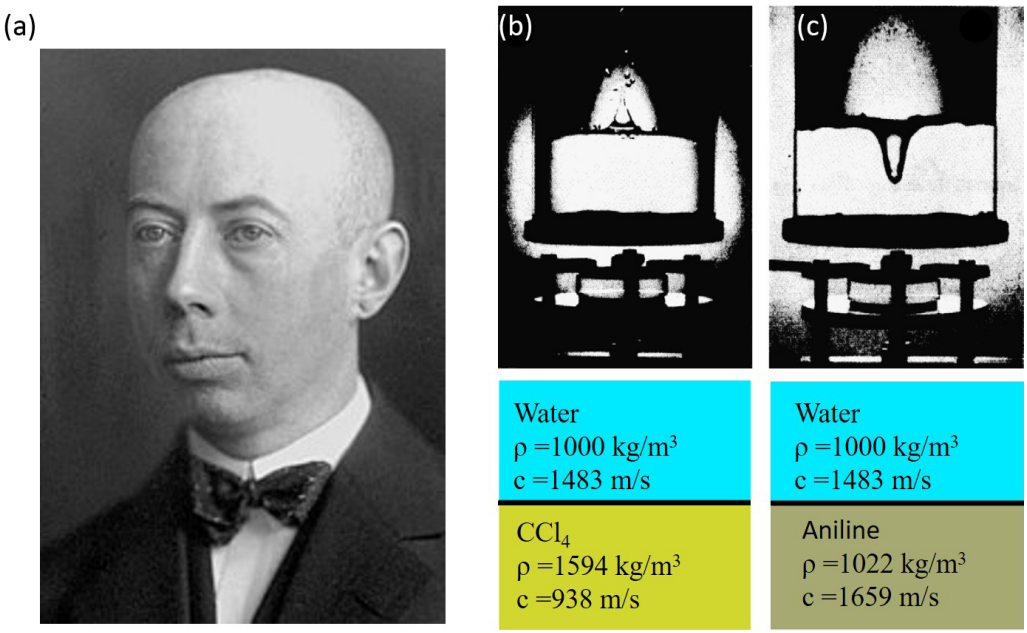

Figure 1.4: (a) Gustav Ludwig Hertz, German physicist, 1887-1975. Acoustic radiation force on an interface of two media with the properties of media shown in (b) and (c). Figure from Sarvazyan et al.[1]

Figure 1.5: Lev Petrovich Gor'kov, Russian-American physicist, 1929-2016. Figure from American Institute of Physics.

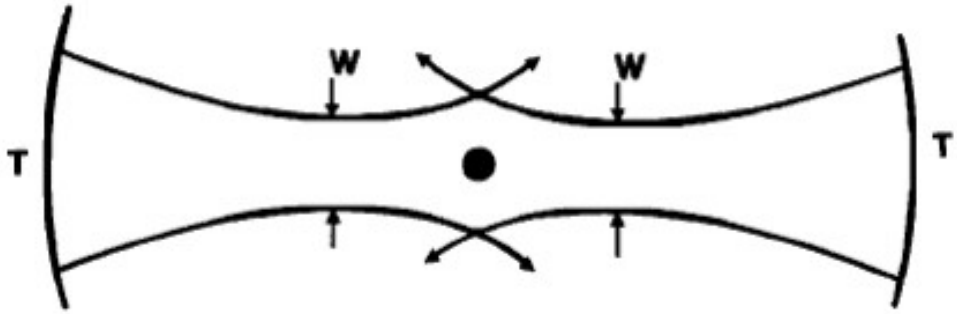

Figure 1.6: A particle is trapped by two focused ultrasound beams. Figure from Wu.[2]

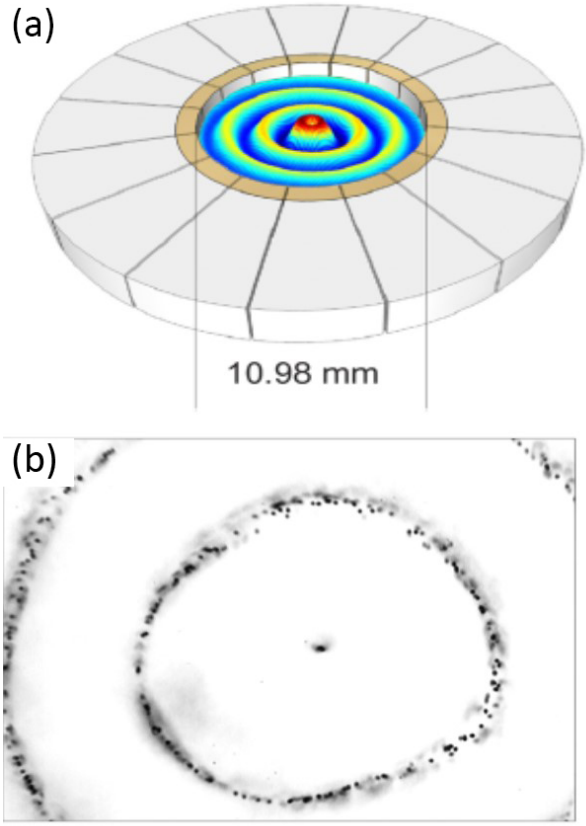

Figure 1.7: Particle manipulation by acoustic cylindrical standing waves generated by a circular speaker array of 16 elements. Figure from Courtney et al.[3]

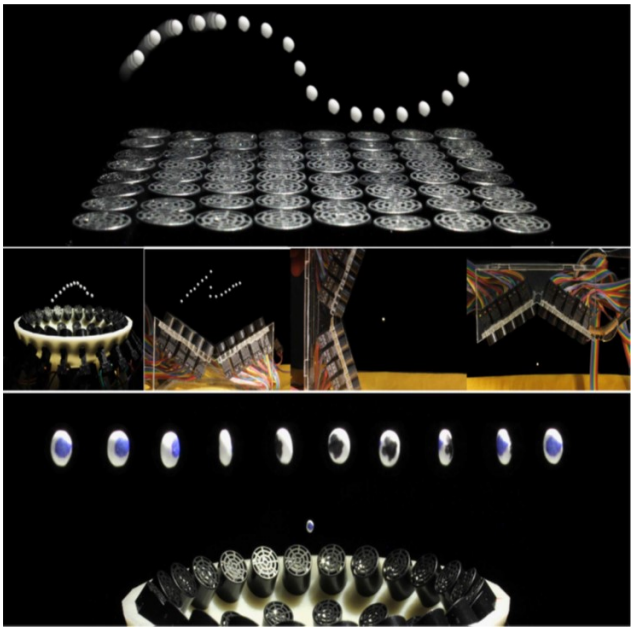

Figure 1.8: Particle manipulation including moving and rotating particles using acoustic transducer arrays. Figure from Marzo et al.[4]

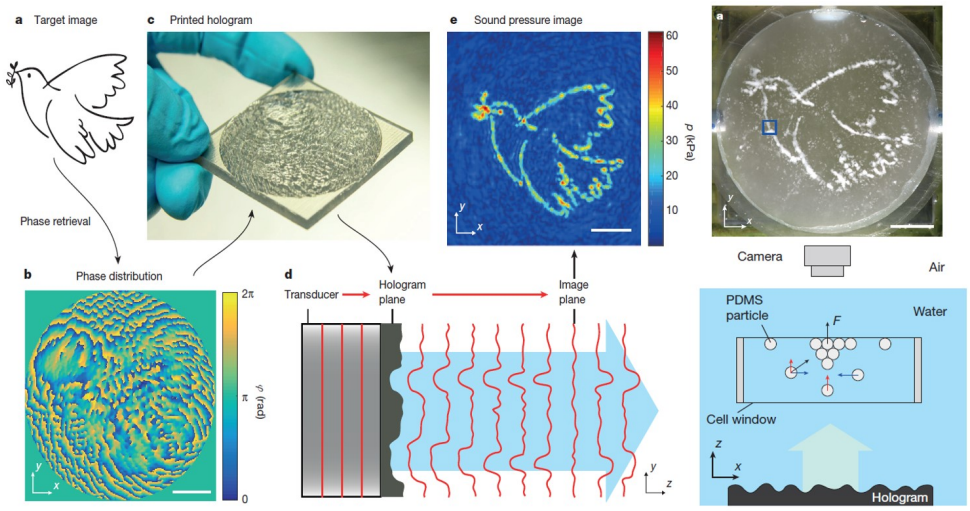

Figure 1.9: Particle manipulation using acoustic histograms. Particles can be trapped into pre-designed pattern. Figure from Melde et al.[5]

object. The momentum-flux tensor $\overleftrightarrow{T}$ can be written as,[1]

$$\overleftrightarrow{T} = \left[\frac{1}{2\rho_0 c_0^2} p^2 - \frac{\rho_0}{2} v^2\right] \mathbf{I} + \rho_0 \mathbf{v}\mathbf{v}, \tag{1.1}$$

where $\mathbf{I}$ is unit diagonal tensor, p and v are the total acoustic pressure and particle velocity. Therefore, the total acoustic radiation force can be represented by

$$\mathbf{F} = -\oint_S \langle \overleftrightarrow{T} \rangle \cdot \mathbf{n} ds, \tag{1.2}$$

where $\mathbf{n}$ is the vector of outward normal to the closed surface S surrounding the volume V. It is worth noting that the acoustic radiation force in an ideal fluid can be determined by integration of time-averaged momentum-flux tensor $\langle \overleftrightarrow{T} \rangle$ over an arbitrary closed surface enclosing the objects with complex shapes, internal structures, or spatially dependent properties since the force only depends on the total acoustic pressure and particle velocity around the objects caused by scattering.

Acoustic radiation forces on small objects within acoustic fields that possess strong spatial gradients of the energy density can be obtained from the negative gradient of the Gorkov potential

U,[12] i.e.,

$$\mathbf{F}^{\text{rad}} = -\nabla U. \tag{1.3}$$

The Gorkov potential follows from Eq. (1.2) by expressing the total fields as a summation of the incident field and the scattering field, and then keeping the leading order of the scattering field at the small object limitation that is dominated by the monopolar and dipolar terms.

Together with some mathematical operations, the Gorkov potential[12] was obtained as

$$U = (\pi a^3/3)[f_1 p^2/(\rho_0 c_0^2) - (3/2) f_2 \rho_0 \mathbf{v}^2], \tag{1.4}$$

where a is the radius of the object, ρ_0 and c_0 are the mass density and the sound speed of the background medium, and f_1 and f_2 are the monopole and dipole factors,

$$f_1 = 1 - K_0/K_s, \;\; f_2 = 2(\rho_s - \rho_0)/(2\rho_s + \rho_0), \tag{1.5}$$

depending on the mass density (ρ) and bulk modulus (K) of the object (indicated by the subscript s) and the surrounding medium (indicated by the subscript 0).[19]

1.3 Born approximation

For non-spherical objects or when the materials inside the objects are not uniform, the Born approximation method can be used to analyze the trapping force. The Born approximation method also allows for spatial variations of the density and compressibility within the particle, which is another significant advantage.

The Born approximation[20] was first proposed by Max Born in the early days of quantum theory development. It is a perturbation method dealing with the scattering problem on an external body. The Born approximation takes the incident field in place of the total field as the driving field at each point in the scatterer, and it is accurate when the scattered field is small compared to the incident field on the scatterer.

Although the Born approximation was originally introduced to solve quantum scattering problems, it can be adapted to acoustics for the analysis of scattering on weakly scattering objects.[21–23] Under the Born approximation, the acoustic scattered field from the whole object can be considered as a summation of the individual scattered field from each infinitesimal volume element within the object. The prerequisite for the Born approximation in acoustics is the same as that in quantum mechanics, i.e., the scattered field is much smaller than the incident field. This conclusion is met when the density and compressibility of the particle are not substantially different from those of the surrounding media. This condition is admissible for a variety of biological media and other soft materials.[24,25] One advantage of the Born approximation method is that the scattering problem can be approximately solved by considering only the monopole and dipole terms even when the size of the particle is beyond the Rayleigh regime (characteristic length is much smaller than the wavelength), in contrast to the usual method where high-order terms would be needed.

Based on the Born approximation method, the radiation force acting on particles can be also obtained by integrating over the force acting on each infinitesimal volume element within the object, where only the monopole and dipole contributions to the force need to be considered. The Born approximation method can only be used for forces due to the gradient of sound fields like standing waves where the trapping force is proportional to the volume of the particle when the particle is small [i.e., $f \propto (ka)^3$ with k being the wavenumber and a being the radius of the object].[12] In contrast, the pulling force is associated with traveling sound waves, where the force is proportional to the square of the volume for small particles [i.e., $f \propto (ka)^6$],[13] prohibiting the integration over a volume of finite size. The former type of force is usually called the gradient force, which can be expressed in terms of the gradients of the local potential and the kinetic energy densities in the sound field.[12] The latter force is usually called the scattering force since it is associated with scattering from the object in progressive waves.

Analysis of the Born approximation for one-dimensional plane standing waves[26] or progressive spherical waves[27] has been presented. Using the Born approximation, some integral expressions were obtained for the acoustic radiation force acting on a soft compressible object of

arbitrary shape and orientation with respect to the incident plane standing wave. The integral expressions for one-dimensional standing waves were reduced to 1D integrals for some cases, which can simplify numerical calculations and even enables analytical integration for certain geometries. The available range of parameters, for which the Born approximation method for 1D standing waves is accurate, was also indicated.

The focus here is on acoustic Bessel and vortex waves. Compared with *one* dimensional standing waves, *three* dimensional waves might be more flexible for the particle manipulations since there are more variables to control for three-dimensional waves.

1.4 Phase shift from scattering

The acoustic radiation force acting on objects has been derived from either the integration of the Langevin-Westervelt stress or the calculation of momentum transfer associated with the scattering.[13–15,18,19,28–49] The force is commonly expressed in terms of the partial wave expansion containing coefficients of the scattered field that depend on the properties of the particle and the surround medium. For a plane wave $p = p_0 \exp(ikz - i\omega t)$, the partial wave expansion of the total field on a spherical particle is[42]

$$p = p_0 \sum_{n=0}^{\infty} (2n+1) i^n \left[\underbrace{j_n(kr)}_{\text{incident}} + \underbrace{c_n h_n^{(1)}(kr)}_{\text{scattered}} \right] P_n(\cos\theta), \tag{1.6}$$

in which θ is the scattering angle, P_n is the Legendre polynomial, and j_n and $h_n^{(1)}$ are the spherical Bessel and Hankel functions of the first kind, respectively. Here a $\exp(-i\omega t)$ time dependence is suppressed. The partial wave scattering coefficients c_n, determined from the continuity of displacement and stress at the surface of the object, have been well studied for incident plane wave on an isotropic sphere. The corresponding dimensionless axial radiation force Y_z is usually expressed using real parts α_n and imaginary parts β_n of the partial wave coefficients c_n ($c_n = \alpha_n + i\beta_n$)

in a well-known form,[42]

$$Y_z = -\frac{4}{(ka)^2}\sum_{n=0}^{\infty}(n+1)\left[\alpha_n + \alpha_{n+1} + 2(\alpha_n\alpha_{n+1} + \beta_n\beta_{n+1})\right], \tag{1.7}$$

where the force is normalized by $F_0 = \pi a^2 I_0/c_0$ with $I_0 = p_0^2/(2\rho_0 c_0)$ being acoustic intensity. a is the radius of the spherical object, and ρ_0, c_0 are the density and sound speed of the background medium, respectively.

Recently, Zhang and Marston imported the complex phase shifts into acoustics from quantum scattering theory to greatly simplify the analytical expressions for the radiation force.[42,43] The complex phase shifts η_n are related to the partial wave coefficients c_n through the partial wave scattering function s_n,

$$c_n = \frac{s_n - 1}{2} \text{ with } s_n = e^{i2\eta_n} \text{ and } \eta_n = \delta_n + i\gamma_n. \tag{1.8}$$

With the aid of the scattering function s_n, the total field in Eq. (1.6) can be rewritten in terms of ingoing and outgoing spherical waves

$$p = p_0\sum_{n=0}^{\infty}\frac{(2n+1)}{2}i^n\left[\underbrace{h_n^{(2)}(kr)}_{\text{ingoing}} + \underbrace{s_n h_n^{(1)}(kr)}_{\text{outgoing}}\right]P_n(\cos\theta), \tag{1.9}$$

where $h_n^{(2)}(kr)$ is the Hankel function of the second kind and $j_n(kr) = [h_n^{(1)}(kr) + h_n^{(2)}(kr)]/2$ is used during the calculation. It is now clear that the scattering function s_n represents the reflection coefficient of ingoing spherical waves being reflected by the object. As a result, $|s_n| \leq 1$, where all $|s_n| = 1$ only when there is no dissipation in both the particle and the boundary layer surrounding the particle.[50] Imaginary parts of the phase shifts γ_n ($\gamma_n \geq 0$) represent the dissipation.

With the aid of the phase shifts in Eq. (1.8), the radiation force expression for incident plane wave in Eq. (1.7) is greatly simplified. It assumes a very simple form when the dissipation is not

taken into account (i.e., $\gamma_n = 0$), where Eq. (1.7) becomes[42]

$$Y_z = \frac{4}{(ka)^2}\sum_{n=0}^{\infty}(n+1)\sin^2(\delta_n - \delta_{n+1}). \tag{1.10}$$

One advantage of importing phase shifts into radiation forces appears immediately: one can directly tell from Eq. (1.10) that the radiation force for incident plane wave on ordinary objects can never be negative unless the targets are active ($|s_n| > 1$ or $\gamma_n < 0$; see examples in Ref.[51–54]). It is worth noting that although the individual series of the ingoing or outgoing wave is divergent [Eq. (1.9)],[50,55,56] the sum of the ingoing and outgoing waves are convergent [Eq. (1.6)], and the expression of the radiation force involving the difference of adjacent phase shifts [Eq. (1.10)] is also convergent.

The phase shift method is not restricted to the incident plane wave, instead it can be applied to an arbitrary field.[14] Consider the arbitrary field scattering from an isotropic sphere with the total field expressed as[50]

$$p = p_0\sum_{n=0}^{\infty}\sum_{m=-n}^{n} a_{nm} i^n \left[j_n(kr) + c_n h_n^{(1)}(kr)\right] Y_{nm}(\theta,\phi), \tag{1.11}$$

where the beam shape coefficients a_{nm} vary for different incident sound beams and the spherical harmonics are

$$Y_{nm}(\theta,\phi) = \sqrt{\frac{(2n+1)}{4\pi}\frac{(n-m)!}{(n+m)!}} P_n^m(\cos\theta) e^{im\phi}. \tag{1.12}$$

Note that the scattering coefficients for an arbitrary incident field on spherical objects are identical to the case of incident plane waves.

Using the scattering function s_n to express the total field as a sum of ingoing and outgoing spherical waves, the three-dimensional radiation force for arbitrary fields was recently obtained by Zhang[50] in a simple form as:

$$\mathbf{Y} = \frac{1}{4\pi(ka)^2}\sum_{n=0}^{\infty}\sum_{m=-n}^{n} \mathrm{Re}[(1 - s_n s_{n+1}^*)\mathbf{b}_{nm}], \tag{1.13}$$

where the vector $\mathbf{b}_{nm}$ is a function of adjacent beam shape coefficient a_{nm},

$$
\begin{aligned}
b_{nm}^{x} &= -(a_{nm}a_{n+1,m+1}^{*} - a_{n,-m}a_{n+1,-m-1}^{*})h_{n}^{m,-m-1} \\
b_{nm}^{y} &= i(a_{nm}a_{n+1,m+1}^{*} + a_{n,-m}a_{n+1,-m-1}^{*})h_{n}^{m,-m-1} \\
b_{nm}^{z} &= (2a_{nm}a_{n+1,m}^{*})h_{n}^{m,m}
\end{aligned}
\tag{1.14}
$$

with

$$
h_{n}^{m,m'} = \sqrt{\frac{(n+m+1)(n-m'+1)}{(2n+1)(2n+3)}}. \tag{1.15}
$$

In terms of complex phase shifts for s_n given in Eq. (1.8), the radiation force is expressed as a summation of functions of adjacent complex phase shifts involving the difference of the real parts $(\delta_n - \delta_{n+1})$ and the sum of the imaginary parts $(\gamma_n + \gamma_{n+1})$, i.e.,

$$
1 - s_n s_{n+1}^{*} = 1 - e^{-2(\gamma_n+\gamma_{n+1})}e^{i2(\delta_n-\delta_{n+1})}. \tag{1.16}
$$

With the aid of phase shifts, the expression of acoustic radiation force is simplified into a compact and physically meaningful form, which is beneficial to the analysis and design of acoustic radiation force. The import of the phase shifts actually provides an efficient way to engineer desired radiation forces.[42,43] The desired force is fulfilled by a specific set of phase shifts from scattering, and the problem of obtaining the desired force is then simplified to finding the desired phase shifts. Next, the set of phase shifts is used to engineer the object and beam parameters efficiently and even analytically since the problem has been reduced to a well-studied scattering problem.

1.5 Acoustic streaming and particle motion

When considering practical situations, the effect caused by the acoustic streaming may need to be included. Acoustic streaming is a net mean flow generated by a nonlinear acoustic wave with a finite amplitude in a viscid fluid. It depends on the geometry of the acoustic system, boundary conditions, and the properties of the incident waves. Based on the generation mechanisms, acoustic

streaming can be classified into several groups: (i) the "boundary layer driven streaming", where the flow is induced by the shear viscosity close to a boundary. Specifically, the mean fluid motion outside the boundary layer is usually referred as the "outer streaming" or "Rayleigh streaming",[57] and the mean fluid motion inside the boundary layer is referred as "inner streaming" and first analyzed by Schlichting;[58] (ii) the "bulk dissipation driven streaming", where the net flow is generated by the high amplitude acoustic source (usually in high frequency range), and the dissipation within the fluid. This kind of streaming was first analyzed by Eckart;[59] (iii) "jet driven streaming", which is associated with the periodic suction and ejection of a viscous fluid through an orifice and the behaviors of the viscid fluid are quite different during the different phases;[60] and (iv) "traveling wave streaming", which is related to travelling waves.[60] These different types of streaming can and usually do occur simultaneously in practice.

The motion of a particle (with the mass of m) suspended under the acoustic radiation force $\mathbf{F}^{\mathrm{rad}}$, gravity $\mathbf{F}^{\mathrm{G}}$, buoyancy $\mathbf{F}^{\mathrm{B}}$, and the Stokes drag force $\mathbf{F}^{\mathrm{D}}$ can be described as follows based on the Newton's law:

$$m\frac{d\mathbf{u}}{dt} = \mathbf{F}^{\mathrm{rad}} + \mathbf{F}^{\mathrm{G}} + \mathbf{F}^{\mathrm{B}} + \mathbf{F}^{\mathrm{D}}, \tag{1.17}$$

where $\mathbf{u}$ is the velocity of the particle, which can be solved based on the equation above.

1.6 Acoustic Bessel and vortex beams

An acoustic Bessel beam/wave is a special wave whose amplitude can be described by a Bessel function of the first kind. The pressure field $\mathrm{Re}[p(\mathbf{r},t)]$ (Re denotes real part) of the Bessel beam can be expressed in the cylindrical coordinates,

$$p = p_0 J_l(\mu\rho)\exp(i\kappa z + il\phi - i\omega t), \tag{1.18}$$

where p_0 is a real-valued amplitude, J_l is Bessel function with topological charge of l, $\mathbf{r}(\rho,\phi,z)$ is the field point in cylindrical coordinates, and the transverse wavenumber μ and axial wavenumber κ are related to the total wavenumber $k = \sqrt{\mu^2+\kappa^2} = \omega/c_0$ (c_0 is sound speed in the surrounding

media) through a paraxiality parameter β with $\mu = k \sin\beta$, and $\kappa = k \cos\beta$.

Acoustic Bessel waves are non-diffractive. When the topological charge $l = 0$, the Bessel beam is an ordinary axisymmetric beam with a central pressure maximum, however, when $l \neq 0$, the Bessel beams are vortex beams with a central pressure null. An ideal Bessel beam does not exist in the real world since it is unbounded and would require an infinite amount of energy. However, approximated Bessel waves can be created, so they exhibit little or no diffraction over a limited range, which is roughly equal to the half length of the source divided by the tangent angle of β.

1.7 Vortex beams in inhomogeneous media

The second portion of the dissertation focuses on the behaviors of acoustic vortex beams in inhomogeneous media. With a spiral phase $\exp(im\phi)$ proportional to the azimuth angle ϕ, acoustic vortex beams carry orbital angular momentum (OAM).[18,61–65] The orbital angular momentum, proportional to the integer m, is produced by the circulation of the phase. The integer m is the topological charge of the vortex and the field has a null at the core. Acoustic waves generated by phased spiral sources or physically spiral sources[66] can be used in many applications, especially in particle manipulations,[4,5,18,62,63,67–78] underwater navigation,[79] and communications.[80,81] There is also interest in using vortex beams for ultrasonic alignment,[61] imaging,[82] and therapy.[83]

The propagation of optical vortices through an inhomogeneous medium was considered in the scalar approximation by Aksenov et al.[84] where a theoretical approach was proposed to address the problem of singular fields in the context of improving optical systems in the turbulent atmosphere. However, prior studies on acoustic vortices were limited to homogeneous media, with an exception that simulated paraxial propagation of nonlinear vortices in weakly heterogeneous media.[65] When considering practical situations or applications, the media commonly has spatially varying parameters. For example, in deep ocean environments, the sound speed is a function of depth, resulting from the temperature and salinity stratification, and pressure variation.[85,86] In biomedical ultrasound, the sound speed has a large variation crossing tissues.[87–89] Hence, it is of fundamental and practical interests to study the propagation of wave vortices and transport of OAM

in heterogeneous media.

1.8 Hall effect

The Hall effect, sometimes called the ordinary Hall effect, was first discovered by American physicist Edwin H. Hall in 1879[90] while he was working on his doctoral degree at Johns Hopkins University in Baltimore, Maryland. The effect states that when an electric current flows through an conductor placed in an external magnetic field, a voltage difference across the conductor (so called the Hall voltage) transverse to the electric current and to the magnetic field is produced. The Hall effect is due to the accumulation of moving electric charge carriers (electrons or holes) on one side of the material since these moving charge carriers experience a Lorentz force when an external magnetic field perpendicular to the electric current is present. Then equal and opposite charges develop on the other side. The separation of charges establishes an electric field that opposes the migration of further charges as long as the charges are flowing.

After about one century, a German Physicist, Klaus von Klitzing, made the first discovery of the quantum Hall effect[91] (or integer quantum Hall effect) , which is a quantum-mechanical version of the Hall effect, and it was observed in two-dimensional electron systems subjected to low temperatures and strong magnetic fields. For this finding, von Klitzing was awarded the 1985 Nobel Prize in Physics. Later, the fractional quantum Hall effect was experimentally discovered in 1982 by Tsui et al.[92] in experiments performed on gallium arsenide heterostructures developed by Arthur Gossard. In the quantum Hall effect, the Hall resistance, which is the voltage across the transverse direction of a conductor divided by the longitudinal current, is quantized as $h/\nu e^2$, where e is the elementary charge, h is Planck's constant, and ν could be an integer or a certain fraction. The quantum Hall effect has also been found in graphene at temperatures as high as room temperature.[93] The quantum Hall effect also provides an extremely precise independent determination of the fine structure constant, a quantity of fundamental importance in quantum electrodynamics.

The optical Hall effect, which comes from the interactions between different types of angular momentum, has been studied for a long time. Specifically, the spin-orbit interaction (the

coupling between spin angular momentum and extrinsic orbital angular momentum) leads to a mutual influence on the polarization and the trajectory of the beam center.[94–97] This spin-orbit coupling causes two effects: (i) a trajectory-dependent polarization variation characterized by the Berry phase, providing a parallel transport of the polarization vector along the ray; (ii) the spin Hall effect, which leads to the transverse shifts (so called Imbert-Fedorov shift[98]) in the reflection/refraction on a sharp boundary[99–103] or splitting of rays for different polarization in a smoothly inhomogeneous medium.[101,104–107] The Imbert-Fedorov effect can be considered as a special case of the spin Hall effect. The optical spin Hall effect is the photonic analogue of the electronic spin Hall effect, where the polarization of an incident light wave corresponds to the electron spin and the refractive index gradient of the material plays a role of an applied electric field.[108] These effects can be understood by the spin-orbit interaction and the conversion of the normal component of total angular momentum.[95,101–104]

Apart from the spin Hall effect caused by the interaction between the polarization and extrinsic orbital features, similar topological phenomena caused by the interaction between intrinsic and extrinsic orbital angular momentum, i.e. orbital Berry phase and the orbital Hall effect were also found.[94,109–115] Large values of intrinsic orbital angular momentum compared to the spin polarization can dramatically enhance and rearrange the topological phenomena. Similarly, the 'orbital' Imbert-Fedorov effect can be considered as a special case of the orbital Hall effect regarding either the singular point[94] or the gravity center of the vortex beam[116–118].

The topological phenomena and effects in optics mentioned above have been found and studied for a long time, however, the study of topological acoustics is only a few years old,[119–137] and the Berry geometric phase effect in acoustics was not reported until recently by Wang et al.[138] and Ma et al.[133] where the Berry phase associated with the helical transport of sound was described and measured via a twisted pipe in the air. The reflection of an obliquely incident acoustic vortex beam on the water-air interface was also studied recently by Zou et al.[139] numerically and experimentally. Nevertheless, the Hall effect associated with acoustic vortex beams has not been explored.

1.9 Organization of the dissertation

The dissertation is organized as follows. Chapter 2 systematically analyzes the trapping behaviors of small spherical objects located at the Bessel and vortex beam axis, and also suggests the possibility of achieving acoustic tractor beams. Chapter 3 studies the trapping behaviors on arbitrary objects with the aid of the Born approximation, especially for large objects. Chapter 4 analyzes the acoustic pulling force with the aid of the phase shifts. Chapter 5 discusses the forces caused by other effects, such as gravity, buoyancy and acoustic streaming. Chapter 6 studies the refraction of acoustic vortex beams in inhomogeneous media, and reports some unusual behaviors as the vortex beam propagates. Chapter 7 describes the acoustic orbital Hall effect for vortex beams during propagation in a continuously stratified medium. Chapter 8 analyzes a special case of the acoustic orbital Hall effect which occurs on the sharp boundary between two media, i.e., the acoustic Imbert-Fedorov effect, and also suggests the possible experiments for the observation of the acoustic orbital Hall effect. Chapter 9 makes a summary and conclusion about this dissertation.

CHAPTER 2

TRAPPING OF SMALL SPHERICAL OBJECTS

In this chapter, the trapping of spherical objects by acoustic Bessel and vortex beams is systematically examined, where the transverse trapping by acoustic Bessel beams can have some unusual and unique behaviors, different from trapping by standing waves and focused beams.

A particle centered on the central core of both axisymmetric beams (central pressure maximum) and vortex beams (central pressure minimum) is considered [Fig. 2.1], and they can be described by arbitrary-order Bessel beams propagating along a z axis with the pressure field $\mathrm{Re}[p(\mathbf{r},t)]$ (Re denotes real part) given by,

$$p(\mathbf{r},t) = p_0 J_l(\mu\rho)\exp(i\kappa z + il\phi - i\omega t), \tag{2.1}$$

where p_0 is a real-valued amplitude, J_l is Bessel function with topological charge of l, $\mathbf{r}(\rho,\phi,z)$ is the field point in cylindrical coordinates, and the transverse wavenumber μ and axial wavenumber κ are related to the total wavenumber $k = \sqrt{\mu^2+\kappa^2} = \omega/c_0$ (c_0 is sound speed in the surrounding media) through a paraxial parameter β with $\mu = k\sin\beta$, and $\kappa = k\cos\beta$.

2.1 Trapping of a rigid sphere

The transverse force $F_\rho = \pi a^2 (I_0/c_0) Y_\rho$ exerted on a spherical particle of radius a (with $I_0 = p_0^2/(2\rho_0 c_0)$ being acoustic intensity and ρ_0 being the density of surrounding media), where the dimensionless transverse force Y_ρ as a function of the transverse location R of the sphere off

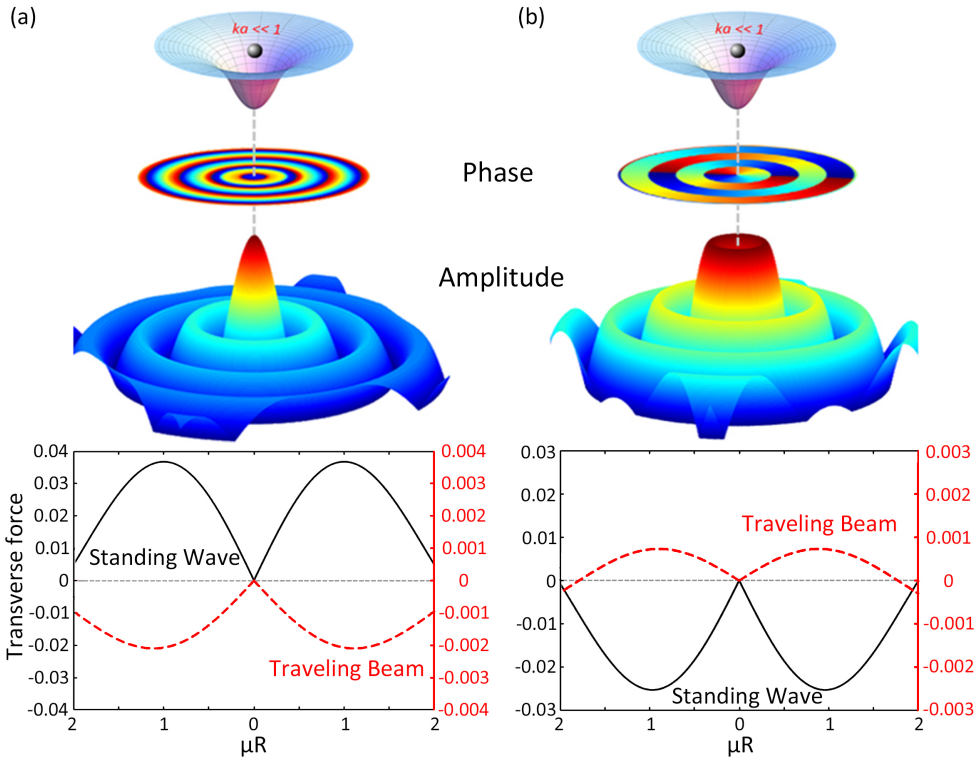

Figure 2.1: Transverse trapping of a rigid sphere of radius a ($ka = 0.05$ with k being wavenumber) using (a) axisymmetric beams and (b) vortex beams. The results of the traveling beams (paraxial parameter $\beta = 15°$; red dashed lines) are different from the results of standing waves ($\beta = 90°$; black solid lines), where paraxial parameter β is related to the axial wavenumber κ and transverse wavenumber μ by $\mu/\kappa = \tan\beta$. The fields are given by Eq. (2.1) with the topological charge $l = 0$ and 1, respectively.

the beam axis can be obtained from partial wave expansion; see Eq. (16) from Zhang,[18]

$$
\begin{aligned}
Y_\rho(R) &= \sum_{m=-\infty}^{\infty} K_m^+ B_m, \\
K_m^+ &= J_{l-m}(\mu R) J_{l-m-1}(\mu R) - J_{l+m}(\mu R) J_{l+m+1}(\mu R), \\
B_m &= \frac{1}{(ka)^2} \sum_{n=|m|}^{\infty} \frac{(n-m)!}{(n+m)!} P_n^m(b) P_{n+1}^{m+1}(b) \mathrm{Im}(s_n^\star s_{n+1}),
\end{aligned}
\tag{2.2}
$$

where $b = \cos\beta$, Im represents for imaginary part, and the scattering functions s_n[42] are determined by boundary conditions on the particle surface (see Appendix; $|s_n| = 1$ in the ideal case of no absorption). Note $K_m^+ = 0$ when $\mu R = 0$. The transverse force as a function of the object location R for a dense and rigid particle ($ka = 0.05$ and $\beta = 15^\circ$) is shown in Fig. 2.1. The results indicate that the rigid particle is trapped to the axis of axisymmetric beam (pressure maximum) and repelled away from the core of the vortex beam (pressure minimum), in contrast to the trapping behaviors by standing waves (relatively dense and stiff particles are trapped to pressure minimum by standing waves).

The contrasting behaviors can be understood by examining the contribution of the velocity component along the propagation direction to the force potential. In the Rayleigh regime, the transverse force is given by $F_\rho = -\partial U/\partial\rho$ where the gradient is along the transverse direction only, but the force potential U[12] depends on velocity in all three directions,

$$
U = (\pi a^3/3)[f_1|p|^2/(\rho_0 c_0^2) - (3/2) f_2 \rho_0 |\mathbf{v}|^2], \tag{2.3}
$$

in which the monopole and dipole factors,

$$
f_1 = 1 - 1/\kappa, \; f_2 = 2(\lambda - 1)/(1 + 2\lambda), \tag{2.4}
$$

depend on the mass density ratio and bulk modulus ratio of the particle to the surrounding media,

$$
\lambda = \rho/\rho_0, \; \kappa = K/K_0. \tag{2.5}
$$

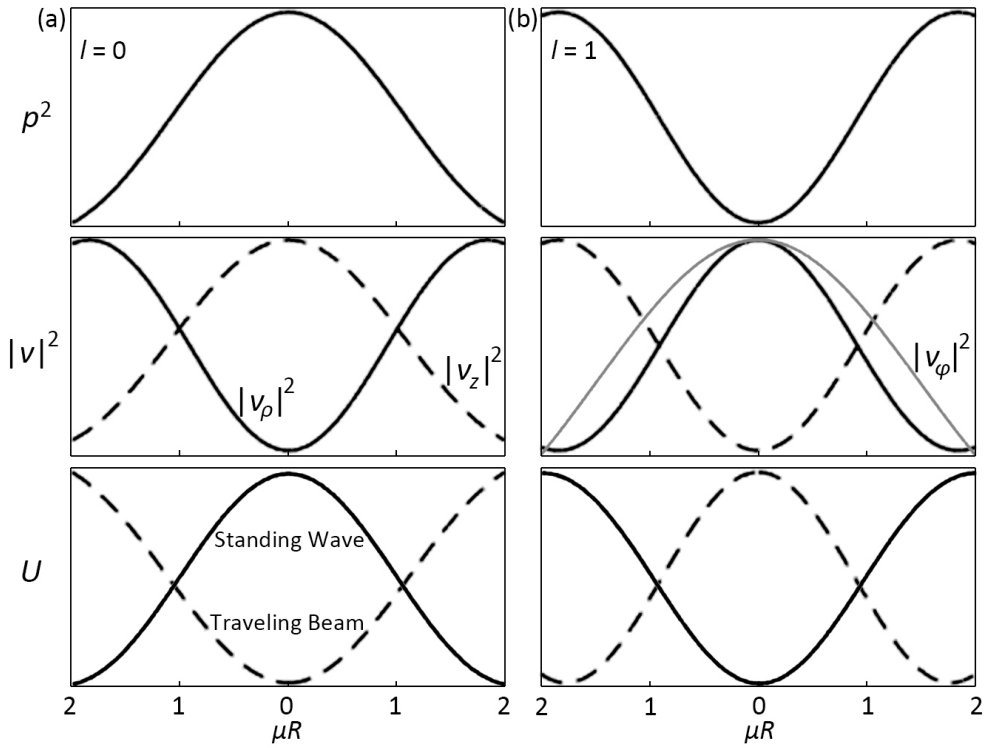

Figure 2.2: Contribution of pressure (top panels) and three components of velocity (center panels) to the potential (bottom panels) for (a) axisymmetric and (b) vortex beams. The reversal of the potential is due to the presence of axial velocity v_z (dashed lines); see Eq. (2.3). Arbitrary unit and normalization are used here.

For the axisymmetric beam [Fig. 2.2(a)], it is true that the transverse velocity has a central minimum coinciding with the pressure maximum, like planar standing waves, leading to a maximum of the Gor'kov potential for a relatively stiff and dense particle. However, the axial velocity component instead has a central maximum coinciding with the pressure maximum. As a result, it is possible to have a minimum potential for a stiff and dense ($f_{1,2} > 0$) or even for the extreme case of a rigid particle ($f_1 = 1$), as long as the particle is dense enough (large f_2). The minimum potential for a rigid particle of heavy mass ($f_{1,2} = 1$) centered on the axisymmetric beam is shown in Fig. 2.2(a). Similarly, for the vortex beam [Fig. 2.2(b)], the transverse and azimuthal velocity has a central maximum coinciding with the pressure minimum, like planar standing waves, leading to trapping of a relatively dense and stiff particle by the minimum of Gor'kov potential. However, the axial velocity component instead has a central minimum coinciding with the pressure minimum. As a result, a stiff and dense particle is repelled from the pressure null of vortex beams due to the maximum potential as shown in Fig. 2.2(b).

Given the projection of wave vectors associated with the paraxial parameter β, the transverse velocity is proportional to $\sin\beta$ while the axial velocity is proportional to $\cos\beta$:

$$v_\rho \propto \sin\beta,\ v_z \propto \cos\beta. \tag{2.6}$$

As such, reducing the paraxial parameter β reduces the transverse velocity and enhances the axial velocity. Consequently, the trapping is reversed when the β is reduced to be smaller than a critical value. The reversal occurs only when the density contrast is large enough [see Eq. (2.3)].

2.2 Variation of trapping with beam and material parameters

The above predictions of variation of the trapping with beam and material parameters are shown in Fig. 2.3 by the transverse gradient of the transverse force:

$$Slope = dY_\rho(R)/d(\mu R). \tag{2.7}$$

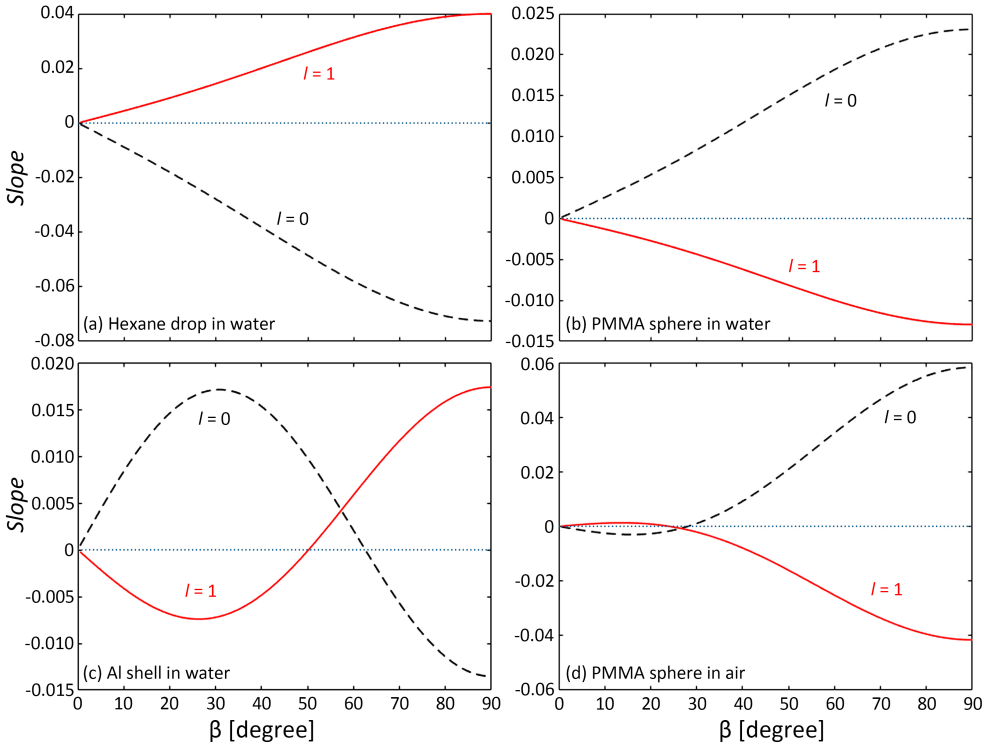

Figure 2.3: When varying the paraxial parameter β, the trapping is (a)-(b) preserved for small contrast of density or (c)-(d) reversed for large contrast of density, as denoted by sign of $Slope$ [see Eq. (2.7)] . The inner-to-outer radius ratio of the shell in (c) is 0.96; see material parameters in Table 8.1.

The results are for $Slope$ as a function of paraxial parameter β calculated from Eq. (2.2) with $ka = 0.05$ for four different contrasts of density and bulk modulus. At the non-propagating limit $\beta = 90°$, the results are in agreement with trapping by plane standing waves or trapping by Bessel-function fields: the light or soft particles are trapped at the pressure anti-node (local maximum) of axisymmetric waves [(a) and (c)], while dense and stiff particles are trapped at pressure node (local minimum) of vortex waves [(b) and (d)]. When reducing the β to change to a traveling beam, the results show exactly that the trapping is preserved when the density contrast is relatively small [(a) and (b)] and reversed when the density contrast is relatively large [(c) and (d)]. Meanwhile, the transition difference of β between $l = 0$ and $l = 1$ leads to the simultaneous repelling [see (c)] or trapping [see (d)] by both axisymmetric and vortex beams at β values between the two transitions, while it is generally true that the particles trapped by one beam are repulsed by the other.

The transverse force can be characterized in terms of a beam-parameter-dependent acoustic

Materials	Mass density ρ [kg/m^3]	Longitude wave speed c_L [m/s]	Transverse wave speed c_T [m/s]
Air	1.21	343	
Hexane	656	1078	
Water	1000	1500	
PMMA	1190	2690	1340
aluminum	2700 (311)	6420	3040

Table 2.1: Acoustic properties of materials in Fig. 2.3. The density 311 kg/m^3 is effective density of the aluminum shell calculated with the inner-to-outer radius ratio $b/a = 0.96$.

contrast factor Φ_l and the dimensionless transverse location μR explicitly,

$$Y_\rho = 2ka \sin\beta \Phi_l \times \mu R + O((\mu R)^2), \tag{2.8}$$

where $\sin\beta$ accounts for momentum projection to the transverse direction. For $l = 0$ and 1 beams, one obtains,

$$\Phi_l = \pm 2^{-l}\left[\frac{1}{3}f_1 + \left(\frac{3+l}{4}\sin^2\beta - \frac{1}{2}\right)f_2\right], \tag{2.9}$$

which follows from: (a) the Gor'kov potential Eq. (2.3) where the velocity is $\mathbf{v} = \nabla p/(i\omega\rho_0)$ with the pressure p given by Eq. (4.1), or (b) the partial wave expansion Eq. (2.2) where only the monopole and dipole terms are kept and the partial wave coefficients for small ka approximation are used:[43]

$$s_0 = 1 - i(2/3)(ka)^3 f_1 - (2/9)(ka)^6 f_1^2, \tag{2.10a}$$

$$s_1 = 1 + i(1/3)(ka)^3 f_2 - (1/18)(ka)^6 f_2^2. \tag{2.10b}$$

The small μR approximation was applied, $J_m(\mu R) \approx (\mu R/2)^m/m!$ (with m being an non-negative integer and $J_m(x) = (-1)^m J_{|m|}(x)$ for a negative integer m). In Eq. (2.2), $K_m(\mu R)$ is then a series in μR, where the contribution to the first order term is only from $m = \pm l$ and $m = -1 \pm l$, which illustrates the coupling of the adjacent order resulting from the transverse projection of

momentum.[50] The sign difference in Eq. (2.9) shows the complement stability between $l = 0$ beam (plus sign) and $l = 1$ beam (minus sign).

Equation (2.9) shows the dependence of the acoustic contrast factor on the beam parameters (β and l) and material parameters (λ and κ). Multiple parameter dependence in the stability diagram is displayed in Fig. 2.4, where the β value for the transition $\Phi_l(\beta) = 0$, denoted by β_l, is illustrated by the colormap. The two transition limits of $\beta_l = 0°$ (at $f_1/f_2 = 3/2$) and $\beta_l = 90°$ (at $f_1/f_2 = -3(1 + l)/4$) divide the stability diagram into four regimes for four types of trapping [Table 2.2]. When varying the paraxial parameter β over the whole 90° range, the trapping is preserved or reversed for materials for which the density contrast is relatively small (I and II) or large (III and IV). Note that, in regime IV (or III), there always exists $\beta_1 \leq \beta \leq \beta_0$ for the particle to be trapped at (or be repulsed away from) both the central pressure maximum of axisymmetric beams and minimum of vortex beams, while particles in regimes I and II are always trapped by one beam and repulsed by the other [Table 2.2].

The four cases calculated in Fig. 2.3 respectively fall into the four regimes in Fig. 2.4 with the contrast factors given by Eq. (2.4) with the bulk modulus being $K_0 = \rho_0 c_0^2$ for background medium, $K = \rho c^2$ for a droplet, and $K = \rho[c_L^2 - (4/3)c_T^2]$ for an elastic sphere with c_L and c_T being the longitudinal and transverse wave velocities of the material, respectively. For a hollow elastic shell with an inner-to-outer radius ratio b/a, the density ρ and bulk modulus K should be replaced by effective mass density and effective bulk modulus:

$$\rho_{\text{eff}} = [1 - (b/a)^3]\rho, \; K_{\text{eff}} = \frac{[1 - (b/a)^3]K}{1 + (b/a)^3[0.75(c_L/c_T)^2 - 1]}, \tag{2.11}$$

which follow from s_n in the Appendix and agree with the expressions in Zhou et al.[140] and Leão-Neto et al.[141] for more complex situations.

Importantly, dense and stiff particles (regimes IV in Fig. 2.4) can now be trapped by the axisymmetric beam with a small paraxial parameter β, in contrast to vortex beams which require a large paraxial parameter. This result suggests a new way to realize trapping of a dense and stiff

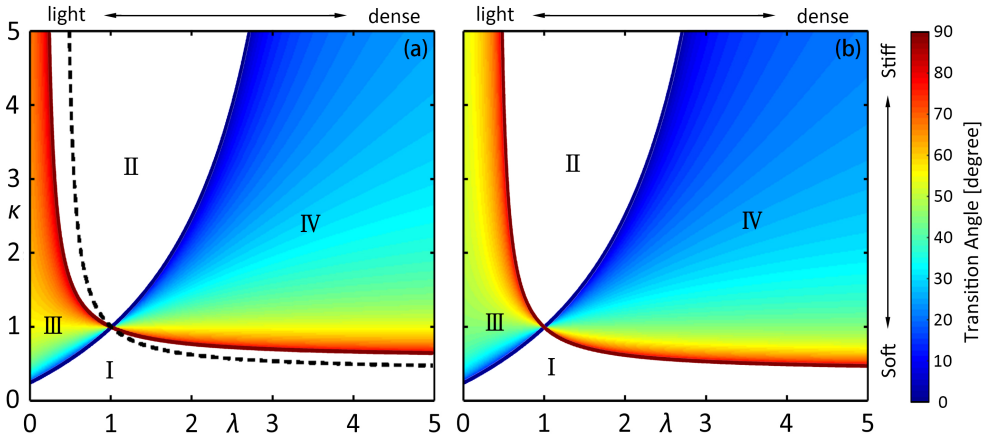

Figure 2.4: Stability diagram for (a) $l = 0$ and (b) $l = 1$ beams, illustrating transition of trapping at a critical paraxial parameter β_l (colorbar) in the parameter space of density ratio λ and bulk modulus ratio κ [see Eq. (2.5)]. See Table 2.2 about the stability features of the four regimes I-IV divided by the two boundaries, $f_1/f_2 = 3/2$ (increasing curve) and $f_1/f_2 = -3(1+l)/4$ (descending curve), following from Eq. (2.9). For comparison, the dashed line in (a) illustrates boundary of transition for plane standing wave trapping, $f_1/f_2 = -3/2$, overlapped with the $\beta = 90°$ standing wave boundary in (b).

	I	II	III	IV
Axisymmetric beam ($l = 0$)	stable for all β	unstable for all β	stable for $\beta > \beta_l$	stable for $\beta < \beta_l$
Vortex beam ($l = 1$)	unstable for all β	stable for all β	stable for $\beta < \beta_l$	stable for $\beta > \beta_l$

Table 2.2: Stability transition for the four regimes in Fig. 2.4.

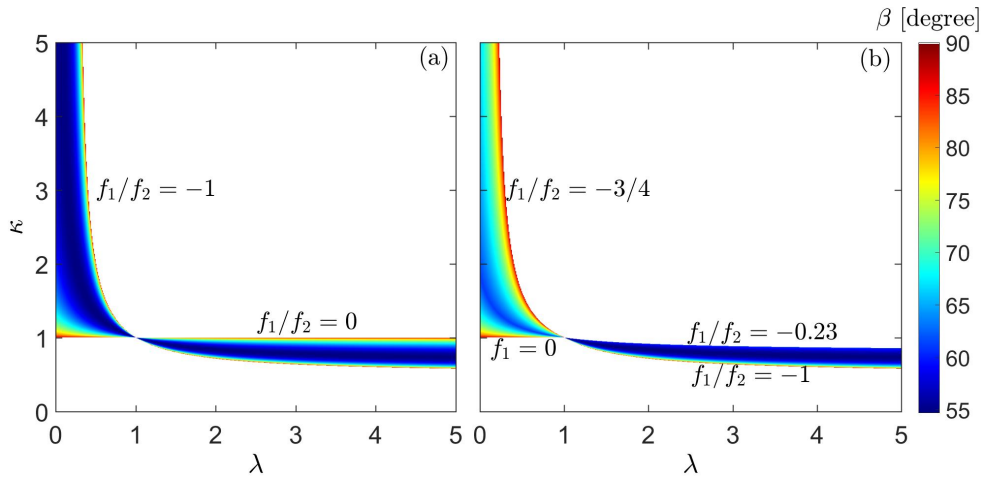

Figure 2.5: Diagrams for (a) pulling and (b) simultaneous trapping and pulling of a Rayleigh particle in the parameter space of (λ, κ), with the colorbar illustrating the minimum paraxial parameter required for the axisymmetric $l = 0$ Bessel beam. The values of f_1/f_2 on the boundaries are determined by Eqs. (2.9) and (2.12).

particle in a simple scheme by using a small β axisymmetric beam, instead by the relatively complex scheme by vortex beams. For a rigid sphere in the dense limit, the trapping is for $\beta < 28°$ using axisymmetric beam and for $\beta > 24°$ using $l = 1$ vortex beams [$f_1 = 1$ and $f_2 = 1$ in Eq. (2.4)].

2.3 Stable tractor beams

A stability diagram is used to seek the stable trapping in situations where the object is simultaneously pulled towards the beam source (namely, a *stable* tractor beam[13–15,37]). By using the axisymmetric Bessel beam, the stability diagram Fig. 2.5 shows that the simultaneous trapping and pulling of a Rayleigh particle is favored for relatively stiff and light particles in Regime III or relatively soft and dense particles in Regimes I and IV, where the trapping can be achieved by using a large paraxial parameter β that is also favoured by momentum projection to pull particles.[14]

Consider the $l = 0$ beam, coupling between the scattered monopole and dipole field leads to the axial radiation force $F_z = \pi a^2 (I_0/c_0) Y_z$ with,

$$Y_z = \frac{1}{9}(ka)^4 f_2^2 \cos\beta [(1 + 2f_1/f_2)^2 + 2P_2(\cos\beta)], \tag{2.12}$$

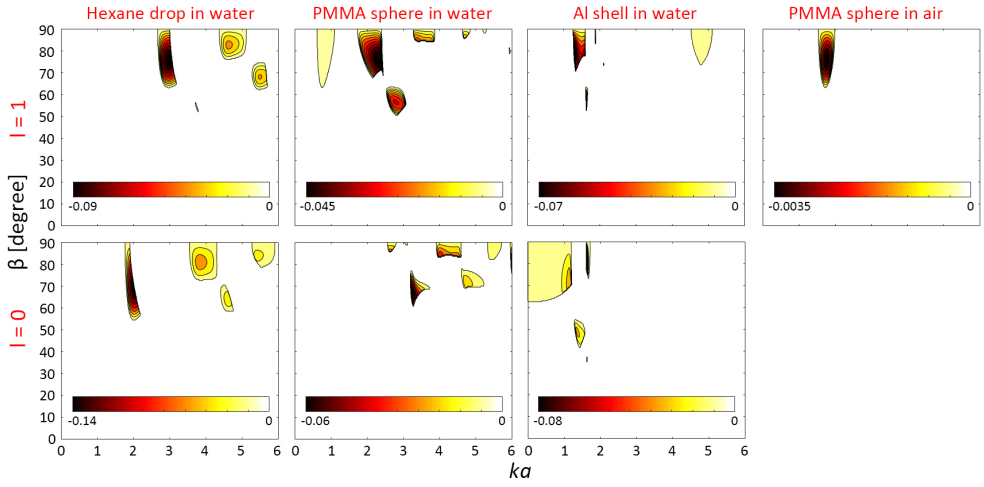

Figure 2.6: Contour plots of dimensionless radial negative force in the parameter space of (ka, β) where particles are simultaneously trapped and pulled. The results are for $l = 1$ (upper panels) and $l = 0$ (bottom panels). Only the aluminum shell is stably pulled by axisymmetric beam in Rayleigh regime because the aluminum shell lies in the stable pulling region in Fig. 2.5 [(λ, κ)=(0.31, 1.44)].

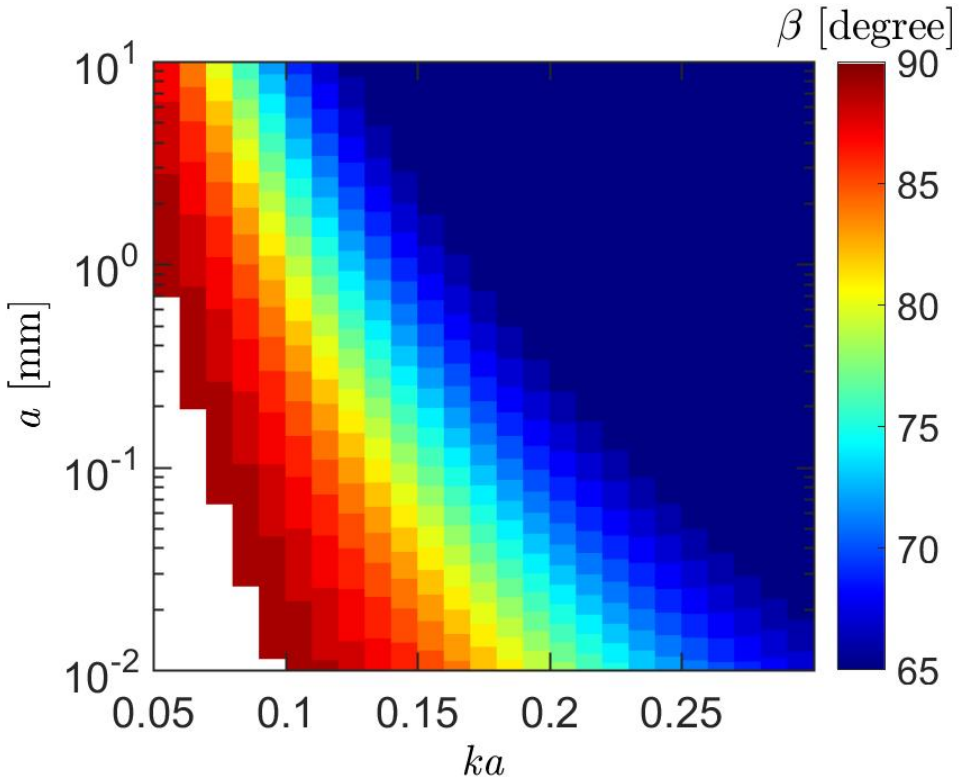

Figure 2.7: Minimum β for simultaneous pulling and trapping of an empty aluminum shell centered on the axis of axisymmetric Bessel beams in the parameter space (ka, a) when the loss correction is included. At the small ka and a values, β approaches to 90° (white region).

which is Eq. (15) in Marston [13] and the Legendre function $P_2(\cos\beta) = (3\cos^2\beta - 1)/2$. Given the material parameters, the force is negative when β is larger than a critical angle given by $Y_z(\beta) = 0$. The minimum β value is about 55° for particles with material contrast $f_1/f_2 = -1/2$. Larger β fulfills a larger region of negative force in the parameter space of mass density ratio and bulk modulus ratio. The negative force exists for materials contrast in the regime bounded by $f_1/f_2 = -1$ and $f_1/f_2 = 0$ [Fig. 2.5(a)].

Regions for simultaneous trapping and pulling a small particle is obtained by combining Eqs. (2.9) and (2.12) or combining Figs. 2.4(a) and 2.5(a) *per sa*. The results are shown in Fig. 2.5(b) with the color-plots illustrating the minimum parameter β required. The minimum β is determined by the critical values for pulling in Fig. 2.5(a) and for trapping in Fig. 2.4(a). In the region $\lambda > 1$, for $f_1/f_2 > -3/4$, the β also needs to be less than the critical angle for stable trapping in Regime IV of Fig. 2.4(a). The boundary $f_1/f_2 = -0.23$ in Fig. 2.5(b) corresponds to the situation when the minimum β angle for pulling equals to the maximum β angle for trapping. Hence, the beam and material parameters for the simultaneous pulling and trapping of a Rayleigh particle is identified.

For other material parameters outside that shown in Fig. 2.5(b), one would have to use a ka outside the Rayleigh regime to achieve the simultaneous trapping and pulling; see Fig. 2.6. The results are calculated from the dimensionless forces Y_ρ and Y_z from Eq. (16) in Zhang [18] (with $R = 0$ therein; see also Zhang [142]). In the Rayleigh regime [Fig. 2.6], only the aluminum shell in water is stably pulled by the axisymmetric beam because the parameters lie in the stable pulling region in Fig. 2.5(b) with the effective mass density ratio $\lambda_{\text{eff}} = 0.31$ and the effective bulk modulus ratio $\kappa_{\text{eff}} = 1.44$ [see Eq. (2.11)]. For this case, the minimum β required for the trapping is about 65° and required for pulling is about 56°.

In the practical situation though, one would need to include the correction by thermoviscous absorption. The absorption degrades the negative force,[14,43] and consequently increases the minimum β required, as illustrated in Fig. 2.7 for the simultaneous pulling and trapping of the aluminum shell in water in the parameter space ka and a. The correction to the axial force is dominated by the term,[14] $Y_z^{\text{abs}} = Q_{\text{abs}}\cos\beta$, where $\cos\beta$ accounts for projection of momentum to the propagation

axis and Q_{abs} is the absorption efficiency. For the range of ka examined herein, it is satisfactory to approximate the force experienced by the elastic shell by retaining only the monopole and dipole terms.[143] The range of the ratio of the boundary thickness to the sphere radius, δ/a, in Fig. 2.7 is from 0.0002 to 0.05, where the ratio,

$$\delta/a = \sqrt{2\nu/\omega}/a = (2\nu/ca)^{1/2}/(ka)^{1/2}, \tag{2.13}$$

is a function of a and ka[43] (ν denotes the kinematic viscosity of the surrounding fluid). Following from the $\delta/a \ll 1$ approximation, the absorption efficiency[14,51] is,

$$Q_{\text{abs}} \approx 12(ka)^{1/2}(2\nu/ca)^{1/2}[(\lambda-1)/(1+2\lambda)]^2\cos^2\beta, \tag{2.14}$$

which accounts for the viscous power dissipation near the small solid sphere; the loss contribution to the monopole term is neglected (which is satisfactory unless Q_{abs} in Eq. (2.14) is significantly reduced when β is near 90°). With these approximations, Fig. 2.7 demonstrates the existence of a stable tractor beam (i.e., simultaneous pulling and trapping) for a small particle when loss correction is included. These angles are relatively large, making "long-range" difficult.

The results in the standing-wave limit ($\beta = 90°$) are applicable to trapping by two orthogonal standing waves,[144] where the field near the nodes and anti-nodes are approximated by the $l = 0$ and $l = 1$ Bessel-function fields.[63] The trapping criteria are

$$\begin{aligned} &f_1/f_2 > -3/2 \text{ for trapping at pressure nodes;} \\ &f_1/f_2 < -3/4 \text{ for trapping at pressure anti-nodes.} \end{aligned} \tag{2.15}$$

Particles whose parameters are in the regime between these two transitions are trapped by both the nodes and anti-nodes.

On the other hand, trapping conditions for a Rayleigh particle can be simplified by using higher-order beams. For instance, the trapping by $l = 2$ beam has an acoustic contrast factor

[Eq. (2.9)]:

$$\Phi_2(\beta) = 1/8 \sin^2 \beta f_2, \tag{2.16}$$

which depends on the mass density ratio but not the bulk modulus radio, where dense (light) particles are repulsed (attracted) and there is no reversal of the trapping when varying the paraxial parameter β in this case. Further, the non-conservative radiation force along the axis direction exerted by the $l = 2$ beam on the Rayleigh particle is negligible, which in turn gives more flexibility in manipulating the axial force for particles beyond the Rayleigh regime.

CHAPTER 3

BORN APPROXIMATION METHOD FOR TRAPPING FORCE

In the previous chapter, the transverse trapping force has been analyzed based on the Gorkov potential and the partial wave expansion with a focus on small spherical objects within the Rayleigh regime ($ka << 1$ with k being the wavenumber and a being the characteristic length of the particle). However, for large objects beyond the Rayleigh regime, there is a lack of analytical solutions for the analysis and prediction of the transverse radiation force. The radiation forces are usually computed using the partial-wave expansion method or the finite element method,[145] which are not efficient and the underlying physics of the radiation force is not intuitive and straight-forward. In this chapter, a relatively simple method, i.e., the Born approximation method, will be introduced, examined, and utilized for the analysis of acoustic transverse trapping force generated by acoustic Bessel fields with a focus on large spherical objects and objects of different shapes.

Systematic analysis of acoustic trapping forces generated by acoustic Bessel fields on small spherical objects has been studied in the Chapter 2. In the current chapter, the focus is to examine the capability of the Born approximation method for the analysis of gradient trapping forces, and then use it to analyze the trapping force exerted by acoustic Bessel fields on large spherical objects and objects of different shapes and orientations. In this chapter, it is proved that for multidimensional fields, for example, acoustic Bessel fields here, the Born approximation method can provide a good approximation in the direction where the gradient force dominates. The Born approximation method can simplify the analysis of the trapping force, and can also provide insight into the trapping behaviors.

Recall that the pressure field $\mathrm{Re}[p(\mathbf{r}, t)]$ (Re denotes real part) of the incident Bessel Beam is given by

$$p = p_0 J_l(\mu\rho) \exp(i\kappa z + il\phi - i\omega t), \tag{3.1}$$

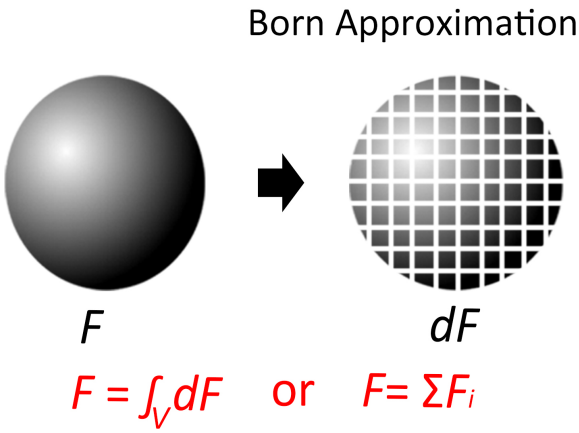

Figure 3.1: Illustration of the Born approximation method. The total radiation force F can be obtained by taking an integration (or a summation numerically) of the force over the total volume V occupied by the object. Numerical grids are divided evenly in all three directions in the Cartesian coordinates.

where p_0 is a real-valued amplitude, J_l is Bessel function with topological charge of l, $\mathbf{r}(\rho, \phi, z)$ is the field point in cylindrical coordinates, and the transverse wavenumber μ and axial wavenumber κ are related to the total wavenumber $k = \sqrt{\mu^2 + \kappa^2} = \omega/c_0$ (c_0 is sound speed in the surrounding media) through a paraxiality parameter β with $\mu = k \sin\beta$, and $\kappa = k \cos\beta$.

When the topological charge $l = 0$, the Bessel beam is an ordinary axisymmetric beam with a central pressure maximum, however, when $l \neq 0$, the Bessel beams are vortex beams with a central pressure null. One advantage of Bessel beams is that the axial and transverse components are explicitly separable. In particular, acoustic Bessel beams have a traveling wave component in the axial direction, yet have a standing wave component in the transverse direction. Hence, the Born approximation method should be applicable to the calculation of the transverse radiation force [Fig. 3.1].

3.1 Acoustic trapping force based on the Gorkov potential

When objects are small, the transverse radiation force F_ρ can be obtained from the negative gradient of the Gorkov potential along the transverse direction in the cylindrical coordinates, i.e.,

$$F_\rho = -\nabla_\rho U \tag{3.2}$$

with the Gorkov potential being

$$U = (\pi a^3/3)[f_1 p^2/(\rho_0 c_0^2) - (3/2) f_2 \rho_0 \mathbf{v}^2], \tag{3.3}$$

where the potential U is proportional to the volume of the sphere (i.e., $V = 4\pi a^3/3$ and a is the radius of the object). ρ_0 is the mass density of the background medium, and f_1 and f_2 are the monopole and dipole factors,

$$f_1 = 1 - K_0/K_s, \; f_2 = 2(\rho_s - \rho_0)/(2\rho_s + \rho_0), \tag{3.4}$$

depending on the mass density (ρ) and bulk modulus (K) of the object (indicated by the subscript s) and the surrounding medium (indicated by the subscript 0).[19]

Combining Eqs. (3.1)-(3.3), the transverse radiation force F_ρ acting on a small particle at the transverse location R is

$$F_\rho = \frac{4\pi a^3}{3} f, \tag{3.5}$$

with the force density f being,

$$f = \frac{p_0^2 \mu}{4\rho_0 c_0^2} \left\{ J_l (J_{l+1} - J_{l-1}) f_1 - \left[J_l (J_{l+1} - J_{l-1}) P_2(\cos\beta) + (J_{l+1} J_{l+2} - J_{l-1} J_{l-2}) \frac{\sin^2\beta}{2} \right] \frac{3}{2} f_2 \right\}, \tag{3.6}$$

where $J_l \equiv J_l(\mu R)$ is defined for convenience and simplicity.

When the particle is near the beam axis, Eq. (3.5) can be further simplified as:

$$F_\rho^{\text{Gorkov}} = \frac{p_0^2 \mu}{2\rho_0 c_0^2} \cdot V \cdot \mu R \cdot \Phi_l(\beta) \tag{3.7}$$

with the acoustic contrast factors $\Phi_l(\beta)$,

$$\Phi_l(\beta) = \begin{cases} [f_1 - \frac{3}{4}(3\cos^2\beta - 1)f_2]/3 & l = 0 \\ -[f_1 + (3\sin^2\beta - \frac{3}{2})f_2]/6 & l = 1 \\ f_2 \sin^2\beta(\mu R)^{2(l-2)}/[(l-1)!(l-2)!2^{2l-5}] & l \geq 2. \end{cases} \tag{3.8}$$

Recall that the acoustic contrast factors for $l = 0, 1, 2$ was previously given in Fan and Zhang.[19] In addition, the trapping forces for $l \geq 2$ have identical dependence on the dipole factor f_2, but the trapping force actually decreases as the order of vortex beams increases.

It is also useful and significant to discuss a special case of cylindrical standing waves, i.e., $\beta = 90°$, since the standing waves are easier to use for particle manipulations in practical applications. In this case, the acoustic contrast factors Φ_l for a cylindrical standing waves are simplified as,

$$\Phi_l = \begin{cases} (f_1 + \frac{3}{4}f_2)/3 \text{ or } (\Delta_K + \frac{1}{2}\Delta_\rho)/3 & l = 0 \\ -(f_1 + \frac{3}{2}f_2)/6 \text{ or } -(\Delta_K + \Delta_\rho)/6 & l = 1 \\ f_2(\mu R)^{2(l-2)}/[(l-1)!(l-2)!2^{2l-5}] \text{ or } \frac{2}{3}\Delta_\rho(\mu R)^{2(l-2)}/[(l-1)!(l-2)!2^{2l-5}] & l \geq 2, \end{cases} \tag{3.9}$$

where the expressions in terms of the mass density contrast $\Delta_\rho = (\rho_s - \rho_0)/\rho_0$ and bulk modulus contrast $\Delta_K = (K_s - K_0)/K_0$ are more intuitive for the justification of trapping behaviours. As discussed in the previous chapter, this acoustic contrast factor Φ_l can be directly used for the predictions of the trapping behaviors for small objects near the beam center [Fig. 3.2]. For the negative contrast factors, the particle will be trapped due to the restoring force, and the particle will be repelled from the axis if the contrast factor is positive.

3.2 Acoustic trapping force based on the partial wave expansion method

For small objects, one can use the Gorkov potential to compute the acoustic trapping force, and use the acoustic contrast factors to predict the trapping behaviors. However, for large objects,

the Gorkov potential loses its capability for the predictions of the radiation force. In this case, the partial wave expansion method[50] is usually used for the calculation of acoustic trapping forces,

$$
\begin{aligned}
&Y_\rho(R) = F_\rho(R)/F_0 = \sum_{m=-\infty}^{\infty} K_m^+ B_m, \\
&K_m^+ = J_{l-m}(\mu R)J_{l-m-1}(\mu R) - J_{l+m}(\mu R)J_{l+m+1}(\mu R), \\
&B_m = \frac{1}{(ka)^2}\sum_{n=|m|}^{\infty}\frac{(n-m)!}{(n+m)!}P_n^m(\cos\beta)P_{n+1}^{m+1}(\cos\beta)\mathrm{Im}(s_n^\star s_{n+1}),
\end{aligned}
\tag{3.10}
$$

where $F_0 = \pi a^2 p_0^2/(2\rho_0 c_0^2)$, Im represents for imaginary part, P_n^m are the associated Legendre polynomials, and the scattering functions s_n[42] are determined by boundary conditions on the particle surface (see Appendix).

The partial wave expansion method is powerful, yet it is relatively time-consuming, and the physics behind the trapping force is not clear enough. That is why the Born approximation method is introduced here for the analysis of the acoustic trapping force, especially for large objects.

3.3 Acoustic trapping force based on the Born approximation method

The trapping force from the Born approximation method takes an integration of the infinitesimal force over the total volume occupied by the objects. Based on Eq. (3.5), the infinitesimal force dF_ρ acting on a volume element dV can be obtained by replacing the volume $4\pi a^3/3$ by dV and corresponding F_ρ by dF_ρ:

$$
dF_\rho = f\,dV. \tag{3.11}
$$

Mathematically, the reason why the Born approximation is restricted to standing waves in the transverse direction is that the gradient force dF_ρ is proportional to dV, however, the scattering force dF_z for a traveling wave along the axial direction is proportional to $(dV)^2$, prohibiting the integration over a volume of finite size.[26]

Consequently, the net transverse acoustic radiation force on an object of *arbitrary-shape* can be then calculated by taking the integration of the force over the total volume occupied by the

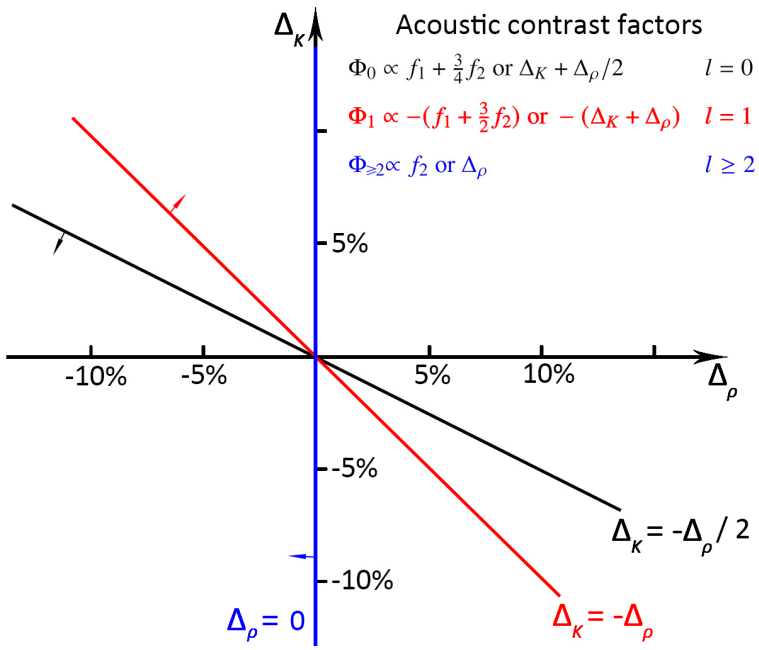

Figure 3.2: Acoustic contrast factors for cylindrical standing waves. Each straight line (black: $l = 0$; red: $l = 1$; and blue: $l \geq 2$) divides the parameter space into two regions, and the region for trapping is marked by the corresponding arrow. $\Delta_\rho = (\rho_s - \rho_0)/\rho_0$ and $\Delta_K = (K_s - K_0)/K_0$ are the mass density contrast and the bulk modulus contrast, respectively.

object (V),

$$F_\rho^{\text{Arbitrary object}} = \int_V dF_\rho. \tag{3.12}$$

Since the Born approximation method in Eq. (3.12) only requires the integration over the object volume, it will simplify the computation compared with some previous methods, for example, the partial wave expansion method, where the scattering coefficients up to a certain order need to be considered.

The Born approximation is an approximation approach, and it is valid only under certain conditions. Hence, it is essential to first examine the validity and accuracy of the Born approximation method for the analysis of acoustic trapping forces. The results from the Born approximation will be compared with the exact solution for spherical objects from the partial wave expansion in Eq. (3.10) as well as the Gorkov potential in Eq. (3.5).

One important issue for the numerical calculation is the relationship of the mesh grid and the convergence. Here, the numerical grids are divided evenly in all three directions in Cartesian

coordinates with the spacing of $a/40$ for spheres and $a/80$ for the cylinders. A convergence test has been conducted, where the maximum error is $\sim 0.3\%$ when the spacing length is halved or doubled for the former case, and for the latter case, the error is $\sim 3\%$ when the mesh grid size is doubled and $\sim 2\%$ as the grid size is halved.

3.4 Trapping by Cylindrical Standing Waves

Let us first examine the Born approximation for objects with relatively large material contrasts. Here, the transverse radiation forces generated by the ordinary standing Bessel field on an aluminum sphere in water are calculated as an example (Fig. 3.3). For this case, the Born approximation method (red circles) fails to predict the radiation force (black solid lines: exact solution) after the first peak of the force. This is understandable because the Born approximation method assumes the amplitude of the scattered acoustic field is considerably small compared with incident acoustic field, which is true when the acoustic properties of the objects are similar to those of the surrounding medium. However, for the case of an aluminum sphere in water, the amplitude of the scattered field is already comparable with the incident field, which will definitely cause some errors. Negative radiation force can trap particles to the beam axis, yet positive force will repel the particles away. Hence, although large errors occur for the Born approximation method when the material contrast is large, the Born approximation method can still make correct predictions on the trapping behaviors (trapping or repelling) up to a relatively large ka even beyond the Rayleigh regime ($ka << 1$). The Gorkov potential, on the other hand, can only make predictions within the Rayleigh regime (blue stars), where the force is proportional to $(ka)^3$.

Hence, in order to make sure the Born approximation method is accurate, the material contrast of the objects cannot be large. To examine the performance and accuracy of the Born approximation on objects of small material contrast, the radiation forces on spherical objects with mass density contrast $\Delta_\rho = 5\%$ and bulk modulus contrasts $\Delta_K = 15\%$ are computed for the zero order, the first order and the second order standing Bessel fields [Fig. 3.4]. The parameters chosen here are the same as that in Jerome et al.[26] since in the case of common soft biological materials

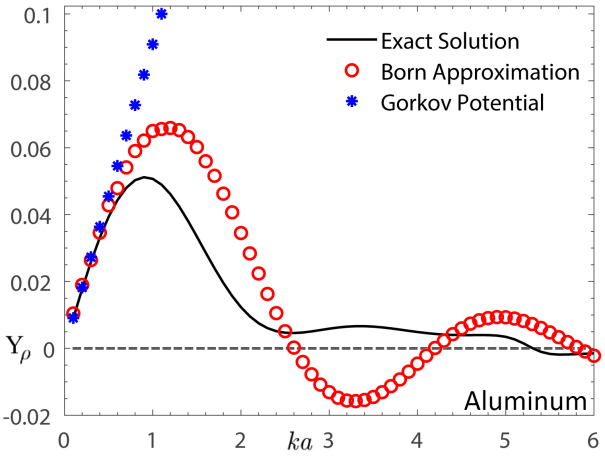

Figure 3.3: Examination of the Born approximation on spheres with large material contrast. Dimensionless trapping force $Y_\rho = F_\rho/(\pi a^2 p_0^2/2\rho_0 c_0^2)$ generated by the ordinary cylindrical standing waves on an aluminum sphere in water are examined with $\Delta_\rho = 170\%$ and $\Delta_K = 3367\%$. The spheres are located at $\mu R = 0.1$. Black solid line: exact solution in Eq. (3.10); red circles: Born approximation method in Eq. (3.12); and blue stars: Gorkov potential in Eq. (3.5).

with water taken as the surrounding fluid, the bulk modulus contrast is typically two or three times that of the mass density contrast, which is usually around 5%.[27] For this case, the results from the Born approximation method (red circles) and the partial wave expansion method (black solid lines) agree quite well with each other (middle panels). The errors take the absolute value of the difference between the Born approximation and the exact solution. To further examine the performance and accuracy of the Born approximation method, the results obtained here using two-dimensional cylindrical standing waves (Fig. 3.4) are compared with the results using one-dimensional standing waves (Fig.1 in Jerome et al.[26]). The accuracy of the Born approximation in 2D standing waves are slightly better than that in 1D standing waves when comparing the two results.

From the results in Fig. 3.4, one finds that small objects (small ka) can be trapped to the field center (pressure node) by the first-order vortex field (negative force), yet these objects will be repelled away from the center for the zero order and the second order Bessel fields, even though for the second-order vortex field, there is a pressure node at the field center. These results are predicted and understood in our prior paper[19] by the Gorkov potential and the acoustic contrast factors in Eq. (3.12). As the particle becomes larger, the Gorkov potential loses its prediction capability, for example, the Gorkov potential mistakenly predicts that the particle is repelled from

the center of the ordinary cylindrical standing wave no matter the size of the object [see the middle panel in Fig. 3.4(a)]. However, the Born approximation can instead make correct predictions on the radiation force for even large particles far beyond the Rayleigh regime. Here, the trapping regions are $\sim 2.8 < ka <\sim 4$ for the zero order Bessel field; $ka <\sim 2.2$ for the first order Bessel field; and $\sim 1.2 < ka <\sim 3.5$ for the second order Bessel field.

In order to understand the underlying physics of the Born approximation on the predictions of the radiation force especially for large objects, the Gorkov potential and its negative gradient are computed with respect to the transverse location (see the bottom panels in Fig. 3.4). Comparing the radiation forces in the middle panels with the negative gradient of the Gorkov potential (red dashed lines) in the bottom panels, one finds that these two quantities follow almost the same pattern. It is understandable because based on the Born approximation, the net total force comes from the accumulation of the individual forces from all the volume elements, and each individual force (could be positive or negative) is computed from the Gorkov potential. Note that if the particle is located exactly at the center, the net transverse radiation force is equal to zero since the force acing on a half of the object is cancelled with the other half of the object due to the geometrical symmetry. Here, the force is computed at $\mu R = 0.1$, slightly away from the center, hence, in this case, the force acting on most of the object can still cancel, and the dominant contribution to the net force only comes from a thin outer layer of the object, where the geometry is asymmetric with respect to the field center. Hence, this thin outer layer can still be considered as a small object, and the force acting on the outer layer, i.e., the net force acting on the whole object, will be directly related to the gradient of the Gorkov potential, i.e.,

$$\mathbf{F}(\text{large } ka) \sim -\nabla U(r = a). \tag{3.13}$$

If all the volume elements suffer from positive forces, then the total force is no doubt positive, and if the negative radiation force is desired, then at least some portion of the object must be subject to a negative force. The finding here provides an efficient way to predict or at least give a sense of the

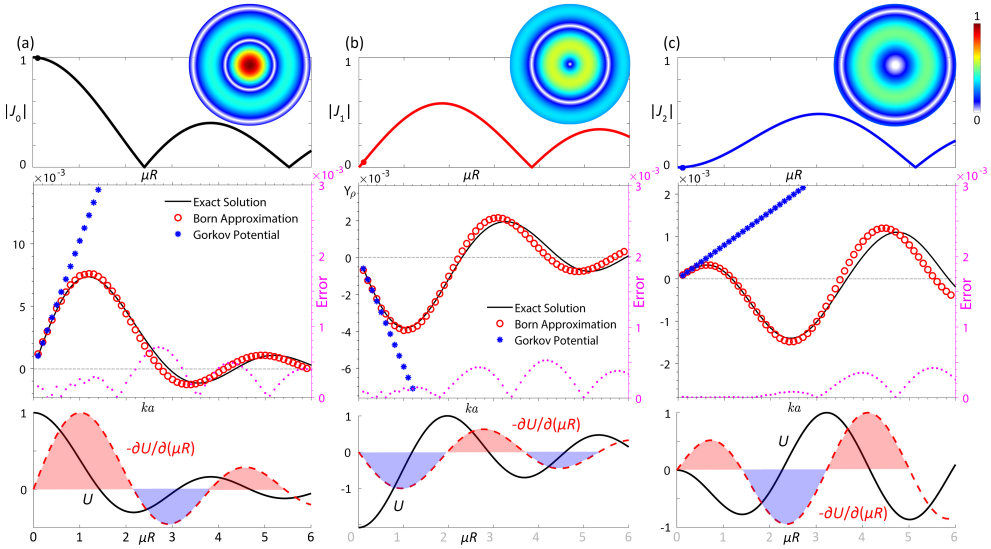

Figure 3.4: Examination of the Born approximation on spheres with small material contrast for (a) zero-order (b) first-order and (c) second-order cylindrical standing waves. Top panels: pressure profiles and corresponding cylindrical standing Bessel fields; Middle panels: dimensionless trapping force Y_ρ on spheres with $\Delta_\rho = 5\%$ and $\Delta_K = 15\%$; The spheres are located at $\mu R = 0.1$ corresponding to the points in the top panels. Black solid lines: exact solution in Eq. (3.10); red circles: Born approximation method in Eq. (3.12); and blue stars: Gorkov potential in Eq. (3.5). Pink dots: the errors are the absolute values of the force differences between the Born approximation and the exact solution. Bottom panels: Gorkov potential and the negative gradient of the potential.

radiation force and trapping behaviors based on the Gorkov potential, and the Gorkov potential is useful for small objects and even for large objects far beyond the Rayleigh regime.

The Born approximation method can also be utilized to analyze the trapping behaviors of objects with different shapes and orientations. Here, the gradient radiation force generated by ordinary standing Bessel fields on cylindrical objects with different height-to-diameter ratios (i.e., $h : D = 3 : 16$ and $h : D = 1 : 1$) are examined and compared with the exact solution of spheres with the same volumes. The cylinder tends to be a disk when the height-to-diameter ratio h/D is small, and it becomes close to a sphere as the ratio is close to 1. Figure 3.5(a) shows the computed dimensionless trapping force Y_ρ for the first cylinder ($h : D = 3 : 16$). When the object is small ($ka <\sim 0.6$), the radiation force is independent of the object shape and orientations, and the force is linearly proportional to the object volume as predicted by the Born approximation [Eq. (3.12)] and the Gorkov potential as well [Eq. (3.5)]. As the object goes beyond the linear regime, the

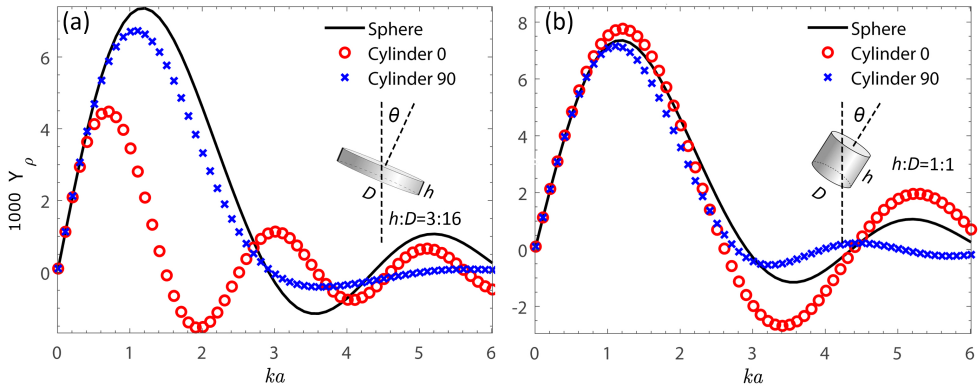

Figure 3.5: Examination of the Born approximation on objects of different shapes and orientations for zero-order standing waves. Dimensionless trapping forces Y_ρ on the cylinders ($\Delta_\rho = 5\%$ and $\Delta_K = 15\%$) located at $\mu R = 0.1$ are computed from the Born approximation method (red circles: $\theta = 0°$; blue crosses: $\theta = 90°$), and the results are compared with a sphere of same volume from the exact solution (black solid line). The aspect ratios of the cylinders are (a) $h : D = 3 : 16$ and (b) $h : D = 1 : 1$. Black solid lines: exact solution in Eq. (3.10); red circles and blue crosses: Born approximation method in Eq. (3.12).

effect caused by the shape and orientation cannot be ignored, and the radiation force for objects of different shapes and orientations diverge. However, for the cylinder with aspect ratio $h : D = 1 : 1$ [Fig. 3.5(b)], the effect cause by the shape and orientation are weak compared with the case in (a), and the forces for different shapes and orientations start to diverge at a much larger ka ($ka \sim 3$). The reason is that for this case, the cylinder is close to a sphere, and thus the effect due to different geometry shapes and orientations can be ignored within a quite large range of ka under a certain value. The results here, on the other hand, also prove that the Born approximation method is valid and reliable.

3.5 Trapping by Traveling Waves

When considering the trapping by traveling waves instead of standing waves (the paraxiality parameter β is changed from 90° to be less than 90°), there appears an additional traveling component which will affect the transverse trapping behaviors.[19] In order to examine the error when changing the paraxiality parameter β from 90° to near 0°, the radiation forces acting on a spherical object with the material contrast of $\Delta_\rho = 5\%$, and $\Delta_K = 15\%$ are calculated for the zero-order, first-order and second-order Bessel fields [Fig. 3.6]. The results from the Born approximation

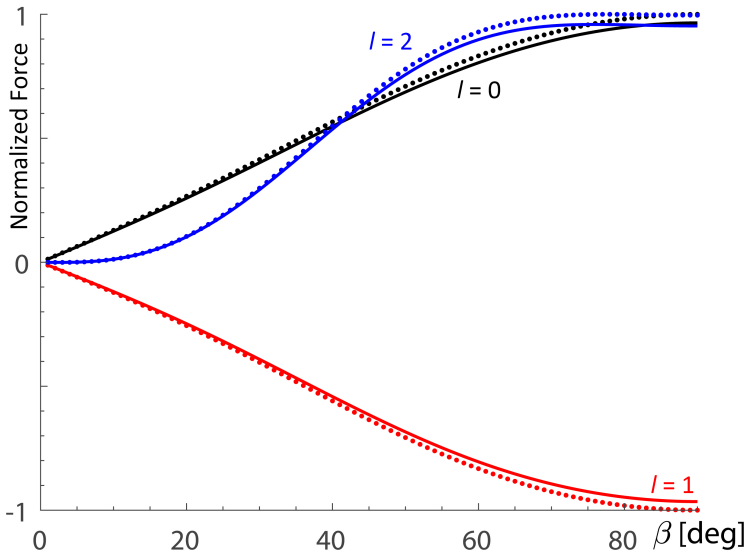

Figure 3.6: Examination of errors when varying the paraxiality parameter β for zero-order (black), first-order (red) and second-order (blue) Bessel fields. Errors can be obtained by comparing the normalized radiation force from the Born approximation (dotted lines) with the exact solution (solid lines). The parameters of the example here are $\Delta_\rho = 5\%$ and $\Delta_K = 15\%$. The maximum error is two order smaller than the exact solution.

[dotted lines, Eq. (3.12)] agree quite well with the exact solution [solid lines, Eq. (3.10)], with the maximum error two orders smaller than the exact solution. In addition, one finds that the magnitude of the radiation force decreases as β is reduced from 90° to 0. This is understandable because the standing wave component is proportional to $\sin\beta$, hence, the magnitude of the radiation force reaches a maximum at $\beta = 90°$ when the field is a pure standing field, and the force goes to 0 at $\beta = 0$ when the field has no standing wave component.

To further examine the effects caused by the paraxiality parameter β, the radiation force generated by traveling Bessel beams of the first three orders are calculated [Fig. 3.7]. When the particle is small, the trapping behavior is exactly same as the prediction from the Gorkov potential and the parameter-dependent contrast factor [Eq. (3.8)]. Note that for small objects, the Gorkov potential can be directly computed based on the object center. However, for large objects beyond the small ka range, direct use of the Gorkov potential based on object center will cause errors as discussed above. For this case, we can take the characteristic length of the object (for example the radius of a sphere) in place of the object center to predict the trapping behaviours using the

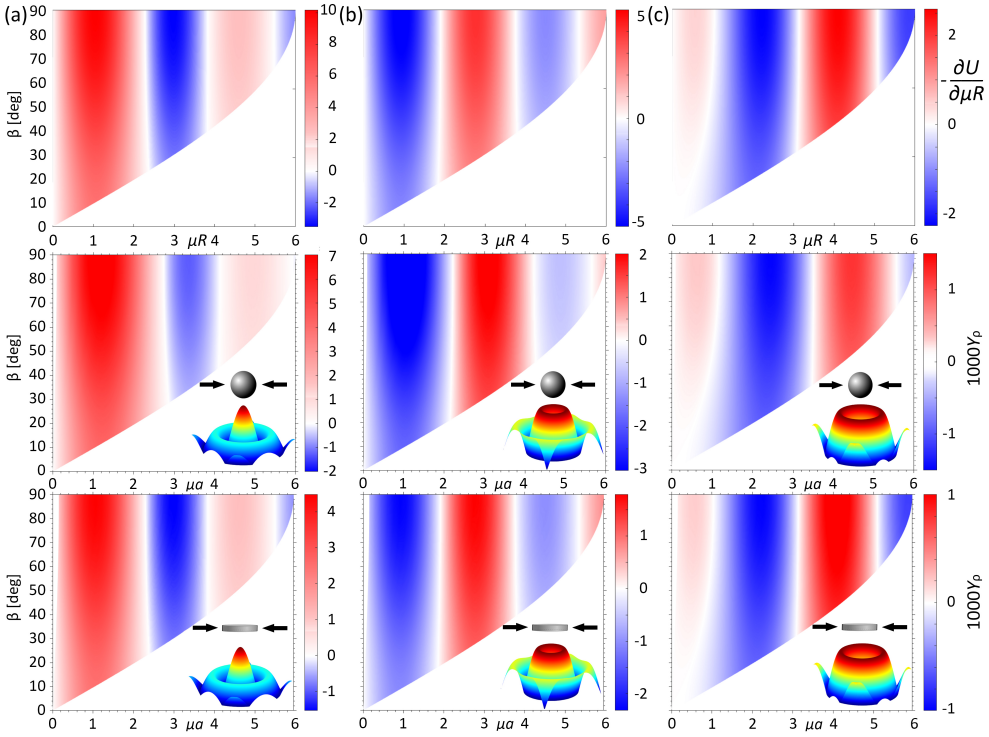

Figure 3.7: Examination the effect caused by the paraxiality parameter β for (a) zero-order (b) first-order and (c) second-order Bessel fields. Top panels: negative gradient of the Gorkov potential. Middle panels: dimensionless trapping force $Y_\rho(\mu R = 0.1)$ on a sphere with $\Delta_\rho = 5\%$, $\Delta_K = 15\%$ computed from the Born approximation method. Insets: traveling Bessel fields acting on a spherical object. Bottom panels: same as middle panels but for a cylinder with $h : D = 3 : 16$ [same as that in Fig. 3.5(a)]; a is the radius of the sphere or the cylinder and $D = 2a$.

Gorkov potential. Similar to the standing waves, the method proposed here can be also used for traveling beams, for example, see the top and middle panels in Fig. 3.7. From the results, the transverse radiation forces computed from the Born approximation (middle panels) have similar patterns compared with the negative gradient of the Gorkov potential (top panels) but with a slight shift as the particle becomes larger. The slight shift is understandable because the asymmetric part of the object, which contributes to the net radiation force, is not concentrated. Hence, it can be anticipated that the shift (or the error) will decrease when the asymmetric part becomes more concentrated for objects of other geometries. For example, see the bottom panels in Fig. 3.7 for a cylinder with the aspect ratio $h : D = 3 : 16$. As predicted, the patterns of the negative gradient of the Gorkov potential are almost the same as the transverse radiation force for this cylinder because for this case the outer layer of the cylinder is more concentrated than that of a sphere. Note that $\mu a = ka \sin\beta$ is used here to indicate the object size, hence, the truly available range $ka = \mu a/\sin\beta$ for trapping actually increases as the paraxiality parameter β decreases. Specifically, $\mu a = ka$ for cylindrical standing waves ($\beta = 90^\circ$). Since the Born approximation method performs better for small material contrast, the results from the Born approximation method will be more accurate when the material contrast is smaller than the situation considered here.

3.6 Remarks

In this Chapter, the Born approximation method was extended from one-dimensional standing fields to multidimensional fields, in particular, 2D standing Bessel fields and 3D traveling Bessel beams. The method was applied to analyze the transverse trapping force generated by acoustic ordinary Bessel beams and vortex beams, which provide a standing wave component along the transverse direction perpendicular to the propagating direction. The results from Born approximation method were compared with the exact solution from the partial wave expansion method to check the validity and accuracy of the Born approximation. For common soft biological materials with water taken as the surrounding fluid, it is relatively safe to use Born approximation method to make prediction for the objects whose characteristic length is smaller than a wavelength. In

addition, the effects caused by the beam parameter β, the object shape and orientation have also been investigated.

When the material contrast is not large, one can also use the Gorkov potential to predict the trapping behaviors or at least get a sense of feeling about the trapping behaviors for large objects. Note that, the characteristic length of the object (e.g. the radius of a spherical object) is instead used in the Gorkov potential to replace the location for the calculation. For example, the acoustic trapping force for a large spherical object can be estimated,

$$\mathbf{F}(\text{large } ka) \sim -\nabla U(r = a). \tag{3.14}$$

This finding here extends the application scope of the Gorkov potential to large objects far beyond the small ka range, which is also helpful for the analysis of acoustic trapping forces by plane waves.

Although only the Bessel fields are discussed in this chapter, the Born approximation method can be extended to an arbitrary incident field once the two required conditions are satisfied: (i) the mass density and compressibility of the particles and the background medium are similar; and (ii) the incident waves are standing waves or have a standing wave component. Then the gradient radiation force from an arbitrary field can be computed by integrating over the object volume with the infinitesimal force obtained by combining the gradient of the Gorkov potential and the specific incident wave field. The approximation methods discussed here will simplify the design of acoustic tweezers in the future and will have applications in biology and engineering, where object manipulation is required. While not considered here, the Born approximation allows for spatial variations of material parameters within the object, and could also be used for the analysis of acoustic radiation torque.[26]

CHAPTER 4

PHASE SHIFT APPROACH FOR PULLING FORCE

Inspired by the pioneering idea from Marston and Zhang,[42,43] a systematic approach based on phase shifts from scattering is developed to engineer a desired acoustic pulling force exerted by acoustic Bessel beams. The desired phase shifts, contributing to the desired radiation force, are herein fulfilled by adjusting the inner-to-outer radius ratio of a spherical shell. The example presented here is relatively simple yet reveals the powerful advantages of the phase shift approach. The phase shift approach developed here can be easily applied to any sound fields.

4.1 Phase shift for Acoustic Pulling Forces

The example of the present chapter is on axisymmetric fields in the form of zeroth-order Bessel function $J_0(\cdot)$, which is a solution of wave equation in acoustics (i.e. acoustic pressure)

$$p = p_0 J_0(\mu\rho)\exp(i\kappa z - i\omega t), \tag{4.1}$$

where ρ, z are radial and axial cylindrical coordinates, and transverse wavenumber $\mu = k\sin\beta$ and axial wavenumber $\kappa = k\cos\beta$ are related to total wavenumber $k = \omega/c_0$ through a paraxiality parameter β [see Fig. 4.1].

The far-field scattered pressure at radius r is conveniently expressed using a dimensionless complex form function f, i.e., $p_s = p_0(a/2r)e^{ikr}f$. With the aid of phase shifts, the dimensionless complex form function f is expressed as,[42]

$$f(\cos\theta) = (i/ka)\sum_{n=0}^{\infty}(2n+1)(1-e^{i2\delta_n})P_n(\cos\beta)P_n(\cos\theta), \tag{4.2}$$

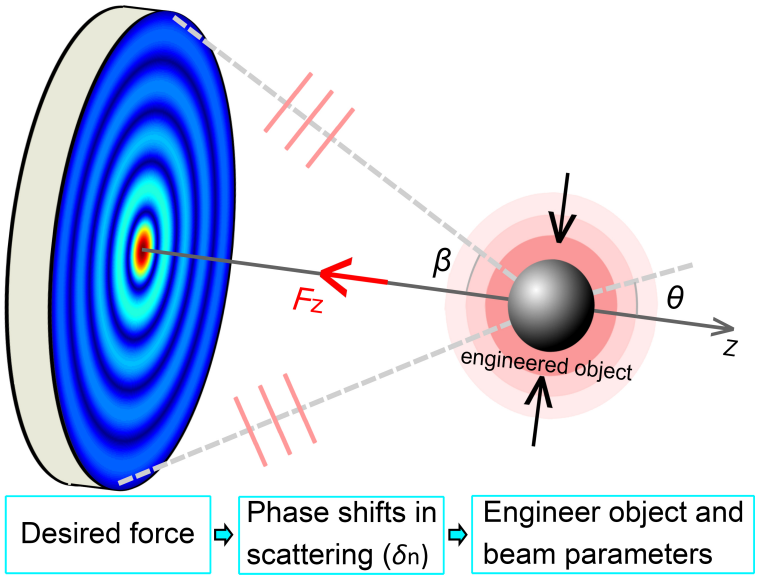

Figure 4.1: Illustration of incident Bessel beam scattered by an engineered object. β is the paraxial parameter and θ is the scattering angle. Phase shift approach: the desired phase shifts, which contribute to the desired radiation force, are adjusted by engineering parameters of objects and beams.

which characterizes the dependence of the scattering on the phase shifts. These phase shifts, determined from boundary conditions, rely on the object dimension ka and acoustic properties of the objects and the surrounding medium (or rely on the energy of incident particles and the potential energy of the scattering objects in quantum[146]). The range of phase shifts is $\delta_n \in [-\pi/2, \pi/2]$, and $\delta_n = 0$ at $ka = 0$ due to the absence of scattering. Eq. (4.2) together with Eq. (4.3) will be used to show the connection between the scattering and the radiation force.

When the energy dissipation is negligible (nondissipative scattering), the dimensionless axial radiation force is simply written as a summation of functions of adjacent partial wave phase shifts δ_n, which play significant roles in the scattering by affecting the coupling of different multipoles from multipole expansion[42]

$$Y_z = \frac{4}{(ka)^2}\sum_{n=0}^{\infty}(n+1)\underbrace{\sin^2(\delta_n - \delta_{n+1})}_{\text{non-negative}}\underbrace{P_n(\cos\beta)P_{n+1}(\cos\beta)}_{\text{may be positive or negative}}. \tag{4.3}$$

This formula was also recovered in the matter-wave tractor beams in Gorlach et al.[146] Here, the

phase shifts δ_n are real-valued and associated with scattering functions s_n by $s_n = \exp(i2\delta_n)$ ($\gamma_n = 0$); see Appendix in Fan and Zhang [19] for the expressions of s_n for different objects.

Based on the phase-shift formula in Eq. (4.3), an approach can now be established to analyze and engineer the acoustic radiation force, specifically the acoustic pulling force. Since the term involving the phase shifts, $\sin^2(\delta_n - \delta_{n+1})$, can never be negative, the pulling force must originate from negative Legendre polynomials, which are functions of the paraxial parameter β [see Fig. 4.2(a)]. Generally speaking, negative pulling forces are a result of a relatively large paraxial parameter β, for example, in the literature, $\beta \approx 45°$,[13,14,35] $\beta \approx 54°$,[46] $\beta \approx 56°$,[147] $\beta > 65°$,[37] yet a small β is actually desired in practical realization.

The objective here is to find a set of phase shifts that can allow the optimization of the angle β for a pulling force. It is desired to eliminate the first term which is never negative as the product P_0P_1 is never negative. The elimination is satisfied by $\delta_0 = \delta_1$. When only the terms δ_0 and δ_1 in Eq. (4.3) survive, the minimum angle for pulling force is $\beta \approx 54.7°$ [black solid line in Fig. 4.2(a)], which happens when the monopole and dipole are in phase (i.e. $\delta_0 = \delta_1$) and the angle obtained here agree with the previous predictions.[14,19,43] The minimum angle can be further reduced as more multipoles are in phase, for example, $\beta \approx 39°$ corresponding to the first three multipoles in phase (i.e. $\delta_0 = \delta_1 = \delta_2$, red dashed line) or $\beta \approx 31°$ corresponding to the first four multipoles in phase (i.e. $\delta_0 = \delta_1 = \delta_2 = \delta_3$, blue dashed-dot line).

When the particle is larger and larger (characterized by ka with a being the radius), there can be more and more multipoles in phase to enhance forward scattering [see Inset in Fig. 4.2(a)] and in turn provide objects stronger backward momentum or pulling force. In principle, the angle β can be reduced to a value that is experimentally realizable or even smaller as long as a sufficiently large number of phase shifts are the same [Fig. 4.2(b)]. Then the problem is how to design engineered objects with the right set of parameters to achieve the constraint of in-phase scattering, although finding an object to satisfy many phase shifts in phase is not straight-forward. It is also worth noting that the maximum values of negative force occur somewhere between the two solutions of $P_n(\cos\beta) = 0$. Once the β or rough range of β is determined, an estimation about the object

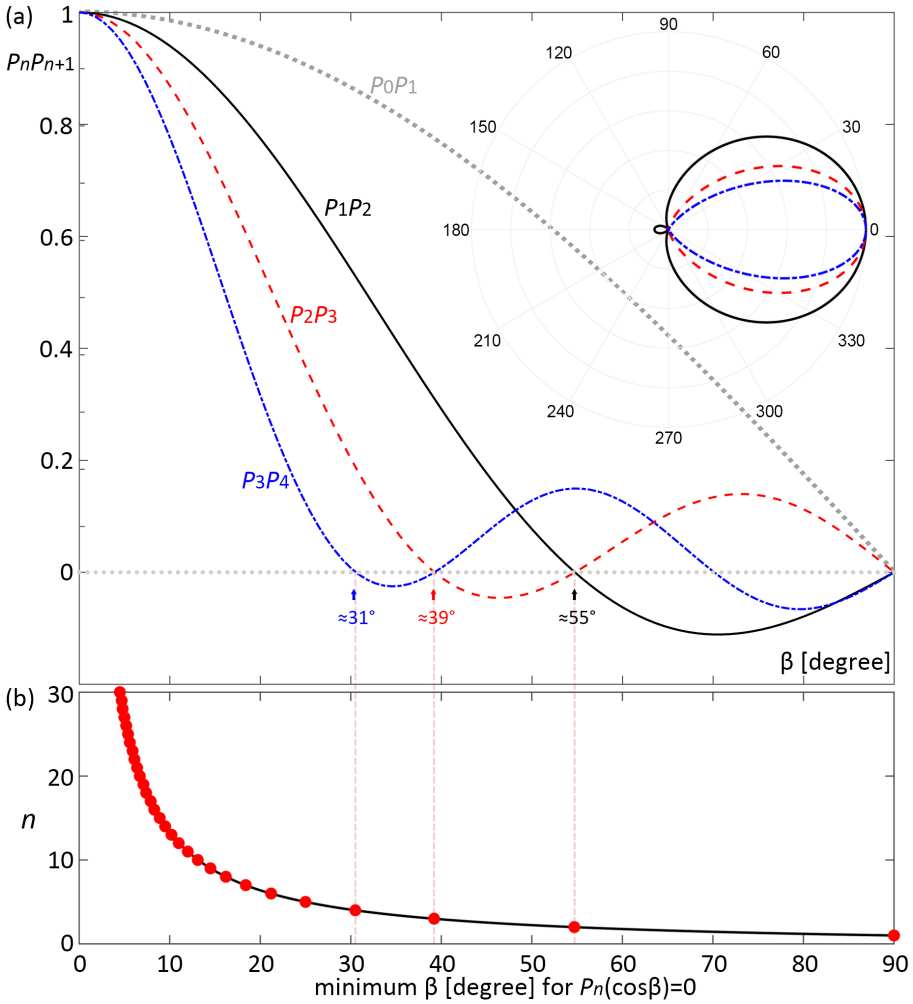

Figure 4.2: (a) Production of adjacent Legendre polynomials P_nP_{n+1} as a function of paraxial parameter β [see Eq. (4.3)]. Minimum β for negative production (P_nP_{n+1}) are marked corresponding to each term. Inset: Normalized scattering pattern $|f|^2$; see Eq. (4.2). The first production $P_0P_1 = \cos\beta$ cannot be negative; see gray dotted line. Black solid line: monopole and dipole in-phase scattering at 54.7°; Red dashed line: monopole, dipole, and quadrupole in-phase scattering at 39°; Blue dashed-dot line: monopole, dipole, quadrupole and octupole in-phase scattering at 31°. More multipoles in phase enhance forward scattering and in turn provide objects stronger backward momentum. These minimum angles correspond to the minimum solutions of β for $P_n(\cos\beta) = 0$ in (b), where minimum β decreases as the order of Legendre polynomials n increases, and the curve is a fit with $\beta = 138.4°/(n + 0.54)$.

dimension ka can be also obtained since β is related to the order n [$\beta = 138.4°/(n+0.54)$], whose truncation is somewhat in excess of ka.[13]

4.2 Rayleigh approximation

Let us start by considering a small particle ($ka \ll 1$) where the contributions only come from monopole and dipolar fields involving the phase shifts of δ_0 and δ_1 ($\delta_{0,1} \ll 1$). The expression of the complex function f in Eq. (4.2) is simplified,

$$f(\cos\theta) \propto \underbrace{\delta_0}_{\text{monopole}} + \underbrace{3\delta_1 \cos\beta \cos\theta}_{\text{dipole}}. \tag{4.4}$$

When $\delta_0/\delta_1 < 0$, backward scattering is stronger than forward scattering and the radiation force is always positive. However, when $\delta_0/\delta_1 > 0$, the forward scattering is stronger instead, and in this case, the radiation force is possibly negative, depending on $\cos\beta$. Two typical scattering patterns $|f|^2$ with parameters of $(\delta_0/\delta_1, \beta) = (\mp 1, 54.7°)$ are illustrated in Figs. 4.3(a) and (b).

In this case, the expression of the acoustic radiation force in Eq. (4.3) is simplified as

$$Y_z \propto t^2 - 2t + 3\cos^2\beta. \tag{4.5}$$

with the force determined by the phase shift ratio $t = \delta_0/\delta_1$.The range of phase shifts ratio δ_0/δ_1 for negative pulling force is in between $1 \pm \sqrt{1 - 3\cos^2\beta}$ [see Eq. (4.5) and Fig. 4.3(c)]. When the monopole and dipole are in phase (i.e. $t = \delta_0/\delta_1 = 1$), the minimum $\beta \approx 54.7°$ is achieved. The maximum range of phase shift ratio is $0 < \delta_0/\delta_1 < 2$ when β approaches to 90°. These results in terms of phase shifts do not rely on specific objects.

The goal is to find objects and beams parameters to fulfill the required phase shifts. In Rayleigh regime, only the first two terms of phase shifts need to be considered, i.e.,

$$\delta_0 = -(1/3)(ka)^3 f_1, \delta_1 = (1/6)(ka)^3 f_2, \tag{4.6}$$

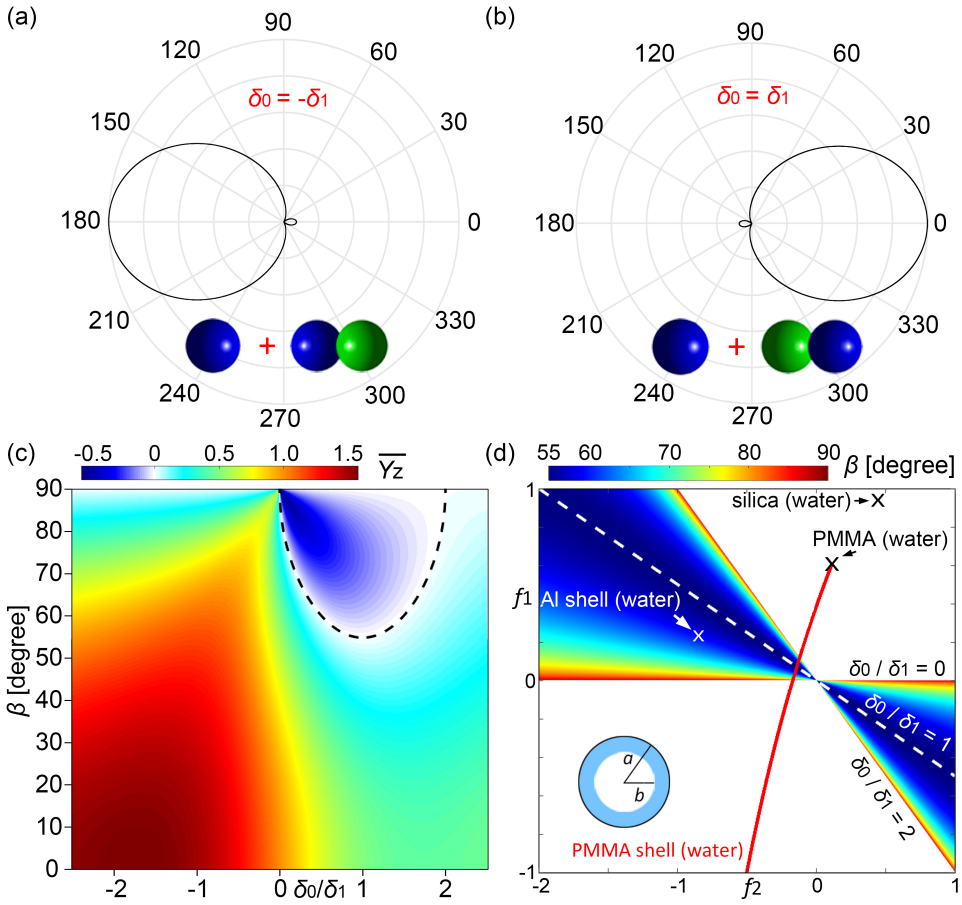

Figure 4.3: Rayleigh approximation. Scattering pattern $|f|^2$ [Eq. (4.4)] with parameters of (a) $(\delta_0/\delta_1, \beta) = (-1, 54.7°)$, where backward scattering is stronger than forward scattering, and (b) $(\delta_0/\delta_1, \beta) = (1, 54.7°)$, where forward scattering is stronger instead. Insets: illustrations of the coupling between a monopole and a dipole. (c) Scaled radiation force $\overline{Y_z}$ [Eq. (4.5)] in the parameter space of $(\delta_0/\delta_1, \beta)$. Black dashed line indicates the boundary $(\delta_0/\delta_1 = 1 \pm \sqrt{1 - 3\cos^2\beta})$ where radiation force is zero. (d) Diagram for pulling a Rayleigh particle in the parameter space of (f_2, f_1), with the colorbar illustrating the minimum angle required for axial pulling force. Minimum angle $(\beta \approx 54.7°)$ occurs on the white dashed line, which corresponds to the monopole and dipole in phase $(\delta_0 = \delta_1)$. Several examples are marked by crosses with the factors (f_2, f_1) being: (i) $(0.44, 0.94)$ for a silica sphere in water, giving $\delta_0/\delta_1 = -4.3$; (ii) $(0.11, 0.61)$ for a PMMA sphere in water, giving $\delta_0/\delta_1 = -11.1$; (iii) $(1, 1)$ for a rigid sphere, giving $\delta_0/\delta_1 = -2$; (iv) $(-0.85, 0.23)$ for an aluminum shell in water $(b/a = 0.96)$, giving $\delta_0/\delta_1 = 0.54$. Red solid line indicates the dynamic behaviours for PMMA shell when varying the inner-to-outer radius ratio from 0 to 0.99. Three intersection points with $\delta_0/\delta_1 = 0, 1, 2$ correspond to $b/a = 0.703, 0.684, 0.669$, respectively. The results are obtained by combining the expression of acoustic radiation force in Eq. (4.5) and the expression of phase shifts in Rayleigh regime in Eq. (4.6). Inset: illustration of a shell-like particle.

Materials	Mass density ρ [kg/m^3]	Longitude wave speed c_L [m/s]	Transverse wave speed c_T [m/s]
Air	1.21	343	
Hexane	656	1078	
Water	1000	1500	
PMMA	1190	2690	1340
Silica	2201	5928	3761
Al	2700	6420	3040

Table 4.1: Acoustic properties of materials. The effective density of an Aluminum (Al) shell of $b/a = 0.96$ is 311 kg/m^3 calculated from Eq. (4.9).

depending on the monopole and dipole factors,[12]

$$f_1 = 1 - 1/\kappa \text{ and } f_2 = 2(\lambda - 1)/(1 + 2\lambda), \tag{4.7}$$

with $\lambda = \rho/\rho_0$, $\kappa = K/K_0$ being the mass density ratio and bulk modulus ratio of the particle to the surrounding media. $K_0 = \rho_0 c_0^2$ for background medium, $K = \rho c^2$ for a droplet, and $K = \rho[c_L^2 - (4/3)c_T^2]$ for an elastic sphere with c_L and c_T being the longitudinal and transverse wave velocities of the material, respectively. In general, most ordinary particles, such as droplets or elastic spheres, have a phase-shift ratio beyond the allowable range ($0 < \delta_0/\delta_1 < 2$) and cannot be pulled in Rayleigh regime, for example, $\delta_0/\delta_1 = -4.3$ for a silica sphere in water, $\delta_0/\delta_1 = -11.1$ for a PMMA (a type of plastic) sphere in water, and $\delta_0/\delta_1 = -2$ for a rigid sphere [see Fig. 4.3(d)]. The acoustic properties of materials used in this chapter are found in Table 4.1.

Although for most ordinary particles, the phase shift ratios δ_0/δ_1 are outside the allowable range for acoustic pulling force, one can engineer proper objects with proper parameters to achieve the desired phase-shift ratio. Let us use a shell-like object, as an example. The phase shifts are a function of the size of the object (ka) and the inner-to-outer radius ratio (b/a) once the materials of the object and background medium are determined. There are totally two variables to control (i.e. ka and b/a). However, in this Rayleigh regime ($ka << 1$), the phase shift ratio δ_0/δ_1 in the

leading order is actually independent of ka,

$$\delta_0/\delta_1 = -2f_1/f_2, \tag{4.8}$$

where the monopole and dipole factors depend on b/a. Specifically, for a hollow elastic shell, the density ρ and bulk modulus K contained in $f_{1,2}$ in Eq. (4.7) should be replaced by effective mass density and effective bulk modulus:[140,141]

$$\rho_{\text{eff}} = [1-(b/a)^3]\rho,\ K_{\text{eff}} = \frac{[1-(b/a)^3]K}{1+(b/a)^3[0.75(c_L/c_T)^2-1]}. \tag{4.9}$$

Consequently, the only constraint on phase shift ratio δ_0/δ_1 can then be effectively controlled by the single parameter b/a. In Fig. 4.4(a), the b/a values corresponding to the phase shift ratio $0 < \delta_0/\delta_1 < 2$ are found for two different objects: a PMMA shell in water and a silica shell in water.

The advantage of the phase shift approach appears immediately in that one can directly obtain the minimum paraxial parameter β and then the corresponding object parameters efficiently in an analytical way. However, for conventional methods, one has to numerically search the whole beam and object parameter space to find the minimum angle and corresponding object parameters. For example, in Fig. 4.4(b), the dimensionless radiation force is calculated in the whole parameter space of $(b/a, \beta)$ based on the Eq. (4.3), and finally the minimum angle can be found after scanning the whole parameter space, which is quite time consuming and also less accurate compared with the phase shift approach since the resolution chosen for the numerical computations in conventional methods also affect the final results.

4.3 Beyond Rayleigh approximation

When the particles are beyond dipole regime, the situation is complicated since more phase shifts are involved. Furthermore, the phase-shift ratios including δ_0/δ_1 also depend on ka, or more specifically are a function of $(ka, b/a)$ for a given spherical shell. Nevertheless, the approach here

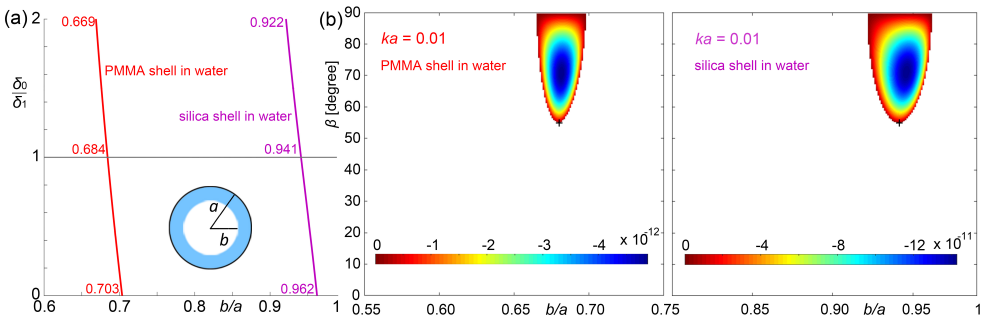

Figure 4.4: Engineered shell-like particles in Rayleigh regime ($ka << 1$). (a) Phase shift ratio δ_0/δ_1 is controlled by adjusting the inner-to-outer radius ratio b/a of a shell-like particle. Maximum range of phase shift ratio for pulling force is $0 < \delta_0/\delta_1 < 2$, and $\delta_0/\delta_1 = 1$ corresponds to the minimum paraxial parameter $\beta \approx 54.7°$ with corresponding b/a values marked. Inset: illustration of a shell-like object. (b) Dimensionless pulling force for two objects in the parameter space of $(b/a, \beta)$. Black pluses mark the locations where the minimum angle $\beta \approx 54.7°$ occurs using the phase shift method.

is to first fulfill the condition of the first two multipoles (monopole and dipole) to be in phase. Since there is only one constraint ($\delta_0 = \delta_1$) to follow yet there are two variables (ka and b/a) to control, it results in an infinite set of solutions corresponding to a line in $(ka, b/a)$ space [Fig. 4.5(a)]. That is, different b/a values are found for different ka values to at least satisfy $\delta_0 = \delta_1$. The first four phase shifts for these $(ka, b/a)$ values are further shown in Fig. 4.5(b), where $\delta_0 = \delta_1$ and the divergence of the phase shifts at certain ka is due to resonances of the shell.[6] Figures. 4.5(a) and (b) are obtained using the exact expressions of phase shifts for shells (see Appendix in Fan and Zhang;[19] alternatively, expansion of phase shifts to higher order[44,45,148,149] may be useful).

Now, in the quadrupole approximation, there are exactly *two* variables (ka and b/a) and *two* constraints ($\delta_0 = \delta_1 = \delta_2$), which means one set of $(ka, b/a)$ solution could be found, corresponding to one single point on the lines in Fig. 4.5(a). Following from the first three phase shifts in Fig. 4.5(b), the desired in-phase scattering occur at

$$b/a = 0.636 \text{ and } ka = 1.77, \tag{4.10}$$

where the phases are

$$\delta_0 = \delta_1 = \delta_2 = -0.1, \tag{4.11}$$

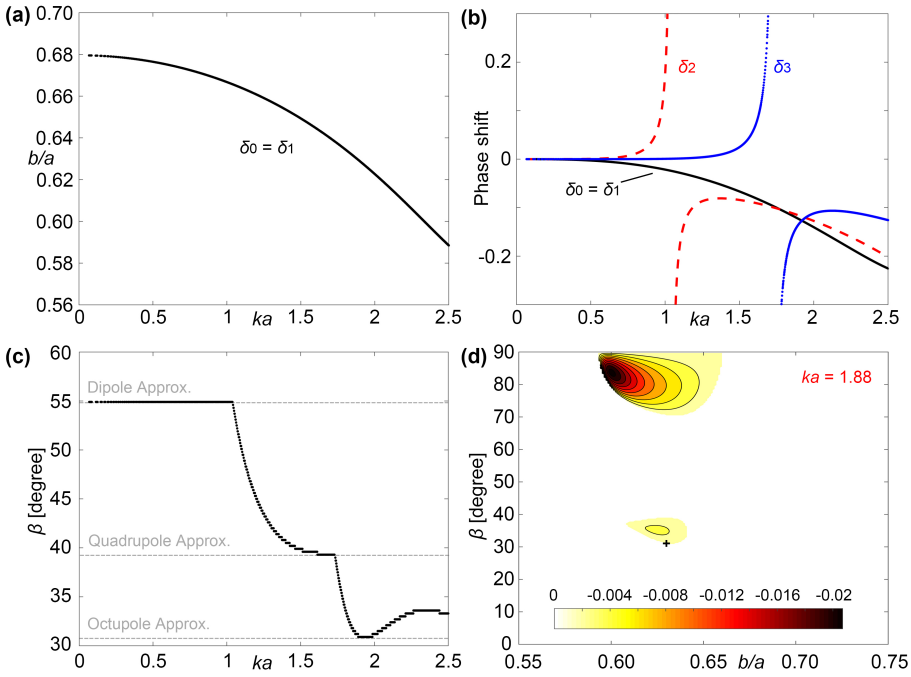

Figure 4.5: Beyond the Rayleigh approximation for PMMA shell in water. (a) b/a as a function of ka by satisfying $\delta_0 = \delta_1$. (b) The jumps of b/a result from resonances of phase shifts;[6] $\delta_0 = \delta_1 = \delta_2$ occurs at $ka = 1.77$. (c) Minimum achievable angle as a function of ka. Minimum angle about 31° occurs at $ka = 1.88$. (d) Negative dimensionless axial radiation force at $ka = 1.88$.

and the minimal angle should be $\beta = 39^\circ$ as analyzed in prior section.

To validate the parameters of $(ka, b/a)$ engineered here, the minimum angle β for a pulling force is calculated from Eq. (4.3) and shown in Fig. 4.5(c), showing that β does reduce to 39° at the engineered $(ka, b/a)$ value. Here in Fig. 4.5(c), for some large ka beyond the Rayleigh regime even up to $ka = 1$, the minimum angle still does not change much which is because the higher order terms are not excited yet due to the suppression of the quadrupole for $P_2(\cos\beta) = 0$ when $\beta = 54.7^\circ$.

As ka goes beyond the quadrupole approximation, there are *three* constraints ($\delta_0 = \delta_1 = \delta_2 = \delta_3$) which normally cannot be satisfied by only engineering *two* controllable variables $(ka, b/a)$ for spherical shells. That is, in principle, it is impossible to find exact solution for $\delta_0 = \delta_1 = \delta_2 = \delta_3$ to have a minimal $\beta = 31^\circ$ under such circumstance, so more complicated objects would be expected. However, one can seek parameters of the spherical shell to make the phase shifts as close to be in phase as possible. Fig. 4.5(b) shows that the four phase shifts are

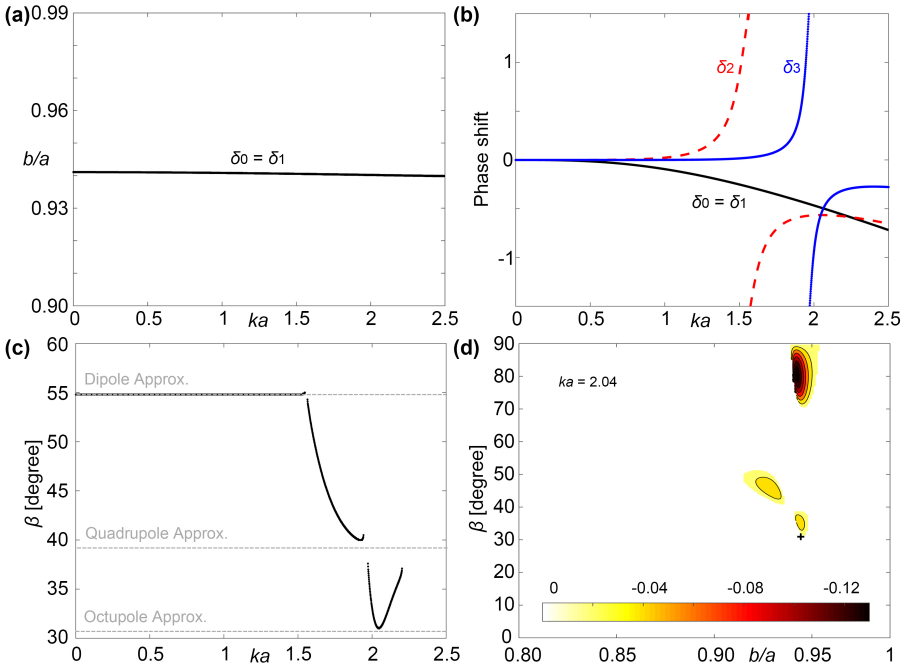

Figure 4.6: Beyond Rayleigh approximation for a silica shell in water. (a) b/a as a function of ka by satisfying the condition $\delta_0 = \delta_1$. (b) The first four phase shifts. (c) Minimum angle as a function of ka. Minimum angle about 31° occurs at $ka = 2.04$. (d) Negative dimensionless axial radiation force at $ka = 2.04$.

actually relatively close for ka between 1.5 and 2. To be exact, at

$$b/a = 0.630 \text{ and } ka = 1.88, \tag{4.12}$$

where the first four phase shifts are relatively close as

$$\delta_0 = \delta_1 = -0.12, \delta_2 = -0.11 \text{ and } \delta_3 = -0.14, \tag{4.13}$$

the minimum angle of 30.9° is achieved [Fig. 4.5(c)].

Again if one would like to find the desired object and beam parameters using this conventional method of direct computation, one has to compute the forces in the whole space of three parameters of ka, β, and b/a. A three dimensional numerical search would be considerably time consuming. The dimensionless radiation force at $ka = 1.88$ computed directly from Eq.(4.3) is shown in the parameter space of $(b/a, \beta)$ [Fig. 4.5(d)], confirming the parameters engineered

herein.

Figure 4.6 further shows the corresponding results for a silica shell in water. A minimum angle 31.2° is found within the octupole regime at

$$b/a = 0.941 \text{ and } ka = 2.04. \tag{4.14}$$

where the first four phase shifts are relatively close

$$\delta_0 = \delta_1 = -0.47, \delta_2 = -0.56 \text{ and } \delta_3 = -0.59. \tag{4.15}$$

It is worthy to note that, even for a spherical shell with two free geometric parameters, the in-phase scattering in the octupole regime is closely achieved. The angle around 30° is so far the minimum angle that has been found by using specific objects.

4.4 Conclusion

In this chapter, a systematic approach based on phase shifts from scattering was established to engineer the desired radiation force. The phase shift method can be used to analyze and design acoustic radiation force for *arbitrary* sound fields, simply by re-expressing the radiation force in terms of the phase shifts (or complex phase shifts depending on whether the dissipation is taken into account). With the aid of the phase shifts, the analytical expressions for acoustic radiation forces studied previously can be greatly simplified into a compact and physically meaningful form. As an example, an acoustic Bessel tractor beam on a spherical shell was designed with a paraxial parameter β about 30.9°, which is fulfilled by engineering the phase shifts up to the first four terms from multipole expansion. Although the shell-like objects used here only provide two variables to control (b/a and ka), yet they exhibit the advantages and performance of the phase shift method. For higher order terms of phase shifts, objects with more controllable variables will be needed such as objects of multiple layers or structured objects, which can provide extra degrees of freedom for modulation to make sure the constraints of phase shifts could be satisfied. More complex objects

would provide more flexibility, which will guide the realization of a even smaller angle or a much larger force. The phase shift method can also be extended for non-spherical objects or for the analysis of acoustic radiation torques.

CHAPTER 5

FORCES CAUSED BY OTHER EFFECTS

In the first part of this dissertation, the stable acoustic tractors that enable transversely stable *trapping* and axially negative *pulling* have been investigated. In practical situations and applications, in addition to the acoustic radiation force, the effects caused by gravity, buoyancy and streaming also need to be considered. The gravity and buoyancy for a spherical object totally immersed in a fluid can be obtained by $F^{\mathrm{G}} = \rho V g$ and $F^{\mathrm{B}} = \rho_0 V g$, respectively. Since the Bessel beams used here are travelling waves, they can manipulate particles far away from the walls or even in free space. In such case, the time-averaged Stokes drag force F^{D} on a spherical object of radius a caused by the acoustic streaming and the motion of the object can be expressed as,

$$F^{\mathrm{D}} = 6\pi\eta a|v_2 - u|, \tag{5.1}$$

where η is the dynamic viscosity ($\eta = 0.00089$ Pa $\cdot$ s for water at about $25°C$), u is the velocity of the moving object, and v_2 is the second-order streaming velocity of the fluid. $|v_2 - u|$ characterizes the magnitude of the relative motion between the acoustic streaming and the object (u and v_2 are in opposite directions). The effect caused by acoustic streaming will be discussed as follows.

5.1 Theory of acoustic streaming

Acoustic streaming can be analyzed from the basic equations including the continuity equation and Naiver-Stokes equation of the fluid mechanics:[150]

$$\frac{\partial \rho}{\partial t} + \nabla \cdot (\rho v) = 0 \tag{5.2}$$

$$\rho\left(\frac{\partial v}{\partial t} + v \cdot \nabla v\right) = -\nabla P + \mu\nabla^2 v + (\eta + \frac{1}{3}\mu)\nabla(\nabla \cdot v) \tag{5.3}$$

where v is the flow velocity vector, P is the pressure of a fluid, η and μ are the shear and the bulk viscosities of the fluid, respectively. Assuming the wave propagation is adiabatic process, one has

$$P(\rho) = P_0 + c_0^2\rho' + c_0(\frac{\partial c}{\partial \rho})_s\rho'^2 + ... \tag{5.4}$$

where P_0 is the atmospheric equilibrium pressure, ρ' the density fluctuation caused by the acoustic wave, c_0 and c are the acoustic velocities for the linear and nonlinear waves of the liquid, respectively, and s represents the entropy of the fluid. Start with

$$v = \epsilon v_1 + \epsilon^2 v_2 + ...,\ \rho' = \rho - \rho_0 = \epsilon\rho_1 + \epsilon^2\rho_2 + ..., \tag{5.5}$$

where ϵ is a small quantity of the first order, v_1, v_2, ρ_1, ρ_2 are the first order and second order of the fluid particle velocities and density fluctuations, respectively. Substituting Eqs. (5.4) and (5.5) into Eqs. (5.2) and (5.3), one obtains the first-order equations:

$$\frac{\partial \rho_1}{\partial t} + \rho_0\nabla \cdot v_1 = 0 \tag{5.6}$$

$$\rho_0\frac{\partial v_1}{\partial t} = -c_0^2\nabla\rho_1 + (\eta + \frac{4}{3}\mu)\nabla(\nabla \cdot v_1) - \mu\nabla \times \nabla \times v_1, \tag{5.7}$$

and the second-order equations:

$$\frac{\partial \rho_2}{\partial t} + \rho_0\nabla \cdot v_2 + \nabla \cdot (\rho_1 v_1) = 0 \tag{5.8}$$

$$\rho_0\frac{\partial v_2}{\partial t} + \rho_1\frac{\partial v_1}{\partial t} + \rho_0(v_1 \cdot \nabla)v_1 = -c_0^2\nabla\rho_2 - c_0(\frac{\partial c}{\partial \rho})_s\nabla\rho_1^2 + (\eta + \frac{4}{3}\mu)\nabla(\nabla \cdot v_2) - \mu\nabla \times \nabla \times v_2. \tag{5.9}$$

With the aid of the first-order equations [Eqs. (5.6) and (5.7)], the second-order equations [Eqs. (5.8) and (5.9)] can be simplified as:

$$\frac{\partial(\rho_2 - \Omega/c_0^2)}{\partial t} + \rho_0 \nabla \cdot v_2 = \frac{1}{\rho_0 c_0^2}\left(\eta + \frac{4}{3}\mu\right) v_1 \cdot \nabla\left(\frac{\partial \rho_1}{\partial t}\right) \tag{5.10}$$

$$\begin{aligned}\rho_0 \frac{\partial v_2}{\partial t} + c_0^2 \nabla(\rho_2 - \Omega/c_0^2) = -c_0 (\frac{\partial c}{\partial \rho})_s \nabla \rho_1^2 - \frac{1}{\rho_0}\left(\eta + \frac{4}{3}\mu\right)\rho_1 \nabla(\nabla \cdot v_1) \\ + \left(\eta + \frac{4}{3}\mu\right)\nabla(\nabla \cdot v_2) - \mu \nabla \times \nabla \times v_2 - \nabla(\rho_0 v_1^2)\end{aligned} \tag{5.11}$$

where $\Omega = \frac{c_0^2 \rho_1^2}{2\rho_0} + \frac{\rho_0}{2} v_1^2$ is the energy per unit volume of the linearized acoustic wave. Performing the operations of $\nabla\cdot$ and $\nabla\times$ on both side of Eq. (5.11), one obtain:

$$\begin{aligned}\frac{\partial^2 D_2}{\partial^2 t} - c_0^2 \nabla \cdot (\nabla D_2) - \frac{1}{\rho_0}\left(\eta + \frac{4}{3}\mu\right)\nabla^2(\partial D_2/\partial t) = -\frac{1}{\rho_0^2}\left(\eta + \frac{4}{3}\mu\right)\nabla^2[v_1 \cdot \nabla(\partial \rho_1/\partial t)] \\ -\frac{1}{\rho_0^2}\left(\eta + \frac{4}{3}\mu\right)\nabla \cdot \frac{\partial(\rho_1 \nabla D_2)}{\partial t} - \frac{1}{\rho_0}\frac{\partial}{\partial t}\nabla^2[c_0(\frac{\partial c}{\partial \rho})_s \rho_1^2 + \rho_0 v_1^2],\end{aligned} \tag{5.12}$$

and

$$\frac{\partial R_2}{\partial t} - \frac{\mu}{\rho_0}\nabla^2 R_2 = \frac{1}{\rho_0^3}\left(\eta + \frac{4}{3}\mu\right)\left(\nabla \rho_1 \times \nabla \frac{\partial \rho_1}{\partial t}\right), \tag{5.13}$$

where $D_2 = \nabla \cdot v_2$ and $R_2 = \nabla \times v_2$. Note that the identity $\nabla \times \nabla \times R_2 = \nabla(\nabla \cdot R_2) - \nabla^2 R_2 = -\nabla^2 R_2$ has been used.

Supposing that the first-order acoustic wave has the form of

$$\rho_1(r, f) = \frac{1}{c_0^2}[P_1(r)\cos(\omega t) + P_2(r)\sin(\omega t)], \tag{5.14}$$

where $P_1(r)$ and $P_2(r)$ are spatial functions. Thus, one obtain that:

$$\nabla \rho_1 = \frac{1}{c_0^2}[\nabla P_1(r)\cos(\omega t) + \nabla P_2(r)\sin(\omega t)] \tag{5.15}$$

$$\nabla\frac{\partial\rho_1}{\partial t} = \frac{\omega}{c_0^2}[-\nabla P_1(r)\sin(\omega t) + \nabla P_2(r)\cos(\omega t)] \tag{5.16}$$

and $\nabla\rho_1 \times \nabla(\partial\rho_1/\partial t) = (\omega/c_0^4)\nabla P_1(r) \times \nabla P_2(r)$ becomes time-independent. Hence, the steady-state equation for R_2 becomes:

$$\nabla^2 R_2 = -\frac{\omega}{\rho_0^2 c_0^4}\left(\frac{\eta}{\mu} + \frac{4}{3}\right)\nabla P_1(r) \times \nabla P_2(r). \tag{5.17}$$

Now, considering one example of Eckart's streaming in a finite rigid cylindrical tube of radius $\rho = a$. Assume the tube is terminated with a perfect absorber to avoid the reflection at the end of the tube. An acoustic wave transmitter located at the mouth of the tube emanates an acoustic wave propagating along the axial direction of the tube (z-direction). The tube is completely sealed, and no energy exchange takes place with the interior of the tube and the outside of it. Let the first-order traveling wave expressed as

$$p_1(r, f) = c_0^2\rho_1 = P(\rho)\sin(\kappa z - \omega t) \tag{5.18}$$

where $P(\rho)$ is a spatial function and κ is the axial wavenumber. One obtain

$$\nabla^2 R_2 = -\frac{\omega}{\rho_0^2 c_0^4}\left(\frac{\eta}{\mu} + \frac{4}{3}\right)\nabla P_1(r) \times \nabla P_2(r) = b\frac{dP^2(\rho)}{d\rho}e_\phi, \text{ with } b = \frac{\omega\kappa}{2\rho_0^2 c_0^4}\left(\frac{\eta}{\mu} + \frac{4}{3}\right) \tag{5.19}$$

Here $\nabla^2 R_2$ has only e_ϕ component and independent of ϕ, hence, R_2 also has only a component in e_ϕ direction, i.e., $R_2 = f(\rho)e_\phi$, where $f(\rho)$ satisfies

$$\frac{d}{d\rho}\left[\frac{1}{\rho}\frac{d[\rho f(\rho)]}{d\rho}\right] = b\frac{dP^2(\rho)}{d\rho}. \tag{5.20}$$

Performing integration on the above equation, one obtain

$$R_2 = f(r)e_\phi = \left[\frac{b}{\rho}\int_0^\rho \rho' P^2(\rho')d\rho' + 2N\rho + \frac{M}{\rho}\right]e_\phi \tag{5.21}$$

where N and M are integration constants and M should be zero to make $f(\rho)$ is finite at $\rho = 0$. Recall that $R_2 = \nabla \times v_2$ is in e_ϕ direction, $v_{2\rho} = v_{2\phi} = 0$, and v_{2z} satisfies

$$-\frac{\partial v_{2z}}{\partial \rho}(\rho e_\phi) = b \int_0^\rho \rho' P^2(\rho') d\rho' + 2N\rho. \tag{5.22}$$

One obtain

$$v_{2z}(\rho) = bw(\rho) + 2N(a^2 - \rho^2) \tag{5.23}$$

with

$$w(\rho) = \int_\rho^a \frac{1}{\rho''} \left[\int_0^{\rho''} \rho' P^2(\rho') d\rho' \right] d\rho'' \tag{5.24}$$

where the nonslip boundary condition has been used, i.e., $v_{2z}(a) = 0$. The total mass flow at any cross section should be zero for a steady flow,

$$\int_0^a v_{2z}(\rho) \rho d\rho = 0, \tag{5.25}$$

which can be used to determine the constant N.

Here, the spatial function of the pressure amplitude of the acoustic source is $P(\rho) = P_0 J_0(\mu\rho)$ as $0 < \rho < \rho_0$ and $P(\rho) = 0$ as $\rho_0 < \rho < a$, where ρ_0 is the beam-width of the acoustic source. One can first calculate the integration within the bracket in Eq. (5.24)

$$\int_0^{\rho''} \rho' P^2(\rho') d\rho' = \int_0^{\rho''} \rho' P_0^2 J_0^2(\mu\rho') d\rho' = P_0^2 \frac{\rho''^2}{2} [J_0^2(x'') + J_1^2(x'')] \text{ if } \rho'' < \rho_0; \tag{5.26}$$

$$\int_0^{\rho''} \rho' P^2(\rho') d\rho' = \int_0^{\rho_0} \rho' P_0^2 J_0^2(\mu\rho') d\rho' = P_0^2 \frac{\rho_0^2}{2} [J_0^2(x_0) + J_1^2(x_0)] \text{ if } \rho'' > \rho_0, \tag{5.27}$$

where $x'' \equiv \mu\rho''$ and $x_0 \equiv \mu\rho_0$ with μ being the transverse wavenumber and $\mu^2 + \kappa^2 = k_0^2 = \omega^2/c_0^2$.

Substituting the results into Eq. (5.24), one obtain when $\rho > \rho_0$,

$$w(\rho) = P_0^2 \frac{\rho_0^2}{2} [J_0^2(x_0) + J_1^2(x_0)] \ln(\frac{a}{\rho}), \tag{5.28}$$

when $0 < \rho < \rho_0$,

$$w(\rho) = \frac{P_0^2}{2\mu^2}\left[t^2\left(J_0^2(t) + J_1^2(t)\right) - tJ_0(t)J_1(t)\right]_{t=x\equiv\mu\rho}^{t=x_0=\mu\rho_0} + P_0^2\frac{\rho_0^2}{2}[J_0^2(x_0) + J_1^2(x_0)]\ln(\frac{a}{\rho_0}). \quad (5.29)$$

Recall that $v_{2z}(\rho) = bw(\rho) + 2N(a^2 - \rho^2)$ and $\int_0^a v_{2z}(\rho)\rho d\rho = 0$, one obtain that

$$b\int_0^a w(\rho)\rho d\rho + 2N\int_0^a (a^2 - \rho^2)\rho d\rho = 0, \quad (5.30)$$

and in turn obtain the expression of the integration constant

$$N = \frac{bP_0^2 G}{6\mu^4 a^4} \quad (5.31)$$

with

$$G = J_0(x_0)J_1(x_0)x_0^3 - J_0^2(x_0)x_0^4(1+t) - J_1^2(x_0)[x_0^2 + x_0^4(1+t)] \text{ and } t = \frac{3a^2}{2\rho_0^2} - \frac{3}{2} - 3\ln(\frac{a}{\rho_0}). \quad (5.32)$$

Note that these identities have been used during the calculation:

$$\int \ln(\frac{a}{x})xdx = \frac{x^2}{4}\left[2\ln(\frac{a}{x}) + 1\right] \quad (5.33)$$

$$\int x^2 J_0(x)J_1(x)dx = \frac{x^2}{2}J_1^2(x) \quad (5.34)$$

$$\int xJ_0^2(x)dx = \frac{x^2}{2}[J_0^2(x) + J_1^2(x)] \quad (5.35)$$

$$\int xJ_1^2(x)dx = \frac{x}{2}[xJ_0^2(x) + xJ_1^2(x) - 2J_0(x)J_1(x)] \quad (5.36)$$

$$\int x^3 J_0^2(x)dx = \frac{x^4}{6}J_0^2(x) + \frac{x^3}{3}J_0(x)J_1(x) + \left(\frac{x^4}{6} - \frac{x^2}{3}\right)J_1^2(x) \quad (5.37)$$

$$\int x^3 J_1^2(x)dx = \frac{x^4}{6}J_0^2(x) - \frac{2x^3}{3}J_0(x)J_1(x) + \left(\frac{x^4}{6} + \frac{2x^2}{3}\right)J_1^2(x). \quad (5.38)$$

Hence, the velocity at $\rho = 0$ can be obtained as

$$v_{2z}(\rho = 0) = \frac{bP_0^2}{2\mu^2}\left[x_0^2\Big(J_0^2(x_0) + J_1^2(x_0)\Big)\Big(1 + \ln(\frac{a}{\rho_0})\Big) - x_0 J_0(x_0)J_1(x_0) + \frac{2G}{3\mu^2 a^2}\right]. \tag{5.39}$$

Recall that b is given in Eq. (5.19), G is given in Eq. (5.32), a is the radius of the cylindrical container, ρ_0 is the radius of the acoustic source or the transducer, μ is the transverse wavenumber, and P_0 is a constant, related to the incident pressure amplitude. Note that when $\beta = 0°$, Eq. (5.39) is reduced to Eq. (35) in Wu [150] for the case of an incident plane wave, i.e.,

$$v_{2z}^{\beta=0°}(\rho = 0) = \frac{bP_0^2\rho_0^2}{4}\left[\frac{\rho_0^2}{a^2} + 2\ln(\frac{a}{\rho_0}) - 1\right]. \tag{5.40}$$

Now, considering a practical case of using acoustic tractor beam to pull a silica shell in water with the inner-to-outer radius ratio of the shell being 0.93 and the total radius of shell being 0.5 mm. The diameter of the transducer is $\rho_0 = 1$ in, and the central frequency is 1 MHz. The radius of the rigid cylinder is $a = 1$ m, which is about 100 times larger than the transducer diameter. The power ($P = P_0^2/2\rho_0 c_0 \cdot S$ with S being the area of the transducer) is chosen as 25 Watt.

Substituting all these parameters into Eq. (5.39), one obtains the streaming velocity of the fluid is $v_2 = 1.4$ mm/s. Under such circumstance, the force applying to the silica shell including the radiation force (F^{rad}), gravity (F^G), buoyancy (F^B), and the drag force (F^D) has been calculated and analyzed in Fig. 5.1(a), where the magnitude of the negative radiation force are compared to the magnitude of the total force caused by other effects except radiation force. It is found that within some range of the paraxial parameter, the acoustic beams can truly pull a particle towards the source even when considering the practical effects.

5.2 Particle motion under radiation force, gravity, buoyancy and drag force

The dynamical change of the object velocity u can be obtained from the Newton's equation

$$F^{rad} + F^G - F^B - F^D(u) = M\frac{du}{dt}, \tag{5.41}$$

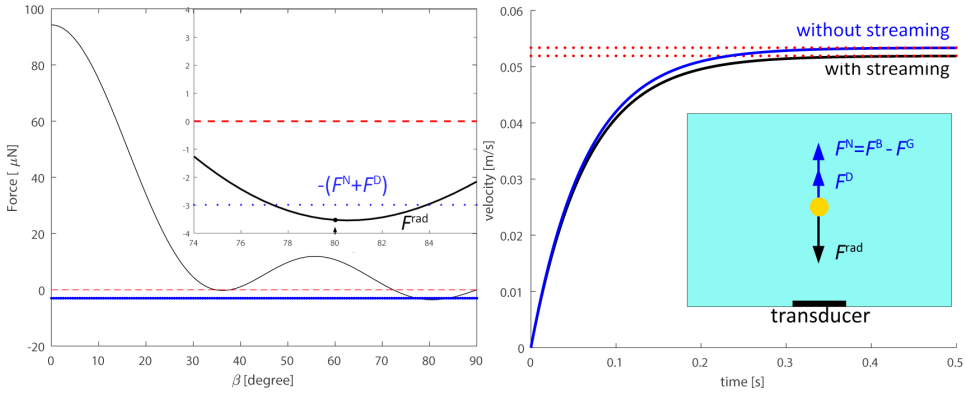

Figure 5.1: Particle manipulation including the effects caused by the gravity, buoyancy, and the drag force. (a) Acoustic radiation force (black solid curve) on a silica shell as a function of paraxial parameter β. Inset: zoom-in plot corresponding to the region marked by the grey box in (a). (b) Dynamical change of velocity of the particle as a function of time when suffering from the radiation force (F^{rad}), gravity (F^G), buoyancy (F^B), and the drag force (F^D) as illustrated in the Inset in (b). The net buoyancy $F^N = F^B - F^G$.

where M is the mass of the silica shell. The explicit expression of the object velocity is

$$u = \frac{A}{B}(1 - e^{-Bt}) \tag{5.42}$$

where $A = (F^{rad} + F^G - F^B - 6\pi\eta a v_2)/M$ and $B = 6\pi\eta a/M = 9\eta/2\rho a^2$. Corresponding results are shown in Fig. 5.1(b), where the velocity reaches the maximum value after 0.3 s. It is worth noting that the drag force caused by the streaming here is about three orders small than the other forces ($F^D = 0.004F^N$,$F^D = 0.0035F^{rad}$), and the streaming does not affect the change rate of the object velocity [see the term B in Eq. (5.42)], instead it only affects the maximum object velocity with the maximum velocity difference w/o streaming equal to the streaming velocity [see the term A/B in Eq. (5.42)].

5.3 Comparison of acoustic radiation forces and the streaming force

As mentioned above, the streaming force for the case considered here is much smaller than the radiation force, which is because the object considered here is relatively large, and the boundary layer δ is much smaller than the particle size a and can be neglected [see Eq. (2.13);

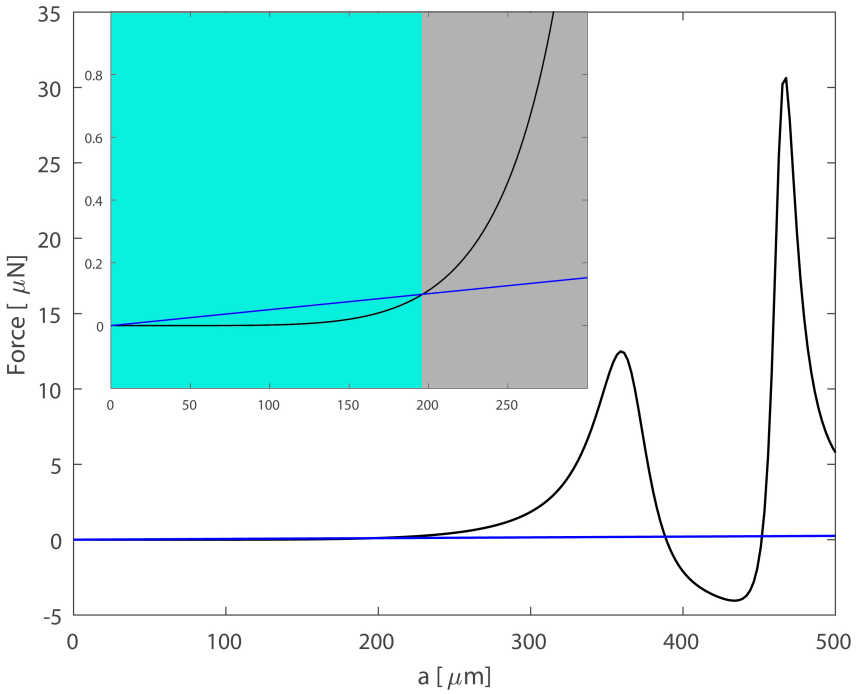

Figure 5.2: Acoustic radiation force and streaming force for the silica shell of different radii. Inset: zoom-in plot for the object radius within the range of 0 to 500 μm.

$F^D \propto (\delta/a)^2 \cdot a^3$]. To further investigate the streaming effect on the objects of different sizes, the acoustic radiation force is compared with the drag force caused by the streaming for the same silica shell with radii varying from 0 to 500 μm (Fig. 5.2). The streaming force dominates when the objects are relatively small, and the radiation force gradually dominates as the objects are getting larger. The reason is that the radiation force[41] is proportional to $(ka)^6$ and the streaming force [Eq. (5.1)] is proportional to ka, leading that the streaming force is much larger than the radiation force when ka is small. Hence, large objects are usually preferred since acoustic radiation forces for large objects are usually much larger than the streaming force unless the radiation force is close to 0 for some specific ka.

The difference of the magnitude of the radiation force and the streaming force, i.e. $|F_z| - F_{drag}$, in the parameter space of ka and a is shown in Fig. 5.3, in which the blue color marks the region where the streaming force dominates. Note that, the radiation force only depends on ka, however, the streaming force depends on both ka and a; see Eqs. (5.1) and (5.39). Generally

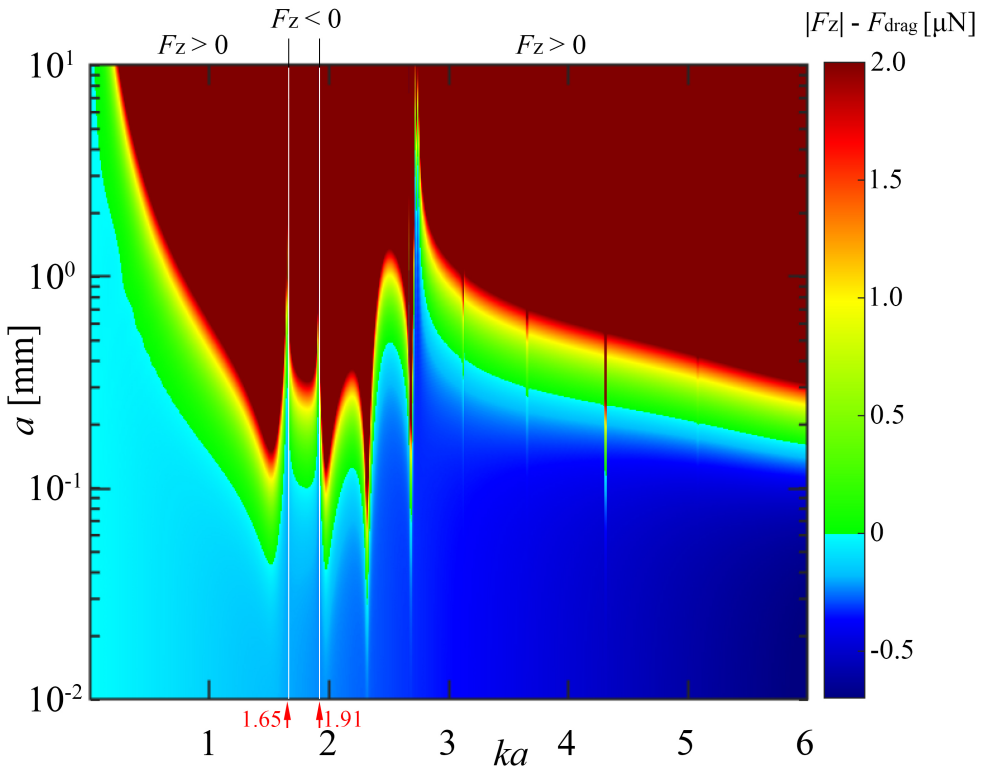

Figure 5.3: Difference of the magnitude of the radiation force and the streaming force, i.e. $|F_z| - F_{drag}$, in the parameter space of ka and a. The region where the radiation force is negative is marked between the two vertical white lines, corresponding to the range of $1.65 < ka < 1.91$.

speaking, the streaming force dominates when a is small for a specific ka, especially for a small ka ($ka << 1$). The exact transition between the radiation force and the streaming force depends on the working frequency, the paraxial parameter, properties of objects and background medium.

CHAPTER 6

REFRACTION OF ACOUSTIC VORTEX BEAMS IN INHOMOGENEOUS MEDIA

The second portion of the dissertation focuses on the acoustic vortices in inhomogeneous media. The effects caused by medium inhomogeneity on the propagation of acoustic ordinary/vortex beams are fundamental and vital to address since the media are often inhomogeneous in practical situations or applications. In this chapter, the refraction of acoustic vortex beams in stratified inhomogeneous media and the interactions between acoustic vortices and medium inhomogeneity are investigated.

6.1 Method

The propagation of ultrasonic vortex fields in a linearly stratified fluid is simulated, where the sound speed is $c = c_0 - Gz$, such as that considered in Zhang and Swinney[86] and Schoen and Arvanitis.[89] The gradient is as large as $G = 58$ m/s per mm, which enhances the stratification effect in a short propagating distance (that saves the simulation load). The typical sound speed in fluids $c_0 = 1500$ m/s at the vortex source center is used and the variation of fluid density is neglected. A finite plane source with a diameter of 15λ is used, which is at the order of 1-inch diameter transducer for 1 MHz ultrasound with a wavelength $\lambda = 1.5$ mm.

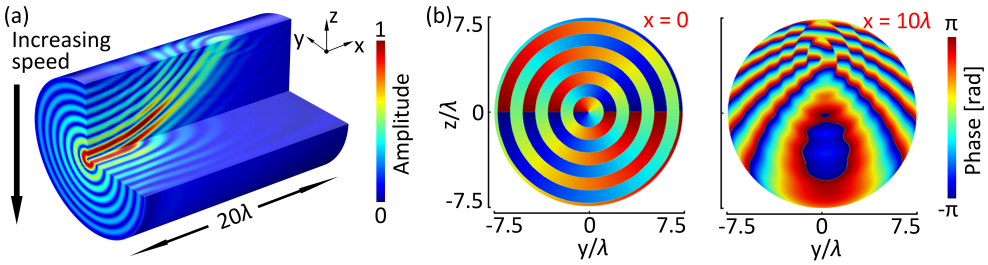

Figure 6.1: (a) Simulation of vortex waves bending in a stratified medium. (b) Stretching and distorting of the phase on y-z cross sections at different propagating distances x.

The simulated source profile has a topological charge of -1 in polar coordinates (ρ, ϕ), $\psi = J_1(\mu\rho)e^{-i\phi}e^{-i\omega t}$, where J_1 is the first-order Bessel function, ω is angular frequency, and μ is the transverse wave number (chosen to be half of the total wave number $k = \omega/c_0$, i.e., $\beta = 30°$). The simulation is conducted with a finite element method based on COMSOL MULTIPHYSICS software. Radiation boundary conditions are applied to outer boundaries of the calculation domain (a cylinder with 15λ in diameter and 20λ in length) to model the propagation in a free space without reflection. The source is located at $x = 0$ plane [Fig. 6.1(a)].

6.2 Numerical results

Figure 6.1(a) shows the simulated three-dimensional wave amplitude. The vortex beam bends upwards towards $+z$ direction as expected due to the refraction. Figure 6.1(b) displays the phase distortions on y-z plane at different x. Overall, the vortex beam bends upwards and is stretched in the stratified direction.[1] The evolution of the wave amplitude during the propagation is then examined [Fig. 6.2(a)]. Unexpectedly, the amplitude is *asymmetric* in the non-stratified y direction (relative to $y = 0$), arising from the fact that the vortices rotate clockwise so the propagation direction is along or against the upward refraction, depending on the positive or negative y values, respectively [Fig. 6.2(b)].

The trajectory of the vortex center which is identified from the singular point of the phase distribution is displayed in Fig. 6.2(c). The singular trajectory is compared with a horizontally emitted eigenray from a point source (black dashed line), which is an arc of a circle c_0/G in a linearly stratified medium.[86] The results show that the singular trajectory does *not* lie on the eigenray of the point source. For comparison, a beam from the same source but without the vortex phases [i.e., a zero-order beam, $\psi = J_0(\mu\rho)e^{-i\omega t}$] is simulated, where the trajectory of the central pressure maximum [Fig. 6.2(c)] does coincide with the singular trajectory of the vortex beam, revealing that the singular trajectory follows the path of a beam emitted by a finite-size source. The behaviors of singular trajectory will be further studied in the future.

[1] See Supplemental Material at http://link.aps.org/supplemental/10.1103/PhysRevResearch.1.032014 for the evolution of the phase, amplitude, and transverse energy flux

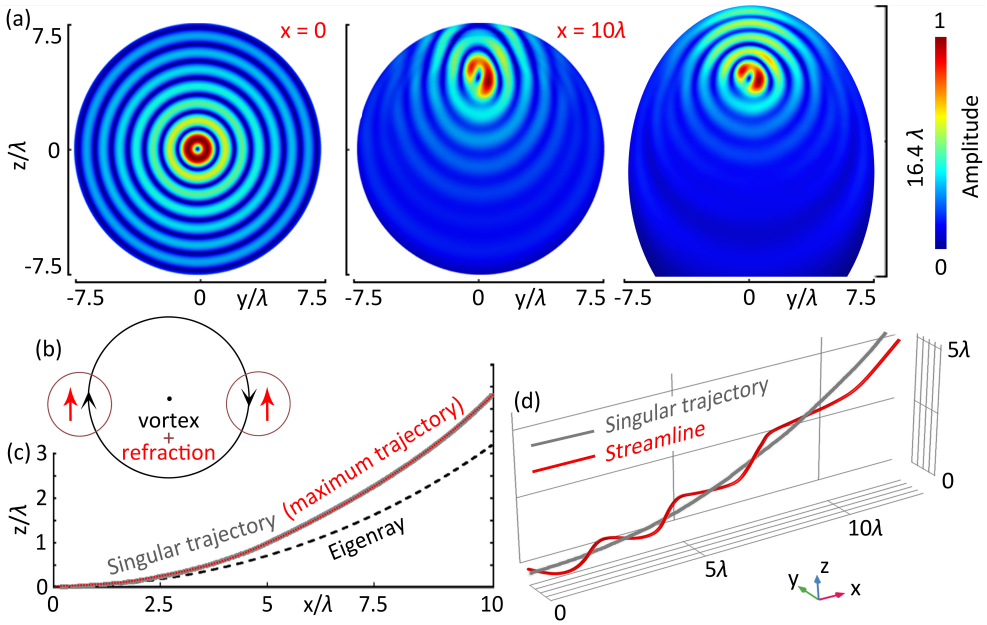

Figure 6.2: (a) Stretching and distortion of amplitude on y-z cross sections at $x = 0$ (left) and 10λ (middle), and on the cross section *perpendicular* to the singular trajectory through the singular point at $x = 10\lambda$. (b) Illustration of the mechanism of amplitude asymmetry. Red arrows represent the refraction direction by stratification. (c) Singular trajectory on z-x plane (gray solid line) and its comparison with a horizontally emitted eigenray (black dashed line) and a maximum amplitude trajectory from a zero-order Bessel beam propagating in the same media (red dotted line). (d) Three-dimensional energy flux and vortex center. A three-dimensional streamline starting from $(0, 0, 0.25\lambda)$ and twisting around the vortex center (singular trajectory) is untwisted beyond a certain distance.

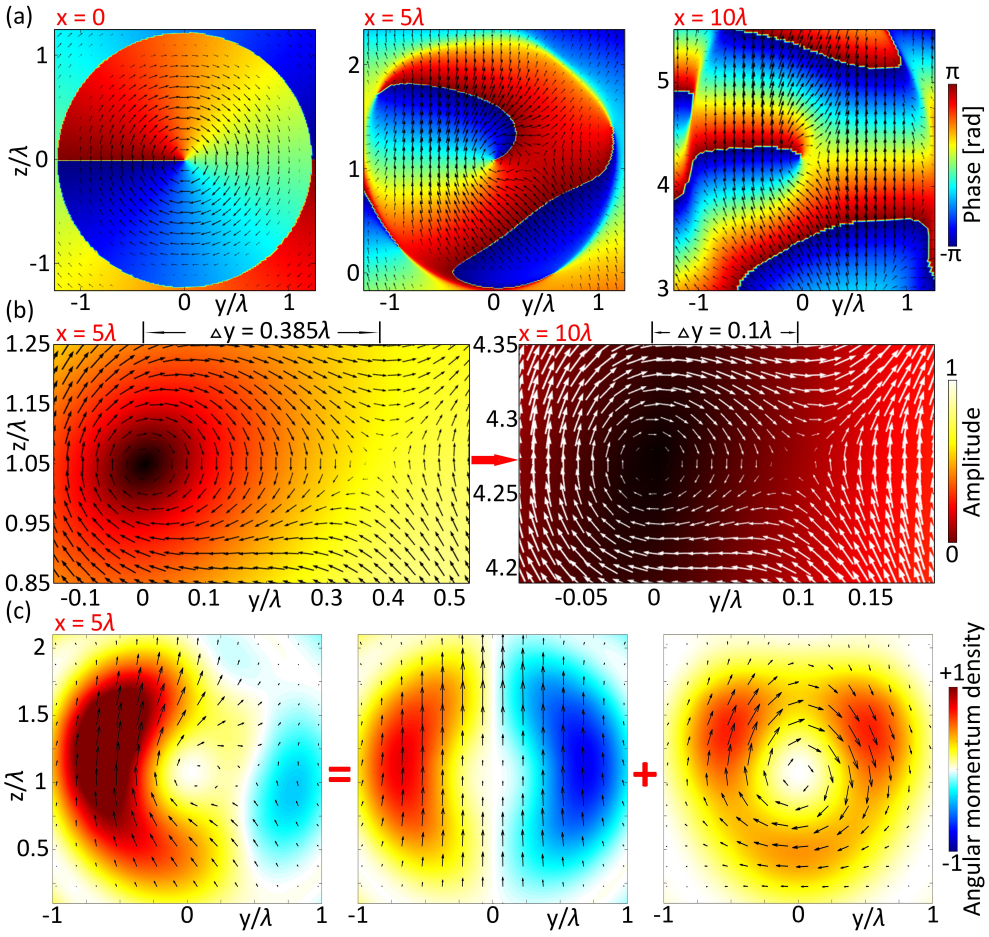

Figure 6.3: Features of transverse energy flux (arrows): (a) Reversal from clockwise to counter-clockwise, (b) migration of an additional singular point of saddle type towards the vortex center [zoom-in areas of panels in (a)], and (c) separation into two portions – the stratified effect where the flux is upwards (middle panel) and a reconstructed vortex (right-hand-side panel). Color plots in (a) show the phase distribution, in (b) show the wave amplitude, and in (c) show angular momentum density.

The transport of energy is calculated by examining the time-averaged energy flux over a wave period, $\mathbf{S} = c^2\mathbf{g}$,[62] where the time-averaged momentum density $\mathbf{g} = \mathrm{Im}(\psi^*\nabla\psi)$ is calculated from the complex scalar field ψ and its gradient (Im represents the imaginary part and a prefactor is suppressed in the normalization of ψ). The flux is illustrated by one typical streamline in Fig. 6.2(d), showing that the energy flux is transformed from twisted into *untwisted* and simply bends upwards at a large distance. The transition results from the fact that, as the wave propagates and the vortex spreads, the upward energy flux due to the stratification gradually dominates.

The transverse flux at different propagating distances x is further shown in Fig. 6.3(a) by

arrow plots. The flux is *reversed* on the positive y side as the wave propagates. The direction of energy flux corresponds to the gradient of phase of wave propagation [Fig. 6.3(a)]. Reversal of the flux implies the opposite propagation of the vortex beam, resulting from an additional upward energy flux by the refraction. The transition of flux direction is at locations where the upward flux by refraction cancels with the clockwise vortex flux, leading to the emergence of another singular point where the transverse energy flux is zero [Fig. 6.3(b)]. This singular point of transverse energy flux is of saddle type, in contrast to the center point of the vortex beam. As the vortex beam propagates and spreads, the saddle point migrates towards the center point of the vortex beam. Note that at this additional singular point, the pressure [Fig. 6.3(b)] and axial velocity are not zero, so there is still a flux along the propagating x direction at these locations.

Even though the vortices are unstable and untwisted by the stratification as observed, an approach is proposed to individually visualize the vortex flow and the stratified effect by separating the transverse energy flux into two portions. The first portion is the background flux (denoted by $\mathbf{g}^{\mathrm{B}}$) obtained by taking the antisymmetrical (symmetrical) part of energy flux in the horizontal y (vertical z) direction, namely,

$$\mathbf{g}_y^{\mathrm{B}}(y,z) = [\mathbf{g}_y(y,z) - \mathbf{g}_y(-y,z)]/2, \tag{6.1}$$

$$\mathbf{g}_z^{\mathrm{B}}(y,z) = [\mathbf{g}_z(y,z) + \mathbf{g}_z(-y,z)]/2. \tag{6.2}$$

The second portion is the vortex flux (denoted by $\mathbf{g}^{\mathrm{V}}$) obtained by taking the symmetrical (antisymmetrical) part of energy flux in vertical y (horizontal z) direction, namely,

$$\mathbf{g}_y^{\mathrm{V}}(y,z) = [\mathbf{g}_y(y,z) + \mathbf{g}_y(-y,z)]/2, \tag{6.3}$$

$$\mathbf{g}_z^{\mathrm{V}}(y,z) = [\mathbf{g}_z(y,z) - \mathbf{g}_z(-y,z)]/2. \tag{6.4}$$

The separation is illustrated in Fig. 6.3(c), where the transverse energy flux in the left-hand-side panel is separated into a *upward* background flux in the middle panel and a *reconstructed* clockwise

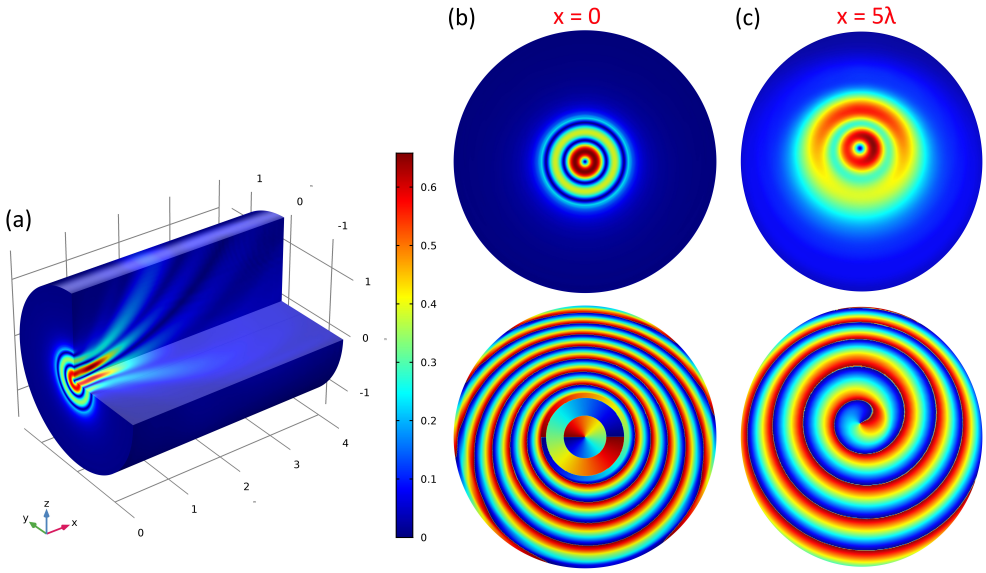

Figure 6.4: (a) Simulation of vortex waves bending in a stratified medium. Amplitude and phase on y-z cross sections at (b) $x = 0$ and (c) $x = 5\lambda$.

vortex in the right-hand-side panel.

Lastly, the angular momentum density $\mathbf{j} = \mathbf{r} \times \mathbf{g}$ is displayed in Fig. 6.3(c) by its axial x component (color plots), calculated from the momentum density $\mathbf{g}$ and the relative distance to the vortex center at the corresponding cross section. The total angular momentum density in the left-hand-side panel is a sum of angular momentum density in the middle panel and the reconstructed vortex in the right-hand-side panel. There is no contribution to the total angular momentum contained in the whole cross section from the refraction in the middle panel, where the angular momentum density is antisymmetric with respect to $y = 0$). The total angular momentum contained in the original vortex is equal to the total angular momentum of the reconstructed vortex. The separation of the stratified part does not change the total angular momentum other than redistributing the angular momentum density in the cross section.

In order to make sure that the effect caused by the reflection from the outer radiation boundaries can be neglected and the results obtained previously are reliable, a vortex beam generated from a smaller source propagating in the same media is simulated with the results shown in Fig. 6.4. The result shows the diffraction of the vortex beam during propagation, and the amplitude asymmetry still exists, which agrees with the previous observation.

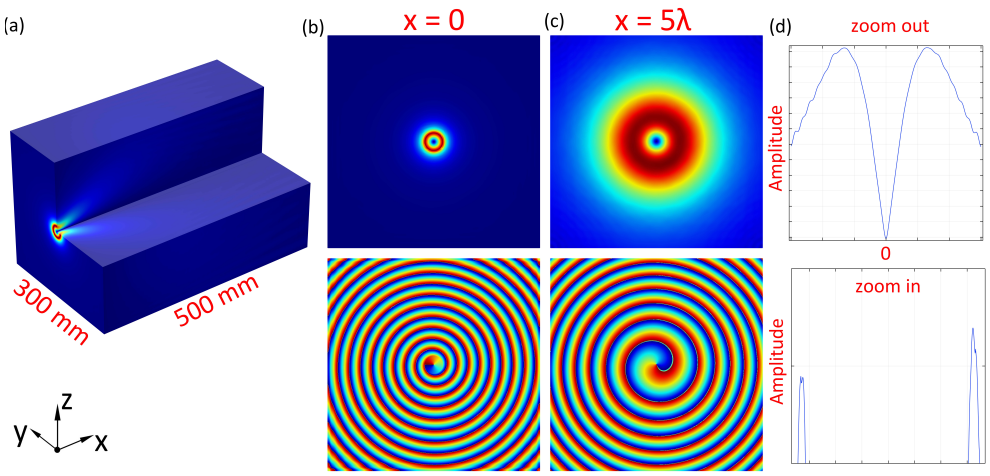

Figure 6.5: (a) Simulation of vortex waves bending in a stratified medium. Amplitude and phase on y-z cross sections at (b) $x = 0$ and (c) $x = 5\lambda$. (d) Amplitude profile along the line of $z = 0$ at the propagating distance $x = 5\lambda$.

The propagation of the vortex beam in a practical medium with reasonable parameters is simulated in Fig. 6.5, where the diameter of the source is set as 1 inch, which is a typical diameter of a transducer, the density and sound speed gradient long z direction are set as 0.2255 kg/m^3 per mm, and 0.377 m/s per mm, respectively and the density and sound speed at z = 0 are 1000 kg/m^3 and 1600 m/s. The dimensions of the computation domain are 300 mm $\times$ 300 mm $\times$ 500 mm. The frequency is chosen as 100 kHz. These parameters, which simulate the ocean environment, are from Zhang and Swinney.[86] The effects are much weaker in this simulation due to the small gradient, but the amplitude asymmetry still exists as shown in Fig. 6.5(d), where the zoom-in plot shows the amplitude asymmetry in the non-stratified y direction.

6.3 Remarks

In this chapter, some unusual behaviors of acoustic singularities and vortices in stratified media are reported. It is found that the stratification feature leads to the distortion and complex behaviors of the vortices via the emergence of bending, distorting, focusing, and stretching of the fields, or even the reversal of the energy and momentum transports, and angular momentum.

All of the observations herein suggests the complexity of applications of vortices in inhomogenous media, for example, in the contexts of oceans and ultrasound. For the purpose of

underwater navigation and communication, it becomes a challenge to decompose the vortices of different topological charges in the stratified ocean. The findings of distortion of energy flux and angular momentum of vortices by the refraction can lead to new phenomena of vortex-based particle manipulations in inhomogeneous fluids, where the spatial gradient plays a central role.[151] One scenario is the particle manipulation and transport in presence of a thermal gradient,[152–154] where the distortion of the vortex propagation by the gradient as observed here may need to be taken into account.

CHAPTER 7

ACOUSTIC ORBITAL HALL EFFECT

This chapter observes and characterizes the acoustic orbital angular momentum Hall effect which is related to the coupling between intrinsic orbital angular momentum (IOAM) and extrinsic orbital angular momentum (EOAM) (Fig. 7.1). The transverse shifts of the beam center related to the orbital Hall effect are observed via simulation and modeling of a vortex beam propagating in a smoothly inhomogeneous medium. The simulated results are compared with a theoretical prediction characterizing the dependence of the shift on physical parameters (helicity, wavenumber, and medium inhomogeneity). This work reveals the existence of the orbital Hall effect in acoustics and introduces the study of angular momentum coupling in acoustics.

7.1 Numerical observation of helicity-dependent transverse shift

An acoustic vortex beam propagating in a linearly-stratified medium was simulated using the commercial software COMSOL MULTIPHYSICS (Acoustic Module). The dimensions of the computational domain are set to $\lambda_0 \times 3\lambda_0 \times 4\lambda_0$, where λ_0 is a reference wavelength. Non-reflection boundary conditions are used to eliminate the disturbance caused by reflection. A circular plane source ($0.5\lambda_0$ in radius) with a profile $\exp[i(\omega t - l\phi)]$ is located in y-z plane at $x = 0$ with ϕ being the azimuthal angle. Simulations for both $l = 1$ [Fig. 7.2(a)] and $l = -1$ beams were conducted.

The simulated sound speed profile is $c = c_0(1 - \alpha z)$, giving a refractive index,

$$n = \frac{c_0}{c} = \frac{1}{1 - \alpha z}, \tag{7.1}$$

and a reference wavenumber $k_0 = \omega/c_0 = 2\pi/\lambda_0$. The medium inhomogeneity is first set as $\alpha = 0.2\ \mathrm{m}^{-1}$ and the reference wavelength is $\lambda_0 = 1$ m. The refractive index profile n is illustrated

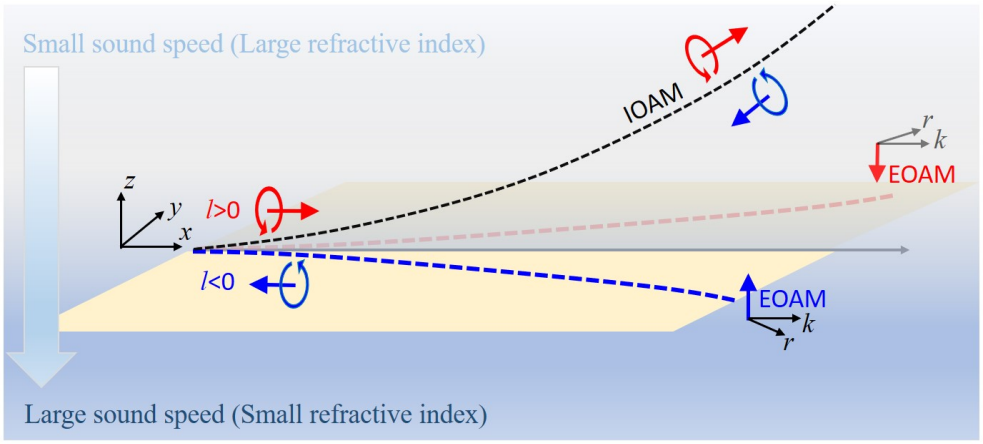

Figure 7.1: Illustration of orbital angular momentum Hall effect in an acoustic vortex beam propagating in an inhomogeneous (gradient) medium, manifesting a helicity-dependent transverse shift in the homogeneous y direction, accompanied by a coupling between extrinsic and intrinsic orbital angular momenta (denoted by EOAM and IOAM) and conservation of the total angular momentum along the gradient z direction.

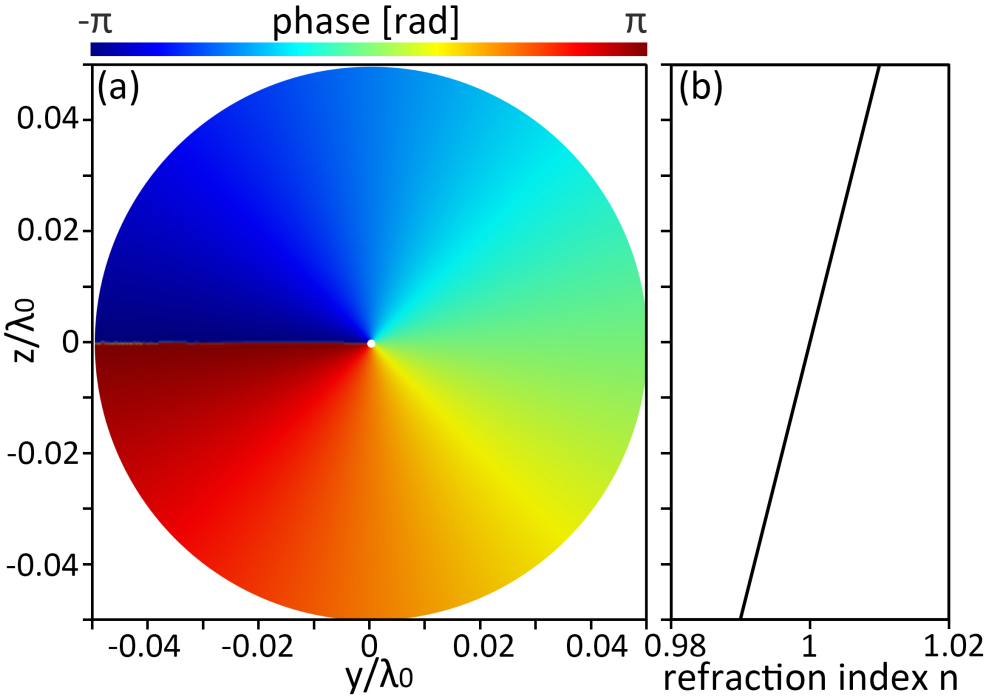

Figure 7.2: (a) Simulated phase in the y-z cross section at the initial source plane for a helicity $l = 1$. (b) One example of refraction index profile used in the simulation [see Eq. (7.1)].

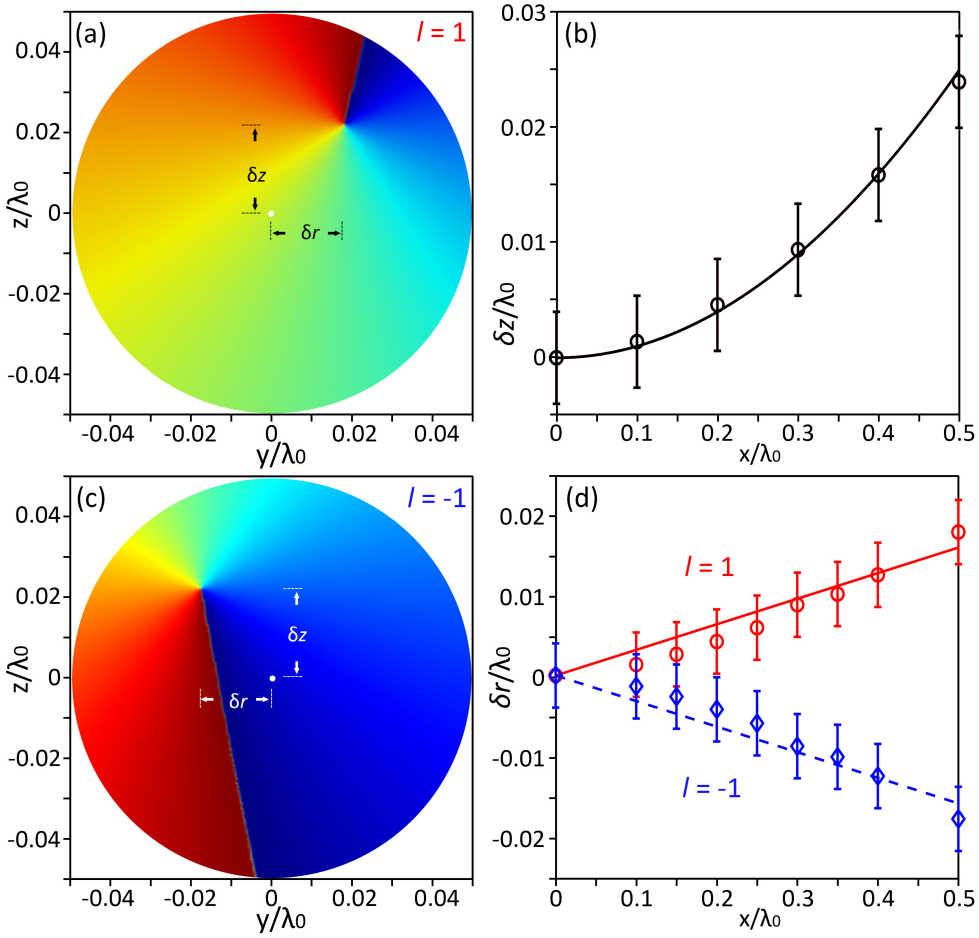

Figure 7.3: (a) Simulated phase in the y-z cross section at $x = 0.5\lambda_0$ for the vortex beam with topological charge of $l = 1$, showing the transverse Hall shift δr in the homogeneous y direction in addition to the refractive deflection δz in the inhomogeneous z direction, where the corresponding shifts of the beam center (singular point) related to the original beam axis (x axis) are marked. (b) Vertical bending due to the refraction (black circles) with the solid line from a quadratic fit. (c) Same as (a) but for a beam of $l = -1$, where the transverse shift is of the same magnitude as (a) but in an opposite direction. (d) Transverse shift δr increases with the propagation distance x for both $l = \pm 1$ beams determined from the simulations and corresponding linear fits. For the vertical bending in (b), $l = \pm 1$ follow the same line. Error bars are determined from mesh size.

in Fig. 7.2(b). To study the dynamical change of the behaviors due to the variation of parameters, a series of simulations were conducted by varying the speed gradient α from 0.03 to 0.3 (fix the reference wavenumber $k_0 = 2\pi$ m^{-1}) and by varying the reference wavenumber $k_0 = 2\pi/\lambda_0$ from 5.0 to 8.3 (fix the gradient as $\alpha = 0.1$ m^{-1}).

To precisely determine location of the beam center during the propagation, the mesh size near the singular core (a cylinder with radius of $0.05\lambda_0$) is reduced to be as small as 1/200 of the reference wavelength. This mesh size is around an order lower than the shift of the singular point location to be found in our simulations. The regions outside the cylinder have a regular mesh size of 1/16 wavelength.

Figure 7.3(a) shows the phase in y-z cross section at the propagation distance, $x = 0.5\lambda_0$, for the vortex beam with topological charges of $l = 1$. The beam bends to the direction of sound speed descent ($+z$ direction) due to the refraction [Fig. 7.3(b)], which was recently simulated in Fan et al.[155] whereas here it is found that the beam center also has a transverse shift in the homogeneous y direction. This transverse shift was not found in the prior simulations where the mesh size varied from 1/10 to 1/5 wavelength and the mesh near the core was not fine enough to identify the transverse shift.

The vortex beam with topological charge of $l = -1$ propagating in the same medium is shown in Fig. 7.3(c). It is found that the transverse shift is of the same magnitude as the case of $l = 1$ but in the *opposite* direction, revealing a dependence on the beam's helicity. The transverse shifts as a function of the propagation distance are further examined for both $l = \pm 1$ [Fig. 7.3(d)]. It is found that the transverse shift is linearly scaling with respect to the propagation distance while the shift direction depends on the sign of the helicity l.

Variations of the transverse shift with the medium inhomogeneity α and reference wavenumber k_0 are shown in Fig. 7.4(a) and (b). The results show that, given a specific distance x, the transverse shift increases with speed gradient [Fig. 7.4(a)] and decreases with the wavenumber [Fig. 7.4(b)]. The dependence is determined by a linear fit. In addition, it is found that the slope $\delta r/x$ of the fit is linearly scaling with α and with $1/k_0$ [Fig. 7.4(c)], namely, $\delta r/x \propto \alpha/k_0$.

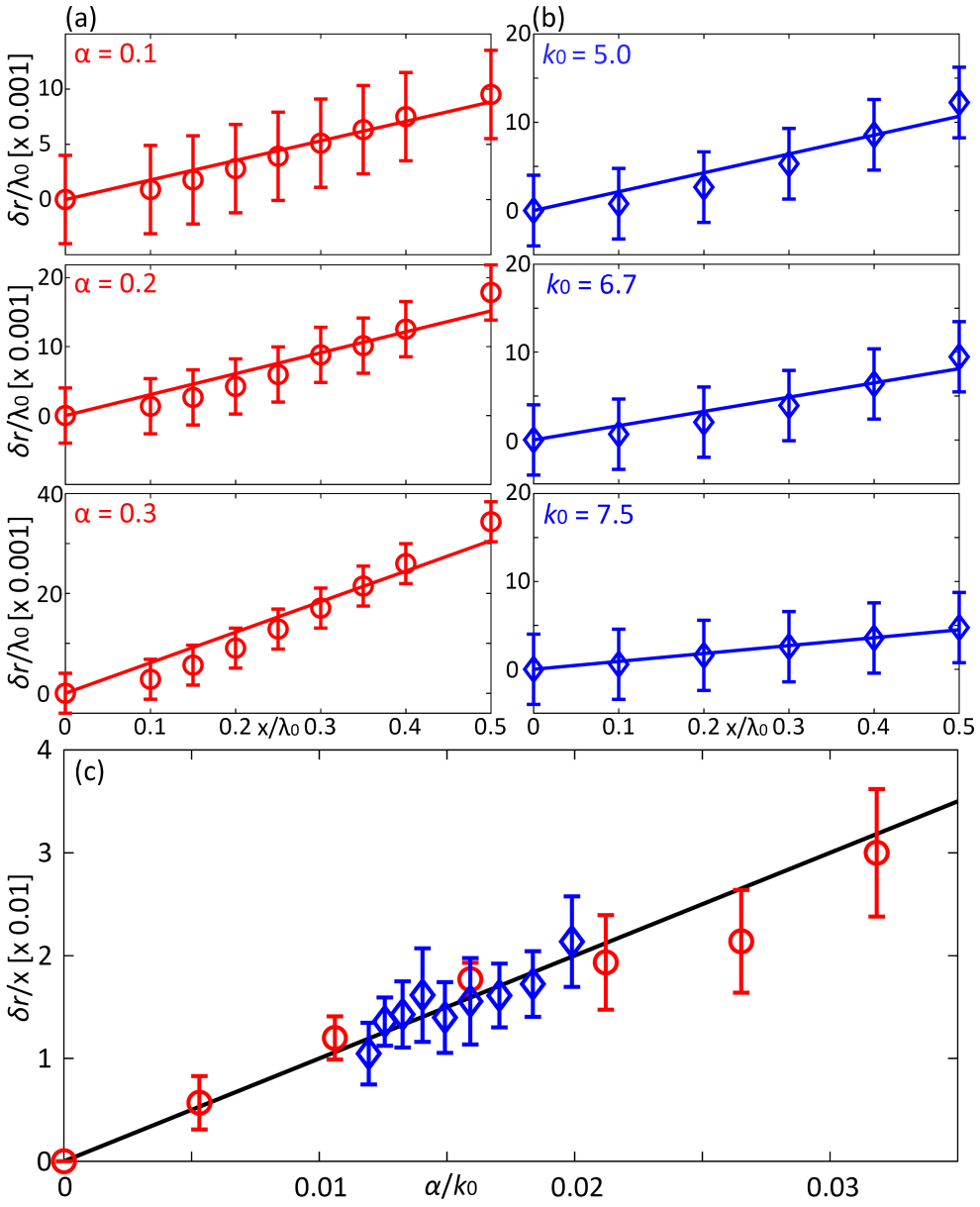

Figure 7.4: Numerically simulated (circles/diamonds) versus linear fitted (solid lines) transverse Hall shifts as a function of propagation distance when (a) varying the gradient α (keeping $k_0 = 2\pi$ m^{-1}) and (b) varying the wavenumber k_0 (keeping $\alpha = 0.1$ m^{-1}). (c) Derivative of transverse shift with respect to the propagation distance, i.e. $\delta r/x$, as a function of α/k_0, determined from the simulated results in (a) and (b) [denoted by red circles and blue diamonds, respectively] and in comparison with theoretical prediction (solid line) from Eq. (7.6), i.e. $\delta r/x \propto \alpha/k_0$. Error bars in (a) and (b) come from the mesh size, and in (c) come from the 95% confidence bounds of the linear fits.

7.2 Modeling of orbital Hall effect in Acoustics

The helicity-dependent transverse shift observed here can be regarded as acoustic orbital Hall effect, which is the acoustic counterpart of the orbital Hall effect in optics. This effect is revealed by considering the equations of motion for the beam center in a smoothly inhomogeneous medium, which have been derived in the context of optics via the variation principle on the effective Lagrangian in the presence of Berry curvature.[94,96,97,100,101,105,106,156] Similar to the optical counterpart, the equations of wave vector $\mathbf{k}$ and the displacement $\mathbf{r}$ of acoustic vortex beam center as propagating in a smoothly inhomogeneous medium are,

$$\dot{\mathbf{k}} = k\nabla \ln n, \text{ and } \dot{\mathbf{r}} = \frac{\mathbf{k}}{k} - l\frac{\mathbf{k}\times\dot{\mathbf{k}}}{k^3}, \tag{7.2}$$

where dot donates the derivative with respect to s, which is the length of a curved trajectory followed by the beam center. In the first equation, the gradient of the logarithm refractive index ($\nabla \ln n$), representing the inhomogeneity of the medium, plays the role of an external force leading to the refraction of the beam in the inhomogenous direction. The first term in the second equation in (7.2) characterizes the ray followed by the beam center without considering the carried orbital angular momentum.

The second term in the second equation in (7.2), proportional to the orbital angular momentum l, is an addition to the vortex beam, where the cross product of $\mathbf{k}$ and $\dot{\mathbf{k}}$ leads to a transverse shift that is normal to both wave vector of the beam center and medium inhomogeneity. This phenomenon is hence regarded as the Hall effect since the shift is perpendicular to the "force" i.e. the medium inhomogeneity, in an analogy to angular momentum Hall effect in optics.[101] The direction of the shift depends on the sign of the topological charge l (Fig. 7.1). In this case, the sound speed gradient leads $\dot{\mathbf{k}}$ to be in z direction and $\mathbf{k}$ is predominantly along x direction. It follows from Eq. (7.2) that the shift is in y direction, consistent with our numerical simulations [Fig. 7.3(a) and (c)] and consequently validating our observation of acoustic orbital Hall effect for the first time after decades of studies of acoustic vortex beams and orbital angular momentum.

The dependence of the shift on the parameters is now analyzed. Specifically, a linearly stratified media, whose refraction index as a function of depth was given in Eq. (7.1), is considered. In this case, the first equation in (7.2) can be simplified as

$$\dot{\mathbf{k}} = k\frac{\alpha}{n}\widehat{\mathbf{z}} = k_0\frac{\alpha}{n^2}\hat{\mathbf{z}}. \tag{7.3}$$

Since the change of the wave vector is only along z direction, the expression of wave vector $\mathbf{k}$ can be assigned as $\mathbf{k} = k_x\widehat{\mathbf{x}} + k_z\widehat{\mathbf{z}}$, where k_x and k_z are to be determined. Substituting $\mathbf{k}$ into Eq. (7.3), one has (i) the wave number in x direction is constant and equal to initial wave number, i.e. $k_x = k_0 = \omega/c_0$, and (ii) the wave number in z direction can be solved from $dk_z = k_0(\alpha/n^2)ds$. Within the range considered in this paper, $\delta n \ll 1$ and zero order approximation is applied, i.e. $ds \approx dx$ and $n \approx 1$. Hence, the wave vector is

$$\mathbf{k} \approx k_0[\widehat{\mathbf{x}} + \alpha x\widehat{\mathbf{z}}]. \tag{7.4}$$

The transverse shift in the homogeneous y direction by the Hall effect can be solved by a contour integral along the ray of zero approximation,

$$\delta\mathbf{r} = -l\int_C(\mathbf{k}\times d\mathbf{k})/k^3. \tag{7.5}$$

Combining Eqs. (7.3), (7.4) and (7.5), one obtains,

$$\delta\mathbf{r} = \frac{l}{k_0}\alpha x\widehat{\mathbf{y}}, \tag{7.6}$$

which predicts that the shift is proportional to (i) the helicity l, (ii) a typical magnitude of k_0^{-1}, (iii) medium inhomogeneity gradient α, and (iv) the propagation distance x. This theoretical prediction is compared with the numerical simulations in Fig. 7.4(c), where the derivative of transverse shift with respect to propagation distance, $\delta r/x$, as a function of α/k_0 is presented. The results confirm

the agreement between the numerical observation and theoretical prediction from Eq. (7.6), i.e., $\delta r/x = \alpha/k_0$ with the helicity $l = 1$.

7.3 Orbit-orbit Interactions and Angular Momentum Conservation

The orbital angular momentum Hall shift represents the interactions between the intrinsic and extrinsic orbital angular momentum with respect to the origin at $(x, y, z) = 0$. The total angular momentum as a sum of extrinsic and intrinsic orbital angular momentum (with a proper normalization) can be expressed as:

$$\mathbf{J} = \mathbf{r} \times \mathbf{k} + l\mathbf{k}/k. \tag{7.7}$$

The bending of the beam along the gradient direction by refraction immediately generates an extrinsic orbital angular momentum in the transverse direction (first term), which is $-(1/2)\alpha k_0 x^2 \hat{\mathbf{y}}$ in our case, following from the wave vector $\mathbf{k}$ in Eq. (7.4) and the position vector $\mathbf{r}$ is solved from the second equation in Eq. (7.2) in the zero approximation ($\dot{\mathbf{r}} = \mathbf{k}/k$) to be

$$\mathbf{r} \approx x\widehat{\mathbf{x}} + \frac{1}{2}\alpha x^2 \widehat{\mathbf{z}}, \tag{7.8}$$

where the second term is the deflection in the inhomogeneous direction by refraction and is quadratic in propagation distance x at the leading order [see Fig. 7.3(b)].

The wave refraction generates a variation of the intrinsic orbital angular momentum along the gradient direction [second term in Eq. (7.7)]. The variation is compensated by a variation of the extrinsic orbital angular momentum [first term in Eq. (7.7)] contributing from the transverse shift of the Hall effect, exhibiting the interactions of intrinsic and extrinsic angular momentum to guarantee the conservation of the total angular momentum. In our case, the variation in the z-component of the intrinsic angular momentum is

$$\text{Intrinsic OAM variation} = \alpha l x \widehat{\mathbf{z}}, \tag{7.9}$$

and the extrinsic orbital angular momentum produced by the transverse shift is

$$\text{Extrinsic OAM variation} = -\alpha l x \widehat{\mathbf{z}}, \tag{7.10}$$

manifesting the conservation of the total angular momentum along the gradient direction and the interactions between intrinsic and extrinsic orbital angular momentum for acoustic vortex beams in a smoothly inhomogeneous media.

Here the ray theory determines the motion of the beam center but not the field's intensity distribution. The intensity profile can be distorted to be transversely asymmetric with respect to the beam center. Such asymmetry was observed in our last simulation in Fan et al.[155] where it was explained by a superposition of vortex rotation and vertical refraction. The asymmetry depends on specific beams and is also affected by other factors like diffraction.[117,118] The asymmetry also perturbs the orbital angular momentum. The further exploration of the asymmetry and its perturbation on orbital angular momentum is beyond the scope of this present analysis.

7.4 Remarks

To conclude, the orbital angular momentum Hall effect in acoustics was observed for the first time via numerical simulations. A vortex beam carrying the orbital angular momentum propagating in a smoothly inhomogeneous medium is considered. The transverse shifts related to orbital angular momentum Hall effect are predicted, observed, and then characterized by a ray formula in the inhomogeneity approximation. These results demonstrate that the orbital angular momentum of sound can also have interesting topological properties that may find applications in the manipulation of sound signals. This work opens up the fundamental study of acoustic Hall effect and orbital angular momentum in an inhomogeneous medium. Note the shift is proportional to sound speed, but the sound speed is several orders smaller than for optical waves.

The formula [Eq. (7.6)] assumes the range of refractive index variation is small. This is the case for many stratified media, for example, the inhomogeneity of sound speed in ocean and

atmospheric environments. To observe the transverse shift in a medium with a small gradient, the sound would need to propagate a long distance. Take the ocean as an example, where the range of sound speed variation is about 50 m/s over 4 km depth and the averaged sound speed is about 1,500 m/s, implying an estimated shift of about only 2 cm for a $l = 1$ sound vortex beam of 1 kHz traveling a distance (horizontal range) of 10 km. The shift increases if the frequency is lowered.

The experimental observation of the acoustic orbital angular momentum Hall effect requires the generation of inhomogeneity of the medium, which can be created by salinity or thermal gradient. A precise acoustic measurement to detect the slight shift of sound field would be needed. A relatively large gradient and low frequency enhances the shift. A higher-order vortex beam could also amplify the shift. For example, one can create a sound speed gradient about 0.377 m/s per mm ($\alpha \approx 0.24$ m^{-1}) in a laboratory tank by salinity.[86] Low frequency underwater transducers can be used to generate sound waves in a frequency range of 1 kHz to 10 kHz, and the corresponding range of the transverse shifts from 60 mm to 6 mm could be measured at the distance of 1 m away from the transducer. In addition, a transverse shift can be specifically observed in the beam transmitted through the sharp interface of two media and with the aid of metasurfaces with a phase gradient,[157] which will be discussed in the next chapters. A large phase gradient generated by metasurfaces[158] amplifies the shift and also allows for the observation of the shifts in air. More complex beams and media/structures could also be considered.

CHAPTER 8

ACOUSTIC IMBERT-FEDOROV EFFECT

In this chapter, a special example of the acoustic orbital Hall effect, the acoustic Imbert-Fedorov effect, which occurs on a sharp boundary between two media, is investigated. Similar to the optical counterpart,[159] theoretical expressions of the transverse shifts in acoustics are derived based on the conservation of the tangent component of linear momentum and the conservation of the normal component of angular momentum. The results are then validated by numerical simulations. Possible experiments to observe the acoustic Imbert-Fedorov effect are also suggested.

8.1 Theoretical prediction

The acoustic Imbert-Fedorov effect involves the reflection and transmission of vortex beams between two media. An incident acoustic vortex beam, carrying intrinsic orbital angular momentum l, propagates in the x-z plane with an angle θ to the z-axis, and the beam is partially reflected and transmitted at the interface $z = 0$ between two non-absorbing media (Fig. 8.1). The wavevectors of all the three beams, which are attached to the Z^a-axes in their local coordinate frames (X^a, y, Z^a) with $a = i, r, t$, lie in the same plane:

$$\mathbf{k}^a = k^a \mathbf{e}_Z^a = k^a(\sin\theta^a, 0, \cos\theta^a). \tag{8.1}$$

Three wavenumbers follow $k^r = k^i \equiv k$ and $k^t = nk$ where n is the relative refractive index of the second medium, i.e., $n = c_1/c_2$ with c_1 and c_2 being the sound speeds of the first and the second media. Based on the Snell's law or the conservation of tangent component of linear momentum,

the incident, reflected and refracted angles can be obtained:

$$\theta^i = \theta, \theta^r = \pi - \theta, \theta^t = \sin^{-1}(n^{-1}\sin\theta) \equiv \theta'. \tag{8.2}$$

Hence, the beam shift can be obtained from the conservation of the normal component of the angular momentum, which means the changes in the z-component of the intrinsic orbital angular momentum must be compensated by the changes of the extrinsic orbital angular momentum caused by the transverse shifts in y-direction. As a result, the shifts for the reflected and transmitted beams $\delta_y^{r,t}$ can be obtained [159,160]

$$\delta_y^r = \frac{L_z^{int,r} - L_z^{int,i}}{k\sin\theta}, \delta_y^t = \frac{L_z^{int,t} - L_z^{int,i}}{k\sin\theta}, \tag{8.3}$$

in which the wavenumber along x direction, $k\sin\theta$, is used so as to obtain a change of the extrinsic orbital angular momentum in z direction. The intrinsic orbital angular momentum from the incident, reflected and transmitted beams are $\mathbf{L}^{int,a} = D^a l \mathbf{e}_Z^a$ with $a = i, r, t$, and the additional factors D^a [160] are

$$D^i = 1,\ D^r = -1,\ \text{and}\ D^t = (\cos\theta/\cos\theta' + \cos\theta'/\cos\theta)/2. \tag{8.4}$$

Again, $\mathbf{e}_Z^a = (\sin\theta^a, 0, \cos\theta^a)$; see Eq. (8.1).

Then the z components of the intrinsic orbital angular momenta can be written explicitly,

$$\begin{aligned} L_z^{int,i} &= l\cos\theta^i = l\cos\theta \\ L_z^{int,r} &= -l\cos\theta^r = -l\cos(\pi - \theta) \\ L_z^{int,t} &= \frac{l}{2}\left(\frac{\cos\theta}{\cos\theta'} + \frac{\cos\theta'}{\cos\theta}\right)\cos\theta^t = \frac{l}{2}\left(\frac{\cos\theta}{\cos\theta'} + \frac{\cos\theta'}{\cos\theta}\right)\cos\theta'. \end{aligned} \tag{8.5}$$

By substituting Eq. (8.5) into Eq. (8.3), one can obtain the transverse shifts in y-direction for both

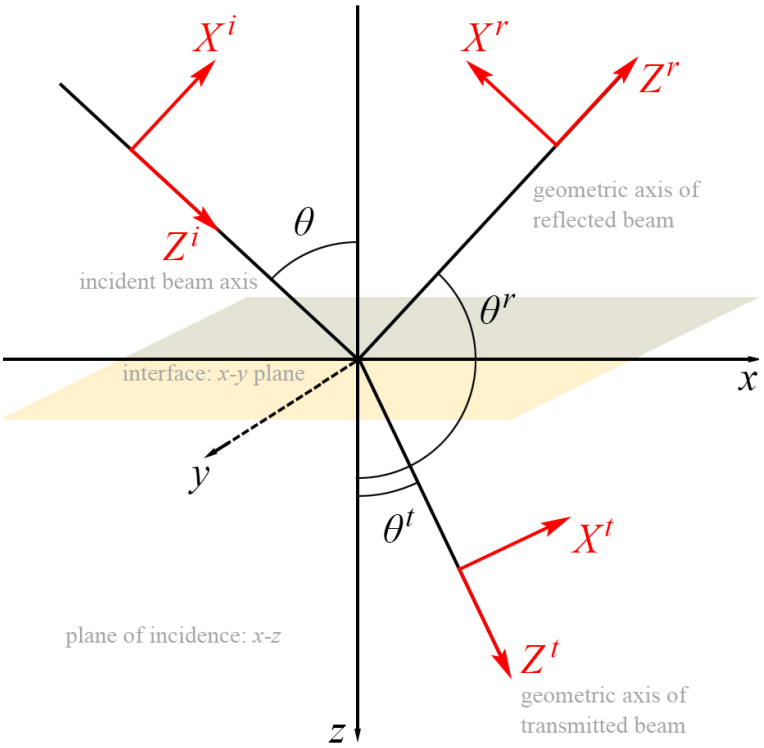

Figure 8.1: Illustration of acoustic reflection and transmission of a paraxial beam at the plane interface between two media, i.e., x-y plane at $z = 0$. The plane of incidence is x-z plane at $y = 0$. The beam coordinate frames (X^a, y, Z^a) with $a = i, r, t$ are attached to the incident, reflected and transmitted beams, respectively. Incident, reflected, and transmitted angles θ^a are marked, and they follows the relations: $\theta^i = \theta$, $\theta^r = \pi - \theta$, and $\theta^t = \sin^{-1}(n^{-1}\sin\theta) \equiv \theta'$ with n being the relative refractive index.

reflected and transmitted beams:[159]

$$\delta_y^r = \frac{(-l)(-\cos\theta) - l\cos\theta}{k\sin\theta} = 0, \tag{8.6}$$

$$\delta_y^t = \frac{\frac{l}{2}\left(\frac{\cos\theta}{\cos\theta'} + \frac{\cos\theta'}{\cos\theta}\right)\cos\theta' - l\cos\theta}{k\sin\theta} = \frac{l}{2k}\tan\theta(1 - n^{-2}). \tag{8.7}$$

The results show that the shift of the reflected beam δ_y^r is zero, independent of the properties of both the incident beam and the interface. However, the shift for the transmitted beam δ_y^t relies on: (i) the intrinsic orbital angular momentum, l; (ii) the incident wavevector $\mathbf{k}$, which gives the wavenumber k and the incident angle θ; and (iii) the relative refractive index n, which characterizes the property of the interface between two media. See relevant studies in optics.[116–118,157]

8.2 Numerical observation

To observe the Imbert-Fedorov effect, an vortex beam with topological charge of $l = 1$ interacting with a sharp boundary between two media is simulated [Fig. 8.2(a)], where the center of the incident vortex beam is in x-z plane at $y = 0$ with the phase profile of the source shown in Fig. 8.2(b). The phase at the transmitted plane is shown in Fig. 8.2(c) where the acoustic Imbert-Fedorov shift is marked between two white dashed lines, i.e., $\delta y = 0.14 \pm 0.05$ mm in this case. Here, the sound speed of the two media are $c_1 = 1500$ m/s and $c_2 = 750$ m/s, giving the relative refractive index $n = c_1/c_2 = 2$. The frequency used is $f = 0.9$ MHz and the incident angle is $\theta = 60°$. Hence, the acoustic IF shift observed here is about 0.1 wavelength, which agrees with the prediction in Eq. (8.7).

To further investigate the dependence of the transverse IF shift on physical parameters, simulations with different incident angles ($\theta = 30°$ to $60°$ with an interval of $5°$) have been conducted with the results shown in Fig. 8.3. The simulated results (red circles) follow along the theoretical prediction (black solid line), i.e., $\delta_y \propto \tan\theta$, with the error bar from the maximum mesh size in the simulations.

Simulations with different incident sound frequencies ($f = 100$ kHz to 1 MHz with an interval of 100 kHz) have also been conducted with the results shown in Fig. 8.4. The simulated results (red circles) follow along the theoretical prediction (black solid line), i.e., $\delta_y \propto 1/k$, with the error bar from the maximum mesh size in the simulations, i.e., $\pm 0.03\lambda$.

8.3 Suggested experiments on the interface of two media

Experimental observation of the transverse shift by acoustic orbital angular momentum Hall effect or acoustic Imbert-Fedorov effect can be suggested based on the formula Eq. (8.7),

$$\delta_y^t = \frac{l}{4\pi} \cdot \lambda \cdot \tan\theta \cdot (1 - n^{-2}), \tag{8.8}$$

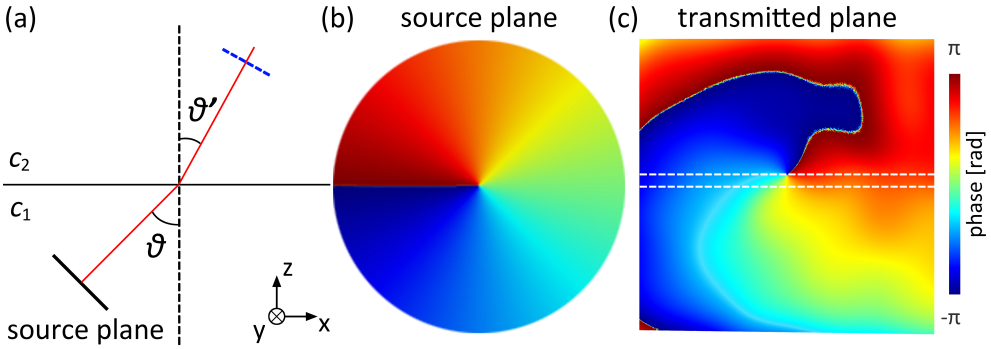

Figure 8.2: (a) Illustration of acoustic vortex beam transmitted from a sharp boundary between two media. Red lines come from the Snell's law with θ and θ' being the incident and refractive angle. (b) Phase in the initial vortex source plane [black solid line in (a)]. (c) Phase in the transmitted plane [blue dashed line in (a)] with the Imbert-Fedorov shift in y direction marked between two white dashed lines.

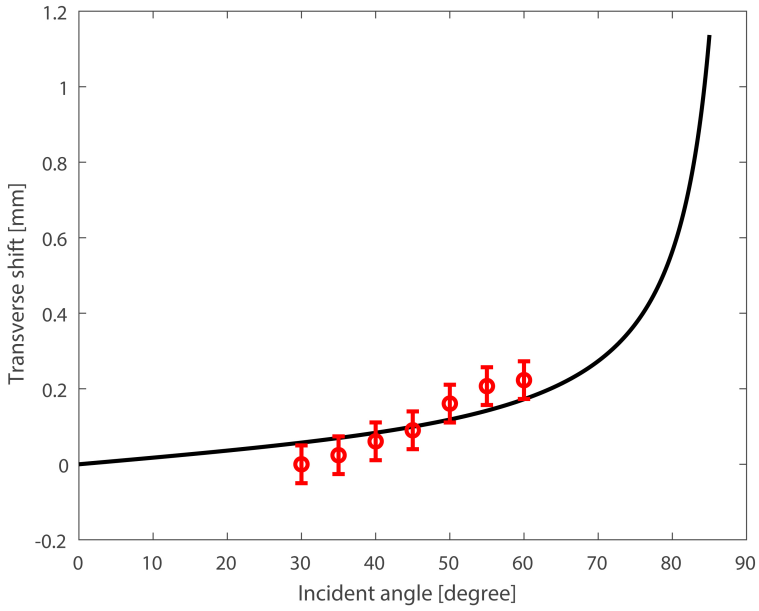

Figure 8.3: Simulated transverse I-F shifts (red circles) as a function of the incident angle with the theoretical prediction (black line) used for comparison. Error bars come from the maximum mesh size used in the simulation, i.e., 0.05 mm.

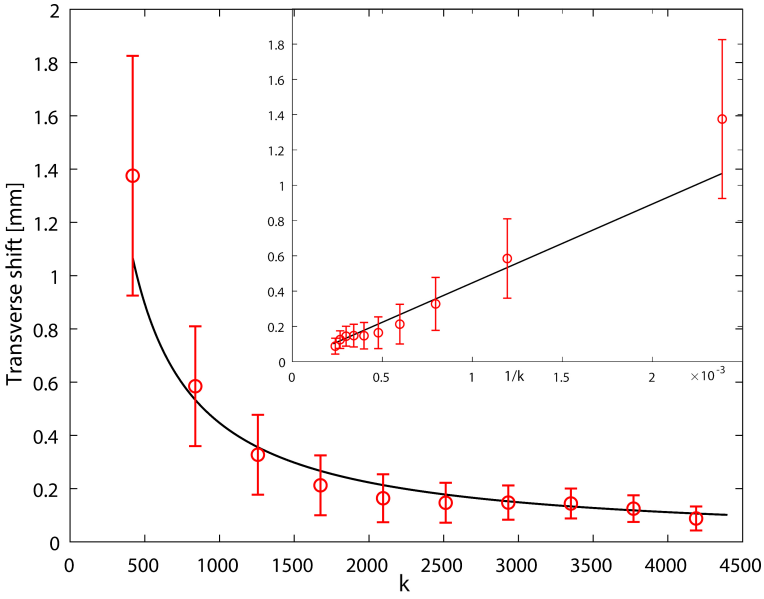

Figure 8.4: Simulated transverse I-F shifts (red circles) as a function of the wavenumber k with the theoretical prediction (black line) used for comparison. Error bars come from the maximum mesh size used in the simulation, i.e., $\pm 0.03\lambda$. Inset: simulated transverse shift versus $1/k$ for comparison.

where one can see that the shift is proportional to the wavelength λ and the tangent of the incidence angle $\tan\theta$. Large wavelength (low-frequency) and large incidence angle would help to enhance the shift for experimental observation. In addition, the relative refractive index n needs to be carefully chosen to make sure: (i) the refractive index is large enough to enhance the shift ($\delta_y^t \propto 1 - n^{-2}$), and (ii) the acoustic impedance difference between two media is not too large (n is not too large), so that enough sound energy can be transmitted through the interface.

Some examples of fluids for experimental observation are suggested as shown in Fig. 8.5, where one layer of the medium can be chosen from Table 8.1 and the other layer of the medium is water. From the results, the transverse shift can reach 0.8λ when the incidence angle is $\theta = 85°$, which means if a 100 kHz transducer is used in the experiment, the transverse shift can reach 12 mm, which is measurable. If the frequency is further reduced to 10 kHz, then the transverse shift can be 10 times larger or 120 mm, since the shift is proportional to the wavelength.

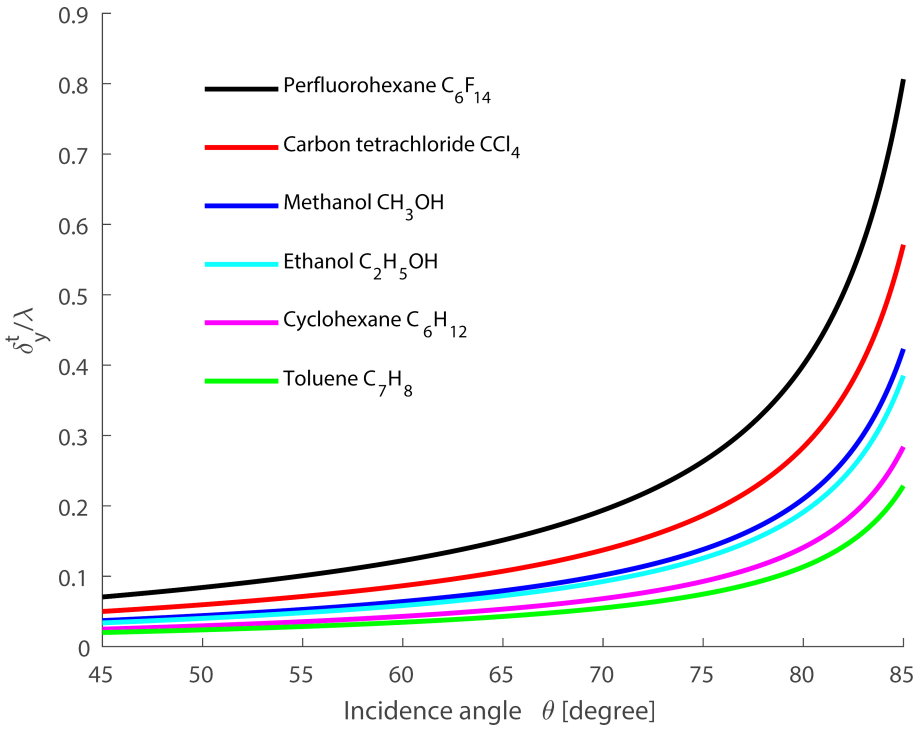

Figure 8.5: Suggested experiments. Transverse I-F shifts as a function of the incidence angle θ for some suggested fluids for experiments. Corresponding acoustic properties of the fluids are shown in Table 8.1.

Materials	Mass density ρ [kg/m^3]	Sound speed c [m/s]	Refractive index n	Transverse shift δ_y^t/λ [$\theta = 85°$]
C_6F_{14}	1691	505	2.97	0.806
CCl_4	1587	915	1.64	0.571
CH_3OH	792	1097	1.37	0.423
C_2H_5OH	789	1139	1.32	0.385
C_6H_{12}	779	1244	1.21	0.284
C_7H_8	867	1298	1.16	0.229
H_2O	1000	1500	1	0

Table 8.1: Acoustic properties of fluids at atmospheric pressure and temperature T = 300 K.

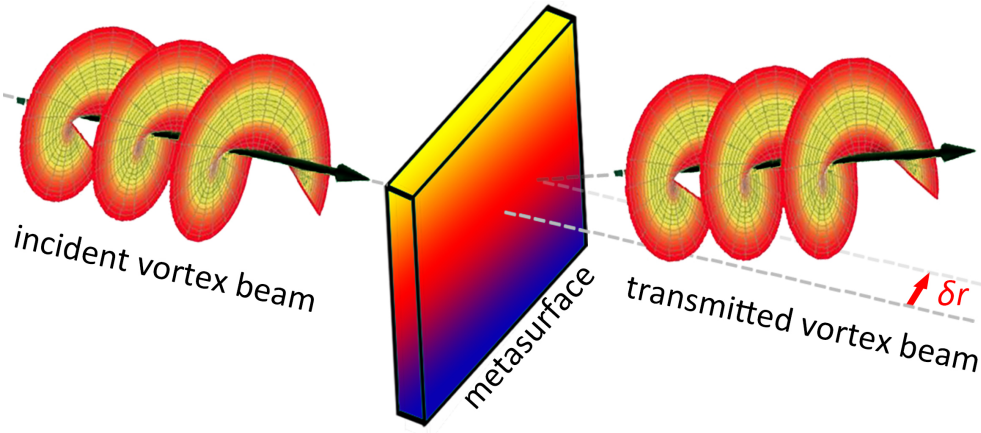

Figure 8.6: Illustration of experimental observation of orbital Hall effect with the aid of acoustic metasurface with a phase gradient. Transverse shift δr can be observed from the transmitted field.

8.4 Suggested experiments using meta-materials

The last section discussed the acoustic Imbert-Fedorov effects on a sharp boundary between two media, which is due to the evolution of the wavevector across the boundary. This sharp boundary can be also constructed using acoustic metamaterials/metasurfaces with a phase gradient since metamaterials/metasurfaces, a type of artificial structures, provide extreme flexibility in reshaping the transmitted wavefront in a passive manner by providing additional momentum in the transverse direction.[161] With the aid of the desired phase profiles, the transmitted fields can be tailored in an controllable manner.

Here, an experiment with the aid of acoustic meta-materials is proposed, which will guide the observation of the acoustic Hall shift in future. The acoustic Hall effect or acoustic IF shift can be measured when the incident vortex beam is transmitted from an acoustic meta-surface with a phase gradient (Fig. 8.6). Specifically, the transverse shift can be determined by comparing the scanned fields with and without the metasurface. The incident vortex beams can be generated, for example, by four individual sources with same amplitude and linearly increasing phases $(0, \pi/2, \pi, 3\pi/2)$,[61] or via a hydrophone array to get a better structured wavefront.

The structure used here is the resonance-based meta-surface [Fig. 8.7(a)].[158,161,162] The structure is composed of individual elements with each having a hybrid structure formed by

coupling a straight tube with a series connection of four cavities acting as acoustic resonators [see Fig. 8.7(b) for the cross section of one element]. The element can effectively adjust the phase of the transmitted waves by varying the geometry parameter d/D while keeping a high transmission efficiency larger than 80% for airborne sound [see simulated results in Fig. 8.7(c)]. Each individual element can be treated as a point source with particular phase and amplitude, together with the phase at the entrance of the unit being accounted. As an example, 16 elements with different d/D are selected to eventually build a metasurface with a phase gradient of 0.8π per wavelength; see Fig. 8.7(d). The metasurface can be printed using 3D printing technology.

According to Fermat's principle or the Generalized Snell's Law,[163] the wavefront of acoustic beams can be reshaped by manipulating the propagation phases. In this case, the direction of "anomalous" refraction related to the normal incident vortex beam follows

$$\theta_t = \sin^{-1}(\frac{1}{k}\frac{d\phi}{d\tau}), \tag{8.9}$$

where θ_t is the refraction angle to the normal line, k is the wavenumber in the transmitted domain, and $d\phi/d\tau$ represents the phase gradient, which is 0.8π per wavelength in this case, giving the theoretical refraction angle $\theta_t = 23.6°$.

The simulated phase on the x-z cross section at $y = 0$ using the proposed structure is shown in Fig. 8.7(e), where the wavevector of the transmitted beam follows along the black arrow with an angle θ_t to the normal line (dashed black line). The refraction angle simulated here agrees exactly with the predicted value by the Generalized Snell's Law, 23.6°. Then the acoustic orbital Hall effect can be observed by measuring the transverse shift of the vortex center in y direction, which is about 0.1λ as shown between the two black dashed lines in Fig. 8.7(f).

8.5 Remarks

The experiment proposed here allows for the observation of the transverse shifts in air via acoustic metasurfaces with a phase gradient. The resonance-based structure[158] used here has

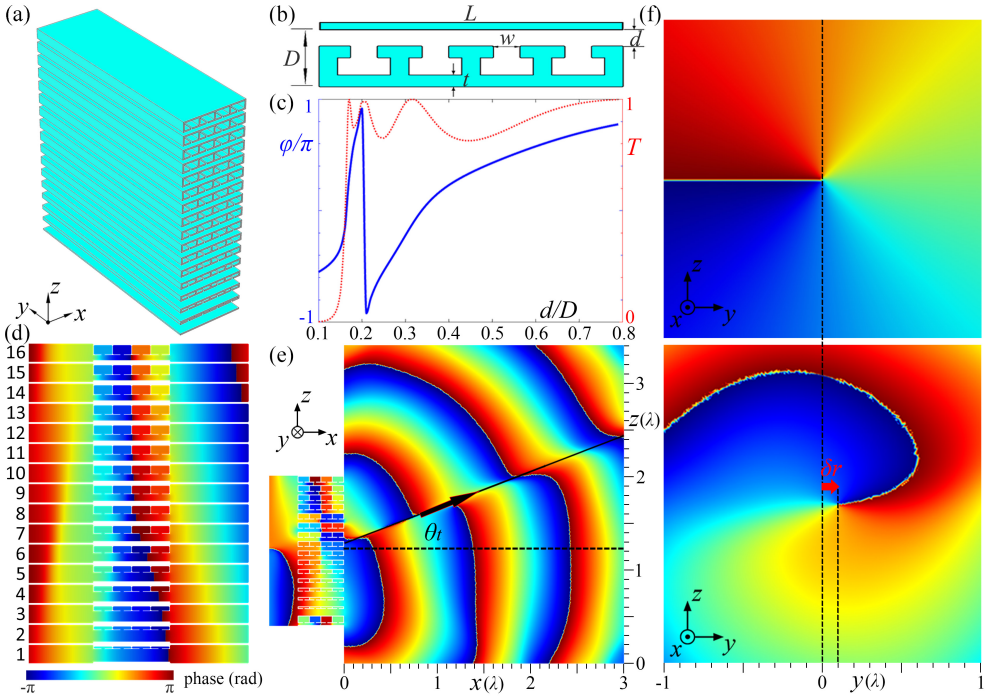

Figure 8.7: (a) Illustration of the metasurface with the cross section of one element shown in (b). Parameters are chosen as $L = 0.5\lambda$, $D = 0.1\lambda$, $t = 0.01\lambda$, and $w = 0.015\lambda$ with λ being the wavelength. (c) Simulated phase shift covering the range of 2π can be effectively adjusted by varying the parameter d/D with the transmission efficiency larger than 80% ($T = |p_t/p_i|$ with p_i and p_t being the incident and transmitted field). (d) Simulated phases of the 16 elements used in the simulation, giving the phase gradient of 0.8π per wavelength. (e) Phase on the x-z cross section at $y = 0$, where the wavevector of the transmitted beam follows along the black arrow with an angle θ_t to the normal line (dashed black line). (f) Phase profile of the incident wave (top panel) and the transmitted wave (bottom panel) on the y-z cross section, where the transverse shift is marked between the two black dashed lines.

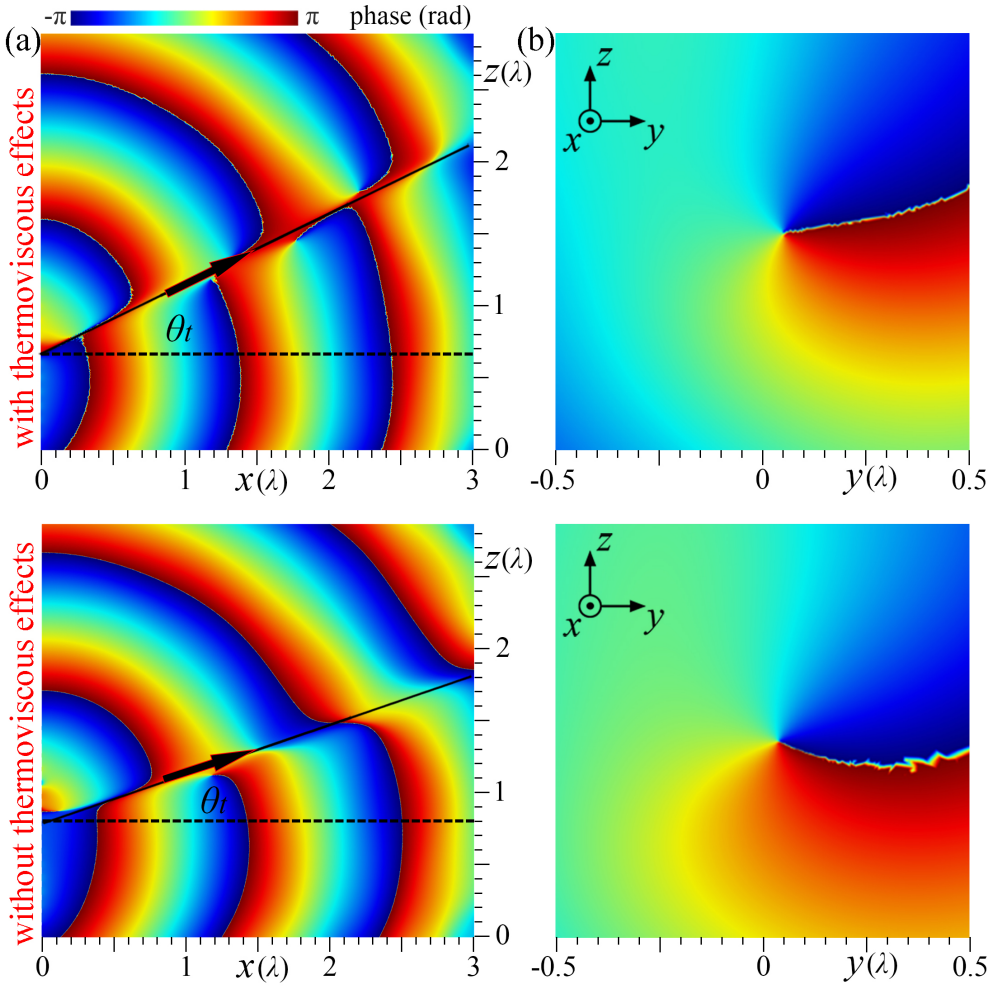

Figure 8.8: (a) Phases on the x-z cross section at $y = 0$. (b) Phase profile of the transmitted wave on the y-z cross section. Top panels: with thermoviscous effects; bottom panels: without thermoviscous effects.

the advantage of a planar interface, a full 2π phase shift, a well-matched impedance, and the subwavelength spatial resolution, which are preferred for most applications. A large phase gradient helps to amplify the transverse shift. More complex beams, media, and structures could also be considered. The oblique incidence and the thermoviscous effect would need to be considered for the transition through the structure.

Normal and oblique incidence of incident waves on this structure was studied by Li et al.[161] where the transmission/reflection spectra and the refracted pressure fields were systematically studied. It was found by Li et al.[161] that aforementioned properties of this structure are still valid under oblique incidence within a certain range of incident angles. Specifically, fully controlled phase shift and high transmission can be achieved for oblique incidence with an incident angle smaller than 56° if the threshold of the transmission amplitude of each element is set to 0.9, and the angle increases to 75° if the threshold is set as -3 dB, which means that 50% of the incident power penetrates the element [see Fig.4 in Li et al.[161] for more details].

Thermoviscous effects on sound transmission through this resonance-based metasurface were studied by Jiang et al.[162] where both wall friction and the thermoviscous diffusivity in the structure were taken into account. The results reveal that the dissipation has a weak influence on phases even when there is a large loss. Specifically, the dissipation reduces the transmission by 28% when the thermoviscous boundary layer thickness is only around 2.3% of the slit width.

Since the structure is valid within a certain range of incident angles,[161] the structure could be used to generate a phase gradient for an incident vortex wave, where a small paraxiality parameter is preferred. Although the thermoviscous effect has little influence on the generation of the phase gradient,[162] which is the key to observe the orbital Hall effect, a simulation including the thermoviscous effects was also conducted; see Fig. 8.8. From the results, one can find that the propagating direction of the transmitted waves was changed due to different transmissions from different unit elements of the structure caused by the thermoviscous effects [see Fig. 8.8(a)], however, the transverse shift does not changed much when comparing the results w/o the thermoviscous effects [see Fig. 8.8(b)]. In the simulations, thermoviscous acoustic module was employed in the

metasurface region [for both the Helmholtz resonators and the straight tube; see Fig. 8.7(b)] to consider both the viscous friction and thermal diffusivity. No slip and isothermal conditions are used on the solid boundaries. Pressure acoustic module was used for the incident and transmitted areas, where the losses are ignored since there is no wall friction outside the metasurface. The working frequency is 3430 Hz. The values of d/D for the simulation are 0.269, 0.282, 0.294, 0.306, 0.319, 0.333, 0.35, 0.36, 0.383, 0.413, 0.451, 0.496, 0.547, 0.604, 0.669, 0.749 [Fig. 8.7(b)].

8.6 Conclusion

Vortex beams with a twisted wavefront possess both intrinsic and extrinsic orbital angular momenta. In this chapter, an analogous orbital Hall effect in acoustics, i.e. acoustic Imbert-Fedorov effect, is modelled using a vortex beam propagating through a sharp interface between two media. Similar to optical counterparts,[159] the transverse shifts related to the acoustic Imbert-Fedorov effect are predicted and characterized by a ray formula based on the conservation of orbital angular momentum. Possible experimental observations of the acoustic phenomenon are suggested via either two media or with the aid of acoustic metasurfaces. The results have possible applications in the manipulations of sound signals. This work introduces the fundamental study of the acoustic Imbert-Fedorov effect between two media and relevant applications in future.

CHAPTER 9

SUMMARY AND CONCLUSION

In summary, this dissertation studied the acoustic Bessel and vortex beams including the radiation force generated by these beams as well as the propagation of vortex beams in inhomogeneous media. A new type of acoustic tweezers, which can not only trap particles in the transverse direction but also pull the particles towards the source in the axial direction, has been proved to be possible. In addition, some unusual and interesting phenomena have been found when simulating the propagation of acoustic vortex beams in inhomogeneous media such as the asymmetry of pressure amplitude and transverse energy flux, the migration of singular points, the reversal and separation of transverse energy flux, and the acoustic orbital Hall effect.

Specifically, for the first part of the acoustic radiation force, the acoustic trapping force generated by acoustic Bessel waves has been analyzed based on the Gorkov potential, the partial wave expansion method and the Born approximation method. The Gorkov potential can be used for the analysis of acoustic radiation forces on small objects with the advantage of simplicity and efficiency compared with the partial wave expansion method. However, for large objects, the Gorkov potential will usually lose its prediction capability, and the full solution from the partial wave expansion method has to be used instead. When the material contrast between objects and background media is small, and the incident wave has a standing wave component as well, the Born approximation method can be used to predict the trapping force on objects whose characteristic length is smaller than a wavelength. With the aid of the Born approximation, a *modified* version of the Gorkov potential could also be used for the analysis of acoustic trapping forces on large objects with small material contrasts compared with background media. In the modified Gorkov potential, the exact location of the objects needs to be replaced with the characteristic length of the object

for the force prediction. In addition, the acoustic pulling force based on the phase shift approach was also analyzed. This phase shift approach can simplify the computation, and also allows one to engineer object and beam parameters to design desired axially pulling forces. The effects of some realistic factors such as gravity, buoyancy, and the acoustic streaming were also studied. Generally speaking, the force due to the acoustic streaming is dominant compared with the acoustic radiation force for small objects, and the acoustic radiation force becomes dominant as objects become larger unless the radiation force is close to near 0. The work here is useful for the further study of acoustic radiation force as well as the design of acoustic tweezers.

For the second part of the propagation of vortex beams in inhomogeneous media, a series of unstable and dynamic behaviors were numerically observed. These behaviors include bending, stretching, distorting and untwisting of the vortex beam, migration of singular points, and reversal of energy flux and angular momentum. Then the acoustic orbital Hall effect in a continuously stratified medium as well as on a sharp boundary between two media was studied. Possible experimental observations of the acoustic orbital Hall effect were suggested in a water tank using salinity gradient, through an interface between two media, and in air with the aid of a gradient metasurface. This work provides a basis for the fundamental study of acoustic vortices in inhomogeneous media or complex media. It would be also interesting to study acoustic tractor beams in inhomogenous media, for example, in a stratified medium, where the particle might be pulled towards the source along a curved path.

LIST OF REFERENCES

Bibliography

1. Armen P. Sarvazyan, Oleg V. Rudenko, and Wesley L. Nyborg. Biomedical applications of radiation force of ultrasound: historical roots and physical basis. *Ultrasound in Medicine & Biology*, 36(9):1379–1394, 2010.

2. J. Wu. Acoustical tweezers. *J. Acoust. Soc. Am.*, 89(5):2140–2143, 1991. doi: 10.1121/1.400907. URL https://doi.org/10.1121/1.400907.

3. C. R. P. Courtney, B. W. Drinkwater, C. E. M. Demore, S. Cochran, A. Grinenko, and P. D. Wilcox. Dexterous manipulation of microparticles using Bessel-function acoustic pressure fields. *Appl. Phys. Lett.*, 102(12):123508, 2013. doi: 10.1063/1.4798584. URL https://doi.org/10.1063/1.4798584.

4. A. Marzo, S. A. Seah, B. W. Drinkwater, D. R. Sahoo, B. Long, and S. Subramanian. Holographic acoustic elements for manipulation of levitated objects. *Nature communications*, 6:8661, Oct. 2015. doi: 10.1038/ncomms9661. URL http://dx.doi.org/10.1038/ncomms9661.

5. K. Melde, A. G. Mark, T. Qiu, and P. Fischer. Holograms for acoustics. *Nature*, 537:518–522, Sep 2016. doi: 10.1038/nature19755. URL https://www.nature.com/articles/nature19755.

6. Takahi Hasegawa, Yasutaka Hino, Akio Annou, Hideki Noda, Masahiko Kato, and Naoki Inoue. Acoustic radiation pressure acting on spherical and cylindrical shells. *The Journal of the Acoustical Society of America*, 93(1):154–161, 1993. doi: 10.1121/1.405653. URL https://doi.org/10.1121/1.405653.

7. Michael Faraday. XVII. On a peculiar class of acoustical figures; and on certain forms assumed by groups of particles upon vibrating elastic surfaces. *Philosophical transactions of the Royal Society of London*, (121):299–340, 1831.

8. Johannes Kepler. 1619. de cometis libelli tres.

9. August Kundt and O. Lehmann. Ueber longitudinale schwingungen und klangfiguren in cylindrischen flüssigkeitssäulen. *Annalen der Physik*, 229(9):1–12, 1874.

10. Lord Rayleigh. XXXIV. On the pressure of vibrations. *The London, Edinburgh, and Dublin Philosophical Magazine and Journal of Science*, 3(15):338–346, 1902.

11. G. Hertz and H. Mende. Der schallstrahlungsdruck in flüssigkeiten. *Zeitschrift für Physik*, 114(5-6):354–367, 1939.

12. L. P. Gor'kov. On the forces acting on a small particle in an acoustical field in an ideal fluid. *Sov. Phys. Dokl.*, 6:773 – 775, 1962.

13. P. L. Marston. Axial radiation force of a Bessel beam on a sphere and direction reversal of the force. *J. Acoust. Soc. Am*, 120(6):3518–3524, 2006. doi: 10.1121/1.2361185. URL https://doi.org/10.1121/1.2361185.

14. L. K. Zhang and P. L. Marston. Geometrical interpretation of negative radiation forces of acoustical Bessel beams on spheres. *Phys. Rev. E*, 84:035601, Sep 2011. doi: 10.1103/PhysRevE.84.035601. URL https://link.aps.org/doi/10.1103/PhysRevE.84.035601.

15. L. K. Zhang and P. L. Marston. Axial radiation force exerted by general non-diffracting beams. *J. Acoust. Soc. Am.*, 131(4):EL329–EL335, 2012. doi: 10.1121/1.3693387. URL https://doi.org/10.1121/1.3693387.

16. S. Xu, C. Qiu, and Z. Liu. Transversally stable acoustic pulling force produced by two crossed plane waves. *Europhys. Lett.*, 99:44003, 2012.

17. C. E. M. Démoré, P. M. Dahl, Z. Yang, P. Glynne-Jones, A. Melzer, S. Cochran, M. P. MacDonald, and G. C. Spalding. Acoustic tractor beam. *Phys. Rev. Lett.*, 112:174302, Apr 2014. doi: 10.1103/PhysRevLett.112.174302. URL https://link.aps.org/doi/10.1103/PhysRevLett.112.174302.

18. L. K. Zhang. Reversals of orbital angular momentum transfer and radiation torque. *Phys. Rev. Applied*, 10:034039, Sep 2018. doi: 10.1103/PhysRevApplied.10.034039. URL https://link.aps.org/doi/10.1103/PhysRevApplied.10.034039.

19. X. D. Fan and L. K. Zhang. Trapping force of acoustical bessel beams on a sphere and stable tractor beams. *Phys. Rev. Applied*, 11:014055, Jan 2019. doi: 10.1103/PhysRevApplied.11.014055.

20. Max Born. Quantenmechanik der stoßvorgänge. *Zeitschrift für Physik*, 38(11):803–827, 1926.

21. Ratan K. Saha and Subodh K. Sharma. Validity of a modified born approximation for a pulsed plane wave in acoustic scattering problems. *Physics in Medicine and Biology*, 50(12):2823–2836, jun 2005. doi: 10.1088/0031-9155/50/12/007. URL https://doi.org/10.1088/0031-9155/50/12/007.

22. Peizhen Zhang, Shuozhong Wang, Runtian Wang, Yunfei Chen, and Luxian Wang. Modification to first-order born approximation for improved prediction of scattered sound from weakly scattering objects. *Chinese Journal of Acoustics*, 33(3):228–238, 2014.

23. Peizhen Zhang and Shuozhong Wang. Fast prediction of scattered sound field based on fourier diffraction theory under second-order born approximation. *Acoustical Physics*, 60(4): 379–386, 2014.

24. Roger Narayan et al. *Biomedical materials*, volume 1. Springer, 2009.

25. Costantino Creton and Matteo Ciccotti. Fracture and adhesion of soft materials: a review. *Reports on Progress in Physics*, 79(4):046601, mar 2016. doi: 10.1088/0034-4885/79/4/046601. URL https://doi.org/10.1088/0034-4885/79/4/046601.

26. Thomas S. Jerome, Yurii A. Ilinskii, Evgenia A. Zabolotskaya, and Mark F. Hamilton. Born approximation of acoustic radiation force and torque on soft objects of arbitrary shape. *J. Acoust. Soc. Am*, 145(3):1715–1715, 2019.

27. Thomas S. Jerome and Mark F. Hamilton. Extensions of the born approximation for acoustic radiation force and torque to inhomogeneous objects and progressive spherical waves. *Proc. 23rd Int. Cong. Acoust.*, pages 7565–7571, 2019.

28. P. J. Westervelt. The theory of steady forces caused by sound waves. *J. Acoust. Soc. Am*, 23: 312 – 315, 1951.

29. P. J. Westervelt. Acoustical radiation pressure. *J. Acoust. Soc. Am*, 29:26 – 29, 1957.

30. H. Olsen, H. Wergeland, and P. J. Westervelt. Acoustic radiation force. *J. Acoust. Soc. Am.*, 30(7):633–634, 1958.

31. H. Olsen, W. Romberg, and H. Wergeland. Radiation force on bodies in a sound field. *J. Acoust. Soc. Am.*, 30(1):69–76, 1958.

32. T. Hasegawa. Comparison of two solutions for acoustic radiation pressure on a sphere. *J. Acoust. Soc. Am.*, 61(6):1445–1448, 1977.

33. T. Hasegawa and Y. Watanabe. Acoustic radiation pressure on an absorbing sphere. *J. Acoust. Soc. Am.*, 63(6):1733–1737, 1978.

34. X. Chen and R. E. Apfel. Radiation force on a spherical object in an axisymmetric wave field and its application to the calibration of highrequency transducers. *J. Acoust. Soc. Am.*, 99(2): 713–724, 1996.

35. Philip L. Marston. Acoustic beam scattering and excitation of sphere resonance: Bessel beam example. *The Journal of the Acoustical Society of America*, 122(1):247–252, 2007. doi: 10.1121/1.2735810. URL https://doi.org/10.1121/1.2735810.

36. P. L. Marston. Acoustic beam scattering and excitation of sphere resonance: Bessel beam example. *J. Acoust. Soc. Am*, 122(6):247, 2007. doi: 10.1121/1.2735810. URL https://doi.org/10.1121/1.2735810.

37. D. B. Thiessen, L. K. Zhang, and P. L. Marston. Radiation force on spheres in helicoidal bessel beams modeled using finite elements. *J. Acoust. Soc. Am.*, 125(1):2552, 2009. doi: http://doi.org/10.1121/1.4783653.

38. L. K. Zhang and P. L. Marston. Optical theorem for acoustic non-diffracting beams and application to radiation force and torque. *Biomed. Opt. Express*, 4(9):1610–1617, 2013. doi: 10.1364/BOE.4.001610. URL http://www.osapublishing.org/boe/abstract.cfm?URI=boe-4-9-1610.

39. G. T. Silva. An expression for the radiation force exerted by an acoustic beam with arbitrary wavefront (L). *J. Acoust. Soc. Am*, 130(6):3541–3544, 2011. doi: 10.1121/1.3652894. URL https://doi.org/10.1121/1.3652894.

40. D. Baresch, J. L. Thomas, and R. Marchiano. Three-dimensional acoustic radiation force on an arbitrarily located elastic sphere. *J. Acoust. Soc. Am.*, 133(1):25–36, 2013. doi: http://dx.doi.org/10.1121/1.4770256.

41. O. A. Sapozhnikov and M. R. Bailey. Radiation force of an arbitrary acoustic beam on an elastic sphere in a fluid. *J. Acoust. Soc. Am.*, 133(2):661–676, 2013. doi: 10.1121/1.4773924. URL https://doi.org/10.1121/1.4773924.

42. L. K. Zhang and P. L. Marston. Acoustic radiation force expressed using complex phase shifts and momentum-transfer cross sections. *J. Acoust. Soc. Am*, 140(2):EL178–EL183, 2016. doi: 10.1121/1.4959966. URL https://doi.org/10.1121/1.4959966.

43. P. L. Marston and L. K. Zhang. Relationship of scattering phase shifts to special radiation force conditions for spheres in axisymmetric wave-fields. *J. Acoust. Soc. Am*, 141(5):3042–3049, 2017. doi: 10.1121/1.4982203. URL https://doi.org/10.1121/1.4982203.

44. P. L. Marston. Phase-shift expansions for approximate radiation forces on solid spheres in inviscid-acoustic standing waves. *J. Acoust. Soc. Am*, 142(2):3358, 2017. doi: 10.1121/1.5016031.

45. P. L. Marston. Phase-shift derivation of expansions for material and frequency dependence of progressive-wave radiation forces and backscattering by spheres. *J. Acoust. Soc. Am*, 145 (2):EL39, 2019. doi: 10.1121/1.5087646.

46. Zhixiong Gong, Philip L. Marston, and Wei Li. t-matrix evaluation of three-dimensional acoustic radiation forces on nonspherical objects in bessel beams with arbitrary order and location. *Phys. Rev. E*, 99:063004, Jun 2019. doi: 10.1103/PhysRevE.99.063004. URL https://link.aps.org/doi/10.1103/PhysRevE.99.063004.

47. Long Meng, Feiyan Cai, Fei Li, Wei Zhou, Lili Niu, and Hairong Zheng. Acoustic tweezers. *Journal of Physics D: Applied Physics*, 52(27):273001, 2019.

48. M. Baudoin and J.-L. Thomas. Acoustic tweezers for particle and fluid micromanipulation. *Annual Review of Fluid Mechanics*, 52(1):205–234, 2020. doi: 10.1146/annurev-fluid-010719-060154. URL https://doi.org/10.1146/annurev-fluid-010719-060154.

49. D. Zhao, J.-L. Thomas, and R. Marchiano. Generation of spherical vortex beams to trap large particles for enhanced axial force. *Ultrasonics*, 111:106296, 2021. ISSN 0041-624X. doi: https://doi.org/10.1016/j.ultras.2020.106296. URL https://www.sciencedirect.com/science/article/pii/S0041624X2030233X.

50. L. K. Zhang. From acoustic radiation pressure to three-dimensional acoustic radiation forces. *J. Acoust. Soc. Am.*, 144(1):443–447, 2018. doi: 10.1121/1.5047441. URL https://doi.org/10.1121/1.5047441.

51. P. L. Marston and L. K. Zhang. Unphysical consequences of negative absorbed power in linear passive scattering: Implications for radiation force and torque. *J. Acoust. Soc. Am*, 139 (5):3139, 2016. doi: 10.1121/1.4954044. URL https://doi.org/10.1121/1.4954044.

52. Majid Rajabi and Alireza Mojahed. Acoustic manipulation of active spherical carriers: Generation of negative radiation force. *Annals of Physics*, 372:182–200, 2016. ISSN 0003-4916. doi: https://doi.org/10.1016/j.aop.2016.05.003. URL https://www.sciencedirect.com/science/article/pii/S0003491616300501.

53. Hai-Qun Yu, Jie Yao, Da-Jian Wu, Xue-Wei Wu, and Xiao-Jun Liu. Negative acoustic radiation force induced on an elastic sphere by laser irradiation. *Phys. Rev. E*, 98:053105, Nov 2018. doi: 10.1103/PhysRevE.98.053105. URL https://link.aps.org/doi/10.1103/PhysRevE.98.053105.

54. Yan Meng, Xiao Li, Zixian Liang, Jack Ng, and Jensen Li. Acoustic pulling with a single incident plane wave. *Phys. Rev. Applied*, 14: 014089, Jul 2020. doi: 10.1103/PhysRevApplied.14.014089. URL https://link.aps.org/doi/10.1103/PhysRevApplied.14.014089.

55. P. A. Martin. On in-out splitting of incident fields and the far-field behaviour of herglotz wavefunctions. *Mathematical Methods in the Applied Sciences*, 41(8):2961–2970, 2018.

56. P. A. Martin. Quadratic quantities in acoustics: Scattering cross-section and radiation force. *Wave Motion*, 86:63–78, 2019. ISSN 0165-2125.

57. L. Rayleigh. On the circulation of air observed in kundt's tubes, and on some allied acoustical problems. *Proceedings of the Royal Society of London*, 175:1–21, 1883.

58. H. Schlichting. Berechnung ebener periodischer grenzschichtströmungen (calculation of plane periodic boundary layer streaming). *Physikalische Zeitschrift*, 33:327–335, 1932.

59. Carl Eckart. Vortices and Streams Caused by Sound Waves. *Physical Review*, 73(1):68–76, January 1948. doi: 10.1103/PhysRev.73.68.

60. Said Boluriaan and Philip J. Morris. Acoustic streaming: From rayleigh to today. *International Journal of Aeroacoustics*, 2(3):255–292, 2003. doi: 10.1260/147547203322986142. URL https://doi.org/10.1260/147547203322986142.

61. B. T. Hefner and P. L. Marston. An acoustical helicoidal wave transducer with applications for the alignment of ultrasonic and underwater systems. *J. Acoust. Soc. Am.*, 106:3313, 1999. doi: 10.1121/1.428184.

62. L. K. Zhang and P. L. Marston. Angular momentum flux of nonparaxial acoustic vortex beams and torques on axisymmetric objects. *Phys. Rev. E*, 84:065601, Dec 2011. doi: 10.1103/PhysRevE.84.065601. URL https://link.aps.org/doi/10.1103/PhysRevE.84.065601.

63. L. K. Zhang and P. L. Marston. Acoustic radiation torque on small objects in viscous fluids and connection with viscous dissipation. *J. Acoust. Soc. Am*, 136(6):2917–2921, 2014. doi: 10.1121/1.4900441. URL https://doi.org/10.1121/1.4900441.

64. R. Marchiano and J. L. Thomas. Synthesis and analysis of linear and nonlinear acoustical vortices. *Phys. Rev. E*, 71:066616, 2005. doi: 10.1103/PhysRevE.71.066616.

65. R. Marchiano, F. Coulouvrat, L. Ganjehi, and J. L. Thomas. Numerical investigation of the properties of nonlinear acoustical vortices through weakly heterogeneous media. *Phys. Rev. E*, 77(01):016605, 2008. doi: 10.1103/PhysRevE.77.016605.

66. X. Jiang, Y. Li, B. Liang, J.-c. Cheng, and L. Zhang. Convert acoustic resonances to orbital angular momentum. *Phys. Rev. Lett.*, 117: 034301, Jul 2016. doi: 10.1103/PhysRevLett.117.034301. URL https://link.aps.org/doi/10.1103/PhysRevLett.117.034301.

67. K. D. Skeldon, C. Wilson, M. Edgar, and M. J. Padgett. An acoustic spanner and its associated rotational doppler shift. *New J. Phys.*, 10:013018, 2008. doi: 10.1088/1367-2630/10/1/013018.

68. K. Volke-Sepúlveda, A. O. Santillán, and R. R. Boullosa. Transfer of angular momentum to matter from acoustical vortices in free space. *Phys. Rev. Lett.*, 100:024302, Jan 2008. doi: 10.1103/PhysRevLett.100.024302. URL https://link.aps.org/doi/10.1103/PhysRevLett.100.024302.

69. C. E. M. Demore, Z. Yang, A. Volovick, S. Cochran, M. P. MacDonald, and G. C. Spalding. Mechanical evidence of the orbital angular momentum to energy ratio of vortex beams. *Phys. Rev. Lett.*, 108:194301, May 2012. doi: 10.1103/PhysRevLett.108.194301. URL https://link.aps.org/doi/10.1103/PhysRevLett.108.194301.

70. A. Anhäuser, R. Wunenburger, and E. Brasselet. Acoustic rotational manipulation using orbital angular momentum transfer. *Phys. Rev. Lett.*, 109:034301, Jul 2012. doi: 10.1103/PhysRevLett.109.034301. URL https://link.aps.org/doi/10.1103/PhysRevLett.109.034301.

71. Z. Hong, J. Zhang, and B. W. Drinkwater. Observation of orbital angular momentum transfer from Bessel-shaped acoustic vortices to diphasic liquid-microparticle mixtures. *Phys. Rev. Lett.*, 114:214301, May 2015. doi: 10.1103/PhysRevLett.114.214301. URL https://link.aps.org/doi/10.1103/PhysRevLett.114.214301.

72. T. Wang, M. Ke, W. Li, Q. Yang, C. Qiu, and Z. Liu. Particle manipulation with acoustic vortex beam induced by a brass plate with spiral shape structure. *Applied Physics Letters*, 109(12): 123506, 2016. doi: 10.1063/1.4963185. URL https://doi.org/10.1063/1.4963185.

73. A. Marzo, M. Caleap, and B. W. Drinkwater. Acoustic virtual vortices with tunable orbital angular momentum for trapping of mie particles. *Phys. Rev. Lett.*, 120:044301, Jan 2018. doi: 10.1103/PhysRevLett.120.044301. URL https://link.aps.org/doi/10.1103/PhysRevLett.120.044301.

74. D. Baresch, J. L. Thomas, and R. Marchiano. Orbital angular momentum transfer to stably trapped elastic particles in acoustical vortex beams. *Phys. Rev. Lett.*, 121:074301, August 2018. doi: 10.1103/PhysRevLett.121.074301. URL https://link.aps.org/doi/10.1103/PhysRevLett.121.074301.

75. E. Toninelli, M. A. Cox, G. M. Gibson, S. D. Brown, M. P. Edgar, A. Forbes, and M. J. Padgett. A compact acoustic spanner to rotate macroscopic objects. *Sci. Rep.*, 9:6757, 2019. doi: 10.1038/s41598-019-43046-4.

76. S. T. Kang and C. K. Yeh. Potential-well model in acoustic tweezers. *IEEE Transactions on Ultrasonics, Ferroelectrics, and Frequency Control*, 57(6):1451–1459, June 2010. ISSN 0885-3010. doi: 10.1109/TUFFC.2010.1564.

77. D. Baresch, J.-L. Thomas, and R. Marchiano. Observation of a single-beam gradient force acoustical trap for elastic particles: Acoustical tweezers. *Phys. Rev. Lett.*, 116:024301, Jan 2016. doi: 10.1103/PhysRevLett.116.024301. URL https://link.aps.org/doi/10.1103/PhysRevLett.116.024301.

78. M. Baudoin, J. C. Gerbedoen, A. Riaud, O. B. Matar, N. Smagin, and J. L. Thomas. Folding a focalized acoustical vortex on a flat holographic transducer: Miniaturized selective acoustical tweezers. *Science Advances*, 5(4), 2019. doi: 10.1126/sciadv.aav1967.

79. B. T. Hefner and B. R. Dzikowicz. A spiral wave front beacon for underwater navigation: Basic concept and modeling. *J. Acoust. Soc. Am.*, 129:3630, 2011.

80. C. Z. Shi, M. Dubois, Y. Wang, and X. Zhang. High-speed acoustic communication by multiplexing orbital angular momentum. *PNAS*, 114:7250, 2017. doi: 10.1073/pnas.1704450114.

81. X. Jiang, B. Liang, J. C. Cheng, and C. W. Qiu. Twisted acoustics: Metasurface-enabled multiplexing and demultiplexing. *Advanced Materials*, 30:1800257, 2018. doi: 10.1002/adma.201800257.

82. T. Brunet, J. L. Thomas, and R. Marchiano. Transverse shift of helical beams and subdiffraction imaging. *Phys. Rev. Lett.*, 105:034301, 2010. doi: 10.1103/PhysRevLett.105.034301.

83. A. D. Maxwell, M. Bailey, B. W. Cunitz, M. Terzi, A. Nikolaeva, S. Tsysar, and O. A. Sapozhnikov. Vortex beams and radiation torque for kidney stone management. *J. Acoust. Soc. Am*, 139:2040, 2016. doi: 10.1121/1.4950032.

84. V. P. Aksenov, V. V. Kolosov, V. A. Tartakovskii, and B. V. Fortes. Optical vortices in inhomogeneous media. *Atmos. Oceanic Opt.*, 12(10):912, 1999.

85. W. H. Munk. Sound channel in an exponentially stratified ocean, with application to sofar. *J. Acoust. Soc. Am.*, 55(2):220–226, 1974. doi: https://doi.org/10.1121/1.1914492.

86. L. K. Zhang and H. L. Swinney. Sound propagation in a continuously stratified laboratory ocean model. *J. Acoust. Soc. Am*, 141(5):3186, 2017. doi: 10.1121/1.4983123. URL https://doi.org/10.1121/1.4983123.

87. M. S. Soldevilla, M. F. McKenna, S. M. Wiggins, R. E. Shadwick, T. W. Cranford, and J. A. Hildebrand. Cuvier's beaked whale (ziphius cavirostris) head tissues: physical properties and ct imaging. *Journal of Experimental Biology*, 208:2319–2332, 2005. doi: https://doi.org/10.1242/jeb.01624.

88. J. Gu and Y. Jing. Numerical modeling of ultrasound propagation in weakly heterogeneous media using a mixed domain method. *IEEE Transactions on Biomedical Engineering*, 65(7): 1258 – 1267, 2018. doi: https://doi.org/10.1109/TUFFC.2018.2828316.

89. Scott Schoen and Costas D Arvanitis. Fast acoustic aberration correction with the angular spectrum approach. *arXiv: Signal Processing*, 2019.

90. E. H. Hall. On a new action of the magnet on electric currents. *American Journal of Mathematics*, 2(3):287–292, 1879.

91. Klaus V. Klitzing. The quantized Hall effect. *Physica B+C*, 126(1):242 – 249, 1984. ISSN 0378-4363. doi: https://doi.org/10.1016/0378-4363(84)90170-0. URL http://www.sciencedirect.com/science/article/pii/0378436384901700.

92. D. C. Tsui, H. L. Stormer, and A. C. Gossard. Two-dimensional magnetotransport in the extreme quantum limit. *Phys. Rev. Lett.*, 48:1559–1562, May 1982. doi: 10.1103/PhysRevLett.48.1559. URL https://link.aps.org/doi/10.1103/PhysRevLett.48.1559.

93. K. S. Novoselov, Zhigang Jiang, Yuanbo Zhang, S. V. Morozov, H. L. Stormer, U. Zeitler, J. C. Maan, G. S. Boebinger, Philip Kim, and A. K. Geim. Room-temperature quantum Hall effect in graphene. *Science*, 315(5817):1379–1379, 2007.

94. Konstantin Yu. Bliokh. Geometrical optics of beams with vortices: Berry phase and orbital angular momentum Hall effect. *Phys. Rev. Lett.*, 97:043901, Jul 2006. doi: 10.1103/PhysRevLett.97.043901. URL https://link.aps.org/doi/10.1103/PhysRevLett.97.043901.

95. Konstantin Y. Bliokh. Geometrodynamics of polarized light: Berry phase and spin Hall effect in a gradient-index medium. *Journal of Optics*, 11(9):094009, 2009.

96. Shoucheng Zhang, Shuichi Murakami, Naoto Nagaosa, Xiaoliang Qi, and Yongshi Wu. The spin Hall effect. *Science*, 301:1348, 2003.

97. Jairo Sinova, Dimitrie Culcer, Qian Niu, NA Sinitsyn, T Jungwirth, and Allan H MacDonald. Universal intrinsic spin Hall effect. *Phys. Rev. Lett.*, 92(12):126603, 2004.

98. O. Costa de Beauregard and C. Imbert. Quantized longitudinal and transverse shifts associated with total internal reflection. *Phys. Rev. Lett.*, 28:1211–1213, May 1972. doi: 10.1103/PhysRevLett.28.1211. URL https://link.aps.org/doi/10.1103/PhysRevLett.28.1211.

99. Fedor I. Fedorov. To the theory of total reflection. *Journal of Optics*, 15(1):014002, jan 2013. doi: 10.1088/2040-8978/15/1/014002.

100. S. I. Vinitskiĭ, V. L. Derbov, Vladimir M. Dubovik, B. L. Markovski, and Yu P. Stepanovskiĭ. Topological phases in quantum mechanics and polarization optics. *Soviet Physics Uspekhi*, 33(6):403–428, jun 1990. doi: 10.1070/pu1990v033n06abeh002598. URL https://doi.org/10.1070.

101. Masaru Onoda, Shuichi Murakami, and Naoto Nagaosa. Hall effect of light. *Phys. Rev. Lett.*, 93(8):083901, 2004.

102. Konstantin Yu. Bliokh and Yury P. Bliokh. Conservation of angular momentum, transverse shift, and spin Hall effect in reflection and refraction of an electromagnetic wave packet. *Phys. Rev. Lett.*, 96(7):073903, 2006.

103. Lingang Zhang, Baifei Shen, Xiaomei Zhang, Shan Huang, Yin Shi, Chen Liu, Wenpeng Wang, Jiancai Xu, Zhikun Pei, and Zhizhan Xu. Deflection of a reflected intense vortex laser beam. *Phys. Rev. Lett.*, 117(11):113904, 2016.

104. V. S. Liberman and B. Ya. Zel'dovich. Spin-orbit interaction of a photon in an inhomogeneous medium. *Phys. Rev. A*, 46(8):5199, 1992.

105. K. Yu. Bliokh and Yu. P. Bliokh. Modified geometrical optics of a smoothly inhomogeneous isotropic medium: the anisotropy, Berry phase, and the optical magnus effect. *Phys. Rev. E*, 70(2):026605, 2004.

106. K. Yu. Bliokh and Yu. P. Bliokh. Topological spin transport of photons: the optical magnus effect and Berry phase. *Physics Letters A*, 333(3-4):181–186, 2004.

107. C. Duval, Z. Horvath, and P. A. Horvathy. Geometrical spinoptics and the optical Hall effect. *Journal of Geometry and Physics*, 57(3):925 – 941, 2007. ISSN 0393-0440. doi: https://doi.org/10.1016/j.geomphys.2006.07.003.

108. Noriaki Horiuchi. Classical optics: Spin Hall effect of light. *Nature Photonics*, 7(1):2–2, 2013.

109. I. V. Tokatly. Orbital momentum hall effect in p-doped graphane. *Phys. Rev. B*, 82:161404, Oct 2010. doi: 10.1103/PhysRevB.82.161404. URL https://link.aps.org/doi/10.1103/PhysRevB.82.161404.

110. Jin Zhang, Xin-Xing Zhou, Xiao-Hui Ling, Shi-Zhen Chen, Hai-Lu Luo, and Shuang-Chun Wen. Orbit-orbit interaction and photonic orbital hall effect in reflection of a light beam. 23 (6):064215, may 2014. doi: 10.1088/1674-1056/23/6/064215.

111. Yeon Ui Lee, Igor Ozerov, Frederic Bedu, Ji Su Kim, Frederic Fages, and Jeong Weon Wu. Spin-and orbital-hall effect in cyclic group symmetric metasurface. *arXiv preprint arXiv:1607.04806*, 2016.

112. Sayantika Bhowal and S. Satpathy. Intrinsic orbital moment and prediction of a large orbital hall effect in two-dimensional transition metal dichalcogenides. *Phys. Rev. B*, 101:121112, Mar 2020. doi: 10.1103/PhysRevB.101.121112. URL https://link.aps.org/doi/10.1103/PhysRevB.101.121112.

113. Sayantika Bhowal and Giovanni Vignale. Orbital hall effect as an alternative to valley hall effect in gapped graphene. *Phys. Rev. B*, 103:195309, May 2021. doi: 10.1103/PhysRevB.103.195309. URL https://link.aps.org/doi/10.1103/PhysRevB.103.195309.

114. Athira B. S., Sounak Mukherjee, Anuraj Laha, Koushik Bar, Dibyendu Nandy, and Nirmalya Ghosh. Experimental observation of the orbital hall effect of light through pure orbit–orbit interaction for randomly and radially polarized vortex beams. *J. Opt. Soc. Am. B*, 38(7): 2180–2186, Jul 2021. doi: 10.1364/JOSAB.426304.

115. Young-Gwan Choi, Daegeun Jo, Kyung-Hun Ko, Dongwook Go, Kyung-Han Kim, Hee Gyum Park, Changyoung Kim, Byoung-Chul Min, Gyung-Min Choi, and Hyun-Woo Lee. Observation of the orbital hall effect in a light metal ti. *arXiv preprint arXiv:2109.14847*, 2021.

116. V.G. Fedoseyev. Spin-independent transverse shift of the centre of gravity of a reflected and of a refracted light beam. *Optics Communications*, 193(1):9–18, 2001. ISSN 0030-4018.

117. Konstantin Y. Bliokh and Anton S. Desyatnikov. Spin and orbital Hall effects for diffracting optical beams in gradient-index media. *Phys. Rev. A*, 79:011807, Jan 2009. doi: 10.1103/PhysRevA.79.011807. URL https://link.aps.org/doi/10.1103/PhysRevA.79.011807.

118. E. Nordblad. Transverse and lateral shifts of the center of gravity of a refracted nonparaxial bessel beam. *Phys. Rev. A*, 85:013847, Jan 2012. doi: 10.1103/PhysRevA.85.013847. URL https://link.aps.org/doi/10.1103/PhysRevA.85.013847.

119. Zhaoju Yang, Fei Gao, Xihang Shi, Xiao Lin, Zhen Gao, Yidong Chong, and Baile Zhang. Topological acoustics. *Phys. Rev. Lett.*, 114(11):114301, 2015.

120. Meng Xiao, Wen-Jie Chen, Wen-Yu He, and Che Ting Chan. Synthetic gauge flux and Weyl points in acoustic systems. *Nature Physics*, 11(11):920–924, 2015.

121. Romain Fleury, Alexander B Khanikaev, and Andrea Alu. Floquet topological insulators for sound. *Nat. Commun.*, 7(1):1–11, 2016.

122. Cheng He, Xu Ni, Hao Ge, Xiao-Chen Sun, Yan-Bin Chen, Ming-Hui Lu, Xiao-Ping Liu, and Yan-Feng Chen. Acoustic topological insulator and robust one-way sound transport. *Nature physics*, 12(12):1124–1129, 2016.

123. Jun Mei, Zeguo Chen, and Ying Wu. Pseudo-time-reversal symmetry and topological edge states in two-dimensional acoustic crystals. *Scientific reports*, 6(1):1–7, 2016.

124. Yu-Gui Peng, Cheng-Zhi Qin, De-Gang Zhao, Ya-Xi Shen, Xiang-Yuan Xu, Ming Bao, Han Jia, and Xue-Feng Zhu. Experimental demonstration of anomalous floquet topological insulator for sound. *Nat. Commun.*, 7(1):1–8, 2016.

125. Zhiwang Zhang, Qi Wei, Ying Cheng, Ting Zhang, Dajian Wu, and Xiaojun Liu. Topological creation of acoustic pseudospin multipoles in a flow-free symmetry-broken metamaterial lattice. *Phys. Rev. Lett.*, 118(8):084303, 2017.

126. Yuanchen Deng, Hao Ge, Yuan Tian, Minghui Lu, and Yun Jing. Observation of zone folding induced acoustic topological insulators and the role of spin-mixing defects. *Phys. Rev. B*, 96 (18):184305, 2017.

127. Hailong He, Chunyin Qiu, Liping Ye, Xiangxi Cai, Xiying Fan, Manzhu Ke, Fan Zhang, and Zhengyou Liu. Topological negative refraction of surface acoustic waves in a Weyl phononic crystal. *Nature*, 560(7716):61–64, 2018.

128. Zhiwang Zhang, Ye Tian, Yihe Wang, Shuxiang Gao, Ying Cheng, Xiaojun Liu, and Johan Christensen. Directional acoustic antennas based on Valley-Hall topological insulators. *Advanced Materials*, 30(36):1803229, 2018.

129. Zhiwang Zhang, Ye Tian, Ying Cheng, Qi Wei, Xiaojun Liu, and Johan Christensen. Topological acoustic delay line. *Phys. Rev. Applied*, 9(3):034032, 2018.

130. Weiwei Zhu, Xinsheng Fang, Dongting Li, Yong Sun, Yong Li, Yun Jing, and Hong Chen. Simultaneous observation of a topological edge state and exceptional point in an open and non-hermitian acoustic system. *Phys. Rev. Lett.*, 121(12):124501, 2018.

131. Jiuyang Lu, Chunyin Qiu, Weiyin Deng, Xueqin Huang, Feng Li, Fan Zhang, Shuqi Chen, and Zhengyou Liu. Valley topological phases in bilayer sonic crystals. *Phys. Rev. Lett.*, 120 (11):116802, 2018.

132. Miguel A Bandres, Steffen Wittek, Gal Harari, Midya Parto, Jinhan Ren, Mordechai Segev, Demetrios N Christodoulides, and Mercedeh Khajavikhan. Topological insulator laser: Experiments. *Science*, 359(6381):eaar4005, 2018.

133. Guancong Ma, Meng Xiao, and Che Ting Chan. Topological phases in acoustic and mechanical systems. *Nature Reviews Physics*, 1(4):281–294, 2019.

134. Xiang Ni, Matthew Weiner, Andrea Alù, and Alexander B. Khanikaev. Observation of higher-order topological acoustic states protected by generalized chiral symmetry. *Nature Materials*, 18(2):113–120, 2019.

135. Haoran Xue, Yahui Yang, Fei Gao, Yidong Chong, and Baile Zhang. Acoustic higher-order topological insulator on a kagome lattice. *Nature Materials*, 18(2):108–112, 2019.

136. Yujiang Ding, Yugui Peng, Yifan Zhu, Xudong Fan, Jing Yang, Bin Liang, Xuefeng Zhu, Xiangang Wan, and Jianchun Cheng. Experimental demonstration of acoustic chern insulators. *Phys. Rev. Lett.*, 122(1):014302, 2019.

137. Yang Long, Jie Ren, and Hong Chen. Unsupervised manifold clustering of topological phononics. *arXiv preprint arXiv:2001.02661*, 2020.

138. Shubo Wang, Guancong Ma, and Che Ting Chan. Topological transport of sound mediated by spin-redirection geometric phase. *Science Advances*, 4(2):eaaq1475, 2018.

139. Zheguang Zou, Robert Lirette, and Likun Zhang. Orbital angular momentum reversal and asymmetry in acoustic vortex beam reflection. *Phys. Rev. Lett.*, 125:074301, Aug 2020. doi: 10.1103/PhysRevLett.125.074301. URL https://link.aps.org/doi/10.1103/PhysRevLett.125.074301.

140. X. M. Zhou, G. K. Hu, and T. J. Lu. Single gradientless light beam drags particles as tractor beams. *Phys. Rev. B*, 77:024101, Jan 2008. doi: 10.1103/PhysRevB.77.024101. URL https://link.aps.org/doi/10.1103/PhysRevB.77.024101.

141. J. P. Leão-Neto, J. H. Lopes, and G. T. Silva. Core-shell particles that are unresponsive to acoustic radiation force. *Phys. Rev. Applied*, 6: 024025, Aug 2016. doi: doi.org/10.1103/PhysRevApplied.6.024025. URL https://link.aps.org/doi.org/10.1103/PhysRevApplied.6.024025.

142. L. Zhang. A general theory of arbitrary bessel beam scattering and interactions with a sphere. *J. Acoust. Soc. Am.*, 143(5):2796–2800, 2018. doi: 10.1121/1.5036734. URL https://doi.org/10.1121/1.5036734.

143. R. A. Roy and R. E. Apfel. Mechanical characterization of microparticles by scattered ultrasound. *J. Acoust. Soc. Am.*, 87(6):2332, 1990. doi: doi/10.1121/1.399079. URL https://doi.org/doi/10.1121/1.399079.

144. J. Shi, X. Ahmed, D.and Mao, S.-C. S. Lin, A. Lawit, and T. J. Huang. Acoustic tweezers: patterning cells and microparticles using standing surface acoustic waves (ssaw). *Lab Chip*, 9:2890–2895, 2009. doi: 10.1039/B910595F. URL http://dx.doi.org/10.1039/B910595F.

145. Peter Glynne-Jones, Puja P. Mishra, Rosemary J. Boltryk, and Martyn Hill. Efficient finite element modeling of radiation forces on elastic particles of arbitrary size and geometry. *The Journal of the Acoustical Society of America*, 133(4):1885–1893, 2013. doi: 10.1121/1.4794393. URL https://doi.org/10.1121/1.4794393.

146. Alexey A. Gorlach, Maxim A. Gorlach, Andrei V. Lavrinenko, and Andrey Novitsky. Matter-wave tractor beams. *Phys. Rev. Lett.*, 118: 180401, May 2017. doi: 10.1103/PhysRevLett.118.180401. URL https://link.aps.org/doi/10.1103/PhysRevLett.118.180401.

147. P. L. Marston. Negative axial radiation forces on solid spheres and shells in a Bessel beam. *J. Acoust. Soc. Am*, 122:3162 – 3165, 2007. doi: https://doi.org/10.1121/1.2799501.

148. Philip L. Marston. Scattering and radiation force dependence on properties of empty elastic spherical shells: Low-frequency phase-shift derivation. *The Journal of the Acoustical Society of America*, 146(2):EL145–EL150, 2019. doi: 10.1121/1.5121576. URL https://doi.org/10.1121/1.5121576.

149. Philip L. Marston. Phase-shift derivation of expansions for material and frequency dependence of progressive-wave radiation forces and backscattering by spheres. *The Journal of the Acoustical Society of America*, 145(1):EL39–EL44, 2019. doi: 10.1121/1.5087646. URL https://doi.org/10.1121/1.5087646.

150. Junru Wu. Acoustic streaming and its applications. *Fluids*, 3(4), 2018. ISSN 2311-5521. doi: 10.3390/fluids3040108. URL https://www.mdpi.com/2311-5521/3/4/108.

151. J. T. Karlsen, P. Augustsson, and H. Bruus. Acoustic force density acting on inhomogeneous fluids in acoustic fields. *Phys. Rev. Lett.*, 117:4504, 2016. doi: 10.1103/PhysRevLett.117.114504.

152. Roberto Piazza. Thermophoresis: moving particles with thermal gradients. *Soft Matter*, 4: 1740–1744, 2008.

153. M. Škarabot, Ž. Lokar, and I. Muševič. Transport of particles by a thermally induced gradient of the order parameter in nematic liquid crystals. *Phys. Rev. E*, 87:062501, Jun 2013.

154. Jiajie Chen, Hengji Cong, Fong-Chuen Loo, Zhiwen Kang, Minghui Tang, Haixi Zhang, Shu-Yuen Wu, Siu-Kai Kong, and Ho-Pui Ho. Thermal gradient induced tweezers for the manipulation of particles and cells. *Scientific reports*, 6:35814, 2016.

155. Xu-Dong Fan, Zheguang Zou, and Likun Zhang. Acoustic vortices in inhomogeneous media. *Physical Review Research*, 1(3):032014, 2019.

156. J. Yi. *Physics from Topology and Structures*, pages 117–137. Springer Berlin Heidelberg, Berlin, Heidelberg, 2006.

157. Xiaobo Yin, Ziliang Ye, Junsuk Rho, Yuan Wang, and Xiang Zhang. Photonic spin Hall effect at metasurfaces. *Science*, 339(6126):1405–1407, 2013. ISSN 0036-8075. doi: 10.1126/science.1231758. URL https://science.sciencemag.org/content/339/6126/1405.

158. Y. Li, X. Jiang, B. Liang, J. Cheng, and L. Zhang. Metascreen-based acoustic passive phased array. *Phys. Rev. Appl.*, 4:024003, 2015. doi: 10.1103/PhysRevApplied.4.024003.

159. K. Y. Bliokh and A. Aiello. Goos–hänchen and imbert–fedorov beam shifts: an overview. 15(1):014001, jan 2013. doi: 10.1088/2040-8978/15/1/014001. URL https://doi.org/10.1088/2040-8978/15/1/014001.

160. V. G. Fedoseyev. Transformation of the orbital angular momentum at the reflection and transmission of a light beam on a plane interface. *Journal of Physics A*, 41(50):505202, 2008.

161. Yong Li, Shuibao Qi, and M. Badreddine Assouar. Theory of metascreen-based acoustic passive phased array. 18(4):043024, apr 2016. doi: 10.1088/1367-2630/18/4/043024. URL https://doi.org/10.1088/1367-2630/18/4/043024.

162. Xue Jiang, Yong Li, and Likun Zhang. Thermoviscous effects on sound transmission through a metasurface of hybrid resonances. *The Journal of the Acoustical Society of America*, 141(4):EL363–EL368, 2017. doi: 10.1121/1.4979682. URL https://doi.org/10.1121/1.4979682.

163. Nanfang Yu, Patrice Genevet, Mikhail A. Kats, Francesco Aieta, Jean-Philippe Tetienne, Federico Capasso, and Zeno Gaburro. Light propagation with phase discontinuities: Generalized laws of reflection and refraction. *Science*, 334(6054): 333–337, 2011. ISSN 0036-8075. doi: 10.1126/science.1210713. URL https://science.sciencemag.org/content/334/6054/333.

APPENDIX

SCATTERING FUNCTIONS

The scattering functions s_n,[42] which are determined by the boundary conditions and material properties, can be calculated by

$$s_n = -\frac{D_n^*}{D_n}, \tag{.1}$$

where D_n is a function of ka and material parameters. It has $|s_n| \leq 1$ and when losses are negligible, $|s_n| = 1$.

For a rigid sphere,[13]

$$D_n = h_n^{(1)\prime}(x), \tag{.2}$$

where $h_n^{(1)}(x)$ is the first kind of spherical Hankel function with $x = ka$, and $'$ represents the derivative with respect to the argument.

For a fluid sphere,[13]

$$D_n = \lambda x j_n(x/\sigma) h_n^{(1)\prime}(x) - x/\sigma j_n'(x/\sigma) h_n^{(1)}(x), \tag{.3}$$

where $j_n(x)$ is the spherical Bessel function, and $\lambda = \rho/\rho_0$ and $\sigma = c/c_0$ are the density ratio and the speed ratio of particle to background medium.

For a solid sphere,[36] D_n is the determinant of the 3-by-3 matrix having the following

elements:

$$
\begin{aligned}
d_{11} &= (z^2/\lambda)h_n^{(1)}(x) \\
d_{12} &= (2N - z^2)j_n(y) - 4y j_n^{'}(y) \\
d_{13} &= 2N[z j_n^{'}(z) - j_n(z)] \\
d_{21} &= -x h_n^{(1)\,'}(x) \\
d_{22} &= y j_n^{'}(y) \\
d_{23} &= N j_n(z) \\
d_{31} &= 0 \\
d_{32} &= 2[j_n(y) - y j_n^{'}(y)] \\
d_{33} &= 2z j_n^{'}(z) + [z^2 - 2N + 2] j_n(z)
\end{aligned}
\tag{.4}
$$

where $x = ka$, $y = (c/c_L)x$, $z = (c/c_T)x$, and $N = n(n+1)$.

For a solid shell with outer and inner radius of a and b,[36] D_n is the determinant of the

5-by-5 matrix with the elements as that for a solid sphere and the remaining elements given by:

$$
\begin{aligned}
d_{14} &= [2N - z^2]n_n(y) - 4yn_n^{'}(y) \\
d_{15} &= 2N[zn_n^{'}(z) - n_n(z)] \\
d_{24} &= yn_n^{'}(y) \\
d_{25} &= Nn_n(z) \\
d_{34} &= 2[n_n(y) - yn_n^{'}(y)] \\
d_{35} &= 2zn_n^{'}(z) + [z^2 - 2N + 2]n_n(z) \\
d_{41} &= 0 \\
d_{42} &= [2N - w^2]j_n(u) - 4uj_n^{'}(u) \\
d_{43} &= 2N[wj_n^{'}(w) - j_n(w)] \\
d_{44} &= [2N - w^2]n_n(u) - 4un_n^{'}(u) \\
d_{45} &= 2N[wn_n^{'}(w) - n_n(w)] \\
d_{51} &= 0 \\
d_{52} &= 2[j_n(u) - uj_n^{'}(u)] \\
d_{53} &= 2wj_n^{'}(w) + [w^2 - 2N + 2]j_n(w) \\
d_{54} &= 2[n_n(u) - un_n^{'}(u)] \\
d_{55} &= 2wn_n^{'}(w) + [w^2 - 2N + 2]n_n(w)
\end{aligned}
\tag{.5}
$$

where n_n is the spherical Neumann function, $u = (c/c_L)kb$ and $w = (c/c_T)kb$.

VITA

Xudong Fan

Education

2021 – Ph.D. in physics and acoustics at the University of Mississippi

2017 – M.Sc. in physics and acoustics at Nanjing University

2015 – B.Sc. in physics and acoustics at Nanjing University

Research

2017 - 2021 – Acoustic radiation force and ocean acoustics in National Center for Physical Acoustics, Dept. of Physics and Astronomy, the University of Mississippi

2015 - 2017 – Acoustic meta-materials in Institute of Acoustics, Department of Physics, Nanjing University

Academic Employment

2017 - 2019 – Teaching assistant, General Physics I and II labs, grading, and other duties, Dept. of Physics and Astronomy, University of Mississippi

2017 - 2021 – Research assistant, Acoustic radiation force, ocean acoustics, bubble dynamics in National Center for Physical Acoustics, Dept. of Physics and Astronomy, the University of Mississippi

Professional Activities

2018 – Physical Acoustics Summer School at the University of Mississippi. A week long lecture series on topics related to physical acoustics.